Final Technical Report

U.S. Department of Energy
Grant No. DE-FG02-06ER64210

Integrated Hydrogeophysical and Hydrogeologic Driven Parameter Upscaling for Dual-Domain Transport Modeling

Prepared by

John M. Shafer, P.I.
University of South Carolina
Columbia, SC 20208

November 2012

PROJECT OVERVIEW

Our basic hypothesis was that significant improvement in the prediction of contaminant migration can be achieved through finer scale understanding of hydrogeologic heterogeneity which dominates advective transport. Our working hypothesis was fine spatial scale (1 m resolution or less) characterization of hydraulic conductivity and porosity can be achieved through an integration of hydrogeophysical measurements and analyses with understanding of the subsurface depositional environment and the hydrogeologic facies configuration. Further, improvement in prediction of subsurface contaminant migration can be achieved by incorporating the finer scale hydrogeologic heterogeneity in a dual-domain transport concept.

A major component of this effort was the integration of hydrogeophysical-based borehole and surface data with hydrogeologic information (e.g., facies modeling) to extend the finer scale parameterization to field scale for flow and transport modeling purposes. A second component of the research is to incorporate the parameter upscaling in a dual-domain solute transport modeling process. Even with improved parameterization, small to intermediate scale heterogeneity is present and significantly influences contaminant migration. Although computing capabilities continue to advance, explicit representation of these smaller scale features through very high resolution simulation is not likely to support the vast majority of the U.S. Department of Energy's environmental clean-up efforts over the next decade. Therefore, the impact of sub-grid scale heterogeneity on plume dispersion must be cost-effectively addressed as part of an overall, multi-scale, treatment of subsurface variability. We used a dual-domain solute transport formulation to handle sub-grid scale heterogeneity identified through finer scale site characterization.

We tested our hypotheses through a series of hydrogeophysical experiments (i.e., seismic, radar, tomography) conducted at the P Reactor Area (Figure 1) at the Savannah River Site (SRS) in South Carolina. Several plumes have been identified here and the plume of interest was a trichloroethylene (TCE) plume that emanates from the northwest section of the reactor facility and discharges to nearby Steel Creek. Our goal was to develop a new approach for upscaling in heterogeneous environments, via hydrogeophysical characterization and interpretation coupled to geologic modeling, and prove the efficacy of this approach through dual-domain solute transport conceptualization.

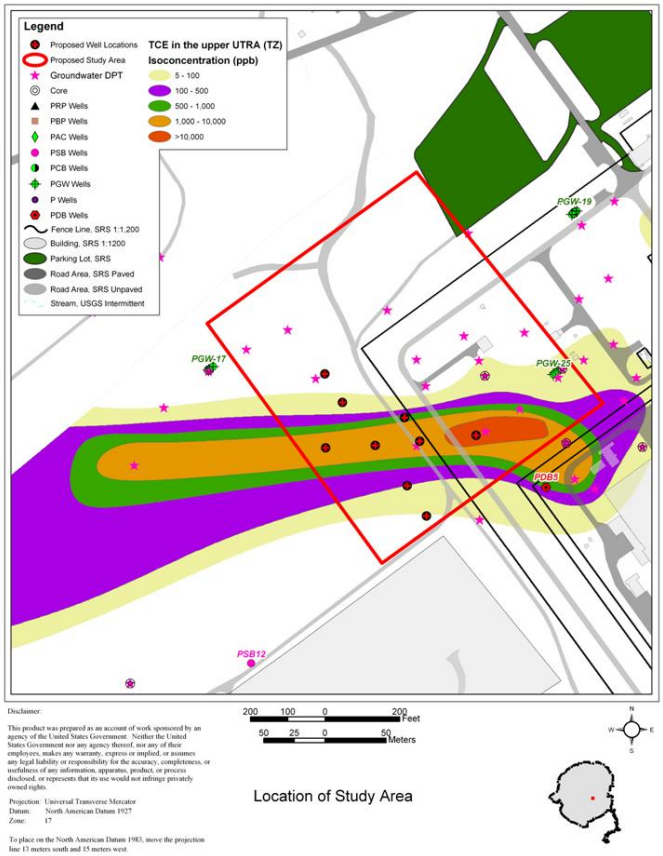

Figure 1. SRS P Reactor Area study site.

ORGANIZATION OF FINAL TECHNICAL REPORT

This final technical report is organized according to the three major study areas and the peer-reviewed publications that have been produced to describe the results of these focused investigations. The three major components of this research were:

1. Application of minimally invasive, cost effective hydrogeophysical techniques (surface and borehole), to generate fine scale (~1m or less) 3D estimates of subsurface heterogeneity. Heterogeneity is defined as spatial variability in hydraulic conductivity and/or hydrolithologic zones.

2. Integration of the fine scale characterization of hydrogeologic parameters with the hydrogeologic facies to upscale the finer scale assessment of heterogeneity to field scale.

3. Determination of the relationship between dual-domain parameters and practical characterization data.

The results of the above research are described in the following sections of this report through the peer-reviewed publications produced by this research effort.

SECTION 1

APPLICATION OF HYDROGEOPHYSICAL TECHNIQUES FOR SITE CHARACTERIZATION

Publication 1: Addison, A.D., M.G. Waddell, C.C. Knapp, D.T. Brantley, and J.M. Shafer, 2009, Developing a robust geologic conceptual model using 3-D P-wave seismic reflection data, **Environmental Geosciences**, 16(1), 41-56.

Publication 2: Cameron-Gonzalez, A.E., C.C. Knapp, M.G. Waddell, A.D. Addison, and J.M. Shafer, 2010, Structural and stratigraphic control on the migration of a contaminant plume at the P Reactor area, Savannah River site, South Carolina, **Environmental Geosciences**, 17(2), 77-98.

Developing a robust geologic conceptual model using pseudo 3-D P-wave seismic reflection data

Adrian D. Addison, Michael G. Waddell, Camelia C. Knapp, Duke T. Brantley, and John M. Shafer

ABSTRACT

As part of a multiscale hydrogeophysical and modeling study, a pseudo three-dimensional (3-D) seismic survey was conducted over a contaminant plume at P area, Savannah River site (South Carolina), to enhance the existing geologic model by resolving uncertainties in the lithostratigraphic sequence. The geometry of the dissolved phase trichloroethylene plume, based on initial site characterization, appears to be confined to a narrow corridor within the Eocene sand overlying a clay unit approximately 25 m (82 ft) below land surface. Processing the seismic data as a 3-D data volume instead of a series of closely spaced two-dimensional lines allowed for better interpretation of the target horizons, the lower clay, and the sand above the clay. Calibrating the seismic data with existing borehole geophysical logs, core data as well as vertical seismic profiling (VSP) data allowed the seismic data to be inverted from two-way traveltime to depth, thereby facilitating full integration of the seismic data into a solid earth model that is the basic part of a site conceptual model. The outcome was the production of realistic horizon surface maps that show that two channel complexes are located on the section, which are not present in the conceptual model, and that the upper and middle clays are not laterally continuous as previously thought. The geometry of the primary channel has been transposed over the map view of the plume to investigate potential relationships between the shape of the plume and the presence of the channel.

INTRODUCTION

The P area at the Savannah River site (SRS) is located in the upper Atlantic coastal plain of South Carolina (Figure 1), which consists of approximately 350 m (1148 ft) of unconsolidated sands, clays, and

DOI:10.1306/eg.10210808005

AUTHORS

ADRIAN D. ADDISON ~ *Department of Geological Sciences, University of South Carolina, Columbia, South Carolina; aaddison@geol.sc.edu*

Adrian Addison is a Ph.D. candidate in the Department of Geological Sciences at the University of South Carolina. He received his B.S. degree in geophysics from the University of Oklahoma and worked for 4 years as a geophysicist with the U.S. Geological Survey. His research interests are borehole and near-surface geophysics, environmental geology, and signal processing.

MICHAEL G. WADDELL ~ *Earth Sciences and Resources Institute, University of South Carolina, ESRI-USC Columbia, South Carolina*

Michael Waddell completed his graduate studies at ESRI-USC in 1982 and remained at ESRI-USC until 1984 when he became a reservoir geologist in Houston working on petrographic investigations of hydrocarbon reservoirs worldwide. In 1986, he returned to ESRI-USC to start an environmental geophysics group and is presently its manager.

CAMELIA C. KNAPP ~ *Department of Geological Sciences, University of South Carolina, Columbia, South Carolina*

Camelia Knapp received her Ph.D. in geophysics from Cornell University and her B.S. and M.S. degrees in geophysical engineering from the University of Bucharest (Romania). She worked with the Romanian State Oil Company and the National Institute for Earth Physics. Currently at the University of South Carolina, her research interests include exploration and environmental geophysics, crustal-scale seismology, and gas hydrates.

DUKE T. BRANTLEY ~ *Earth Sciences and Resources Institute, University of South Carolina, Columbia, South Carolina*

Duke Brantley is an M.S. degree candidate in the Department of Geological Sciences at the University of South Carolina. He received his M.S. degree in earth and environmental resources management from the University of South Carolina in 2006. He provides field and analytical support for geophysical and dewatering

studies for the Earth Sciences and Resources Institute at the University of South Carolina.

JOHN M. SHAFER ~ *Earth Sciences and Resources Institute, University of South Carolina, Columbia, South Carolina*

John Shafer earned his Ph.D. in civil engineering from Colorado State University, his M.S. degree in resource development from Michigan State University, and his B.S. degree in earth science from Penn State University. His research focus includes integrated site characterization, coupled simulation-optimization approaches to solving groundwater problems, and groundwater susceptibility and contamination potential analysis.

ACKNOWLEDGEMENTS

We would like to thank Maggie Millings (Savannah River National Laboratory) for her contributions in the completion of this work. We would like to thank Mary Harris and Gregory Flach (Savannah River National Laboratory), Susan Hubbard (Lawrence Berkeley National Laboratory), and Antonio Cameron (Geophysical Exploration Laboratory, University of South Carolina) for their contributions on the project. We would also like to thank Landmark Graphic Corporation and Seismic Micro-Technology, Inc. (ProMAX® and Kingdom® Suite software packages) for the University Grants Programs. This work was made possible through a grant by the U. S. Department of Energy (grant DE0FG02-06ER64210).

gravels ranging in age from Cretaceous to Pleistocene (Fallaw and Price, 1995) (Figure 2). Precharacterization efforts revealed that the groundwater is primarily contaminated with volatile organic compounds and tritium. Several plumes have been identified, and the plume of interest is a trichloroethylene (TCE) plume that emanates from the northwest section of the reactor facility and discharges to nearby Steel Creek (Figure 3). According to Millings et al. (2003), organic solvents, such as TCE, used in P-reactor operations were disposed of onsite. The shallow geological environment of the P area has been modestly characterized via a limited number of cone penetrometer (CPT) pushes and the installation of several clusters of observation wells.

This study is confined to the upper 45 m (148 ft) of Miocene and upper Eocene age coastal plain sediments. Figure 2 shows a simplified stratigraphic column of the units of interest starting from the surface with the upper sand unit followed by the upper clay, middle sand, middle clay, lower sand, and lower clay units. At P area, the TCE plume is located in an Eocene age sand that lies between the upper clay and middle clay units of the upper Atlantic coastal plain sediments (Figure 2). The geometry of the plume, based on initial site characterization from well, core, and CPT data, appears to be confined to a narrow corridor of sand overlying the middle clay unit approximately 25 m (82 ft) below land surface (Figure 3).

In 2006, three additional wells were installed at the site as part of a multiscale hydrogeophysical and modeling study where the TCE was identified below the middle clay. As part of an ongoing study at the P area, a pseudo three-dimensional (3-D) P-wave seismic survey was performed at the site. The seismic survey area was 34 by 170 m (111 by 558 ft), and 2906 shot points were recorded. Processing the data set as a 3-D data volume instead of a series of closely spaced 2-D lines allowed for better interpretation of the target horizons, which are the lower clay and the sand directly above it.

Traditional two-dimensional (2-D) common depth point (CDP) seismic surveys consist of acquiring a single shot and receiver line that is a single slice of the subsurface. The CDP method involves designing the seismic survey such that multiple ray paths are recorded from the same subsurface reflection point. This redundancy allows for determination of the subsurface velocity structure and the cancellation of certain types of extraneous seismic waves and random noise (Yilmaz, 1987). The pseudo 3-D reflection survey was designed to image the top of the first aquitard. The depth of this unit at P-area ranges from 21 to 37 m (69 to 121 ft) below land surface. Instead of conducting a true 3-D seismic survey, we conducted a CDP swath survey. A true 3-D seismic or patch shooting uses multiple sets of perpendicular source and geophone lines that are arranged in a rectangular pattern (Sheriff and Geldart, 1995). Similar to 2-D CDP acquisition, the swath technique differs from the patch in that several parallel geophone lines are used with (in our case) one source unit in a roll-along fashion (Sheriff and Geldart, 1995). The advantage of the swath for this project is that it achieved the fold multiplicity (the number of times a reflecting point is sampled over

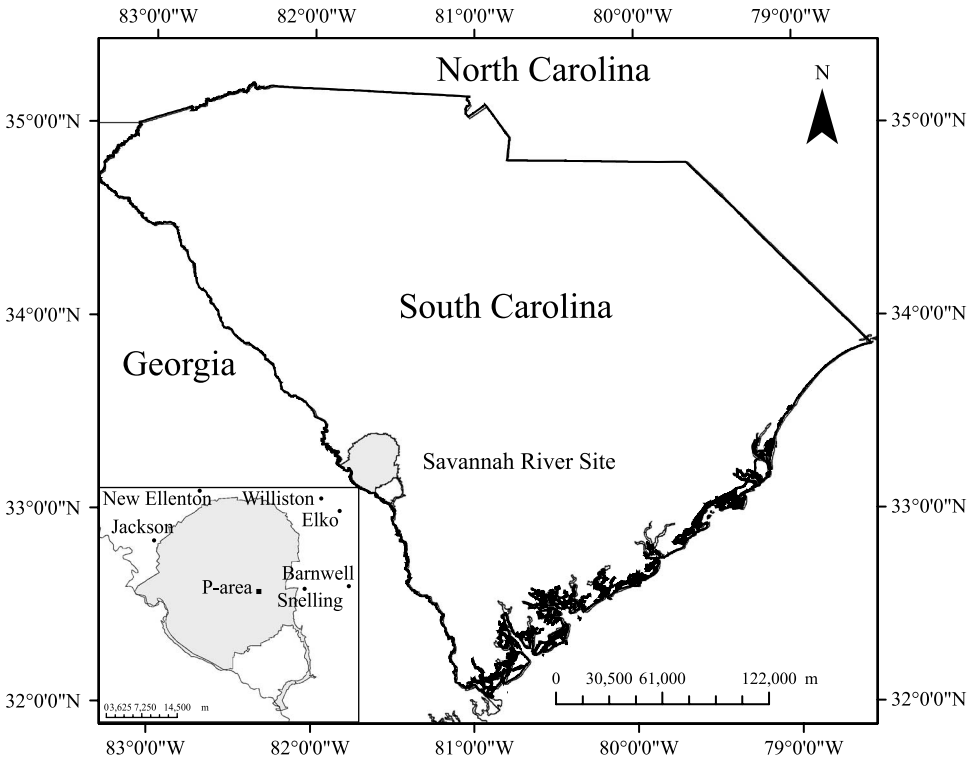

Figure 1. Location of the P area at the Savannah River site, South Carolina.

a spread length) (Sheriff and Geldart, 1995) as the patch technique but in a shorter time and ultimately at lower costs.

In site characterization, a conceptual model is the hydrologists' or geologists' idea of the subsurface (Reilly and Harbaugh, 2004) and is the foundation for building the rest of the models such as the geologic and hydrogeological transport for a particular project. A conceptual model is commonly a simple idea; in the case of the P area, the conceptual model is a 2-D geologic cross

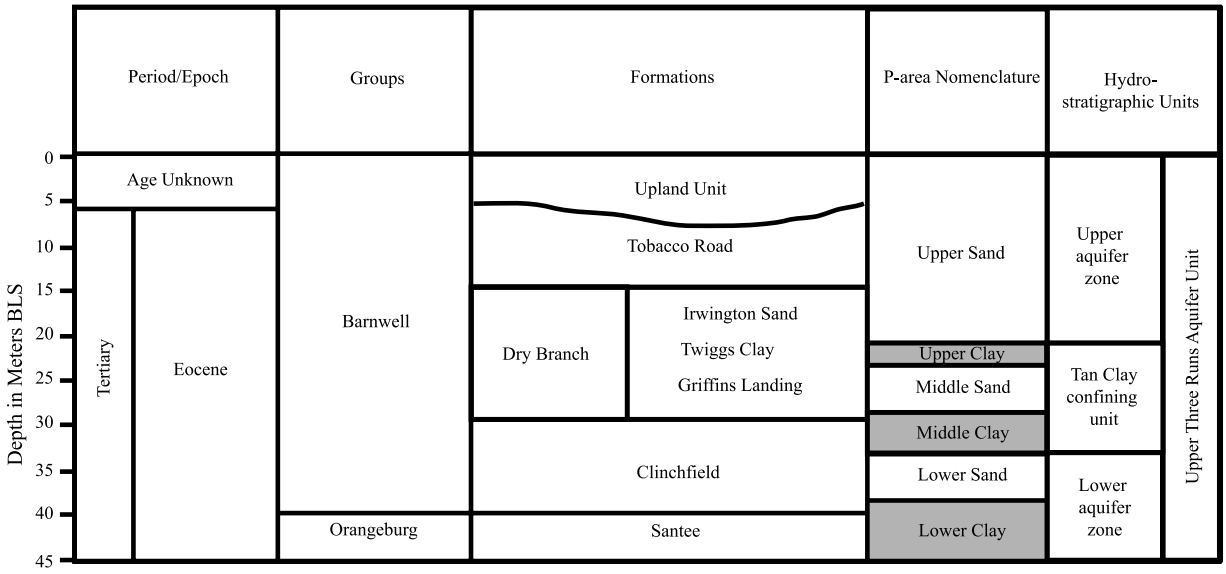

Figure 2. Simplified stratigraphic column for the P area, modified from Fallaw and Price (1995) with hydrostratigraphic units from Aadland et al., 1995.

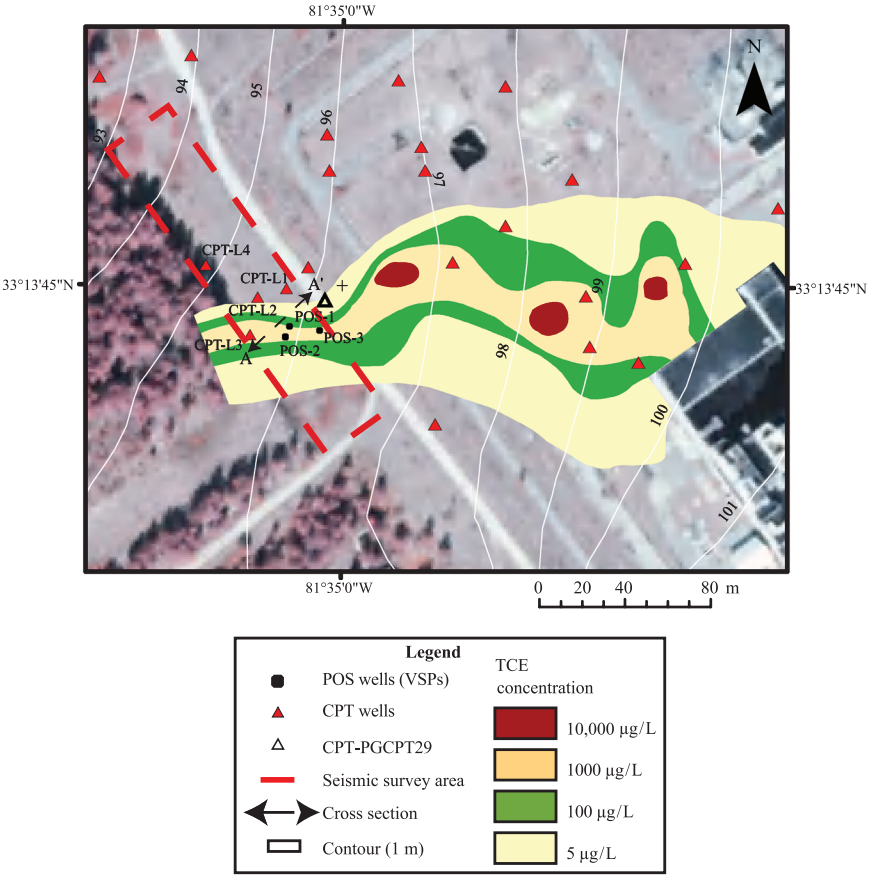

Figure 3. Geometry of trichloroethylene (TCE) plume at the P area, Savannah River site, South Carolina. The vertical seismic profiles (VSPs) were collected in the three position (POS) wells. The red dashed line is an outline of the seismic survey area. Plume flows from east to west discharging into Steel Creek, which is just west of the study area. Plume concentrations were determined from the cone penetrometer (CPT) well data (red triangles) with little well coverage west of the survey.

section with layers of lithologic units (alternating sands and clays) with the location of the TCE plume between the upper and middle clay layers (Figure 4). The cross section in Figure 4 was created from CPT data such as sleeve friction, tip friction, and pore pressure while determining the hydrofacies using grain size analysis from core data. The general dip of the stratigraphy is to the southeast along with the regional groundwater flow, but the plume has a flow direction of east to west. The plume geometry brings forth three questions: (1) What geologically is controlling the flow direction and the shape of the plume? (2) Can the seismic data answer the previous question? (3) Is there any correlation between the plume and the gravel deposits found above and below the upper clay unit in the cores of the position (POS) wells? These questions could not be answered without information beyond the conceptual model based on the cross section in Figure 4 and will be answered by the additional information provided by the seismic data. For transport modeling, a less than realistic model will result in poor modeling results leading to poor prediction of the plume migration and ultimately an ineffective site remediation plan.

HYDROGEOLOGIC SETTING

The P area at SRS is located in the upper Atlantic coastal plain, which consists of stratigraphy of Upper Cretaceous and Tertiary age sediments. Previous work on the geologic characterization at SRS includes a thorough study by Fallaw and Price (1995). Based on the scope of this project, the Tertiary sediments, which include the middle Eocene age Orangeburg and upper Eocene age Barnwell groups (Fallaw and Price, 1995), will be the focus of this article. The Congaree, Warley Hill, and Santee formations make up the Orangeburg Group, whereas the Barnwell Group consists of the Clinchfield, Dry Branch, and Tobacco Road Sand formations (Jean et al., 2002).

The Clinchfield Formation, a medium-grained, well-sorted, poorly consolidated, large bedded quartz sand is the lowermost formation in the Barnwell Group (Jean et al., 2002). The middle unit of the Barnwell Group, the Dry Branch Formation, is divided into three lithofacies: the Twiggs Clay (marine clay), the Irwinton Sand (sand and clay), and the Griffins Landing Member (calcareous and fossilierous sand) (Jean et al., 2002).

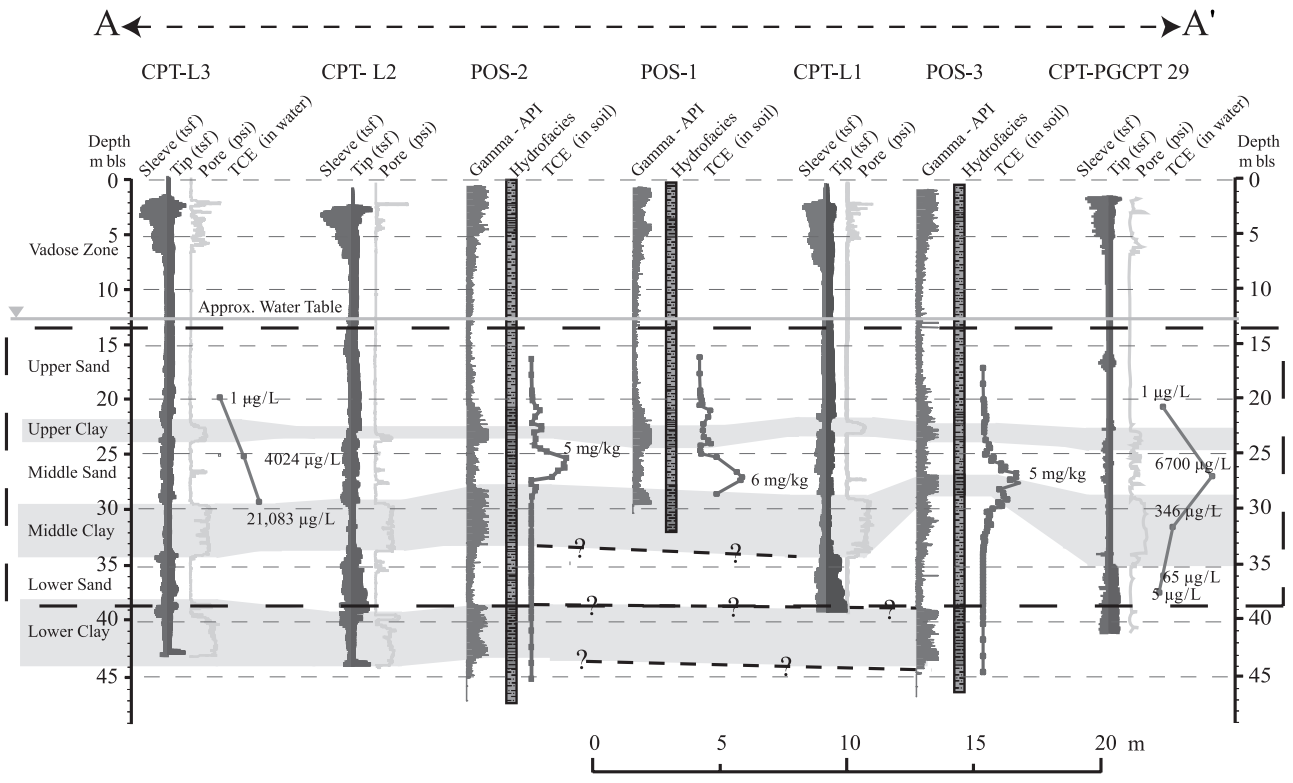

Figure 4. Stratigraphic cross section showing the three clay units and associated sand units at the P-area site. Cores from the position (POS) wells contain gravels above and below the upper clay unit. The dashed rectangle indicates the area of interest. The cross section was provided by the Savannah River National Laboratory. The cross section in the figure was created from cone penetrometer (CPT) data such as sleeve friction, tip friction, and pore pressure while determining the hydrofacies using grain size analysis from core data. TCE = trichloroethylene; BLS = below the surface.

According to Jean et al. (2002), the Tobacco Road Sand lies atop the Barnwell Group and consists of fine-grained and well-sorted to poorly sorted sediments with clay lenses (Jean et al., 2002). Throughout SRS, the ''Upland'' unit sits atop the Tobacco Road Sand, commonly at higher elevations. The Upland unit is generally thought to have been deposited in a fluvial environment consisting of poorly sorted, silty, clayey, and pebbly sand (Fallaw and Price, 1995).

The hydrogeologic setting at P area involves the upper part of the Floridan aquifer system that includes the Upper Three Runs aquifer (UTRA) (Aadland et al., 1995). The UTRA includes the Upland unit, Tobacco Road Sand, Dry Branch Formation, Clinchfield Formation, and Santee Limestone. At P area, the UTRA is informally divided in lower and upper aquifer zones (UAZs) separated by the Tan Clay confining zone (TCCZ). For the purpose of this article, the UTRA has been divided into three zones; the UAZ, the TCCZ, and the lower aquifer zone (LAZ) (Aadland et al., 1995). The LAZ is divided into the lower clay and lower sand facies beneath the TCCZ (Wyatt, 2000). The TCCZ was divided in the upper clay, middle sand, and middle clay facies. The UAZ is characterized by massive beds of sand and clayey sand with minor interbeds of clay (Wyatt, 2000).

DATA ACQUISITION

Before the pseudo 3-D seismic reflection survey was conducted, the minimum and maximum receiver line and source line offsets were determined after a vertical seismic profiling (VSP) analysis of the zero-offset VSP surveys. Zero-offset P-wave vertical seismic profiles were acquired in two wells previously constructed at the site for preliminary hydrogeologic and contaminant distribution characterization. These wells extend through the first aquitard to approximately 30–45 m (98–148 ft) below land surface. Data from the VSP surveys were used to evaluate the vertical acoustic velocity profile at the study site for optimal design of the 3-D surface seismic survey. The zero-offset VSP analysis was performed to determine the source and receiver

Table 1. Acquisition Parameters for the 3-D Seismic Data Collection at P Area, Savannah River Site, South Carolina

Parameter	Values
Group spacing	1 m
Line spacing	2 m
Sample rate	0.5 ms
Record length	500 ms
Accelerated weight drop	4–6 stacks per shot
Total shots	2906

line minimum and maximum offset as well as the source and receiver spacing and sample rate. This provided detailed information on lateral and vertical stratigraphic heterogeneity, subsurface velocities, and noise and signal attenuation. These data were necessary to design the acquisition parameters for the 3-D surface seismic survey. The VSP average velocities ranged from 800 to 1500 m/s (2625 to 4921 ft/s) for the area of interest.

The pseudo 3-D surface P-wave seismic reflection survey was designed using the GEDCO OMNI® 3-D seismic design software. The survey was designed to image the top of lower clay unit. The depth of the lower clay unit at the P-reactor area site ranges from 21 to 37 m (69 to 121 ft) below land surface within our survey area of 34 by 170 m (558 ft). The pseudo 3-D CDP swath survey was acquired with the source line parallel to the receiver line. In this acquisition design, the shots were fired on one line, and the reflected seismic energy was recorded on the parallel receiver line creating a CDP swath midway between the source and receiver line (Stone, 1994; Cordsen et al., 1995; Rex et al., 2003).

From previous experience in acquiring and processing shallow seismic data at SRS in conjunction with the VSP data, the acquisition parameters were as follows: receiver and shot spacing of 1 m (3 ft), sample rate of 0.5 ms, and record length of 500 ms (Table 1). In Figure 5, the red circles represent the receiver lines that are 2 m (6 ft) apart, and the black circles represent the shot lines that are 2 m (6 ft) apart. An example of a receiver line is highlighted in light blue to indicate live receivers, with the star being the shot location. The ability to shoot the survey prior to field deployment allowed us to determine if we had enough fold (the higher the fold, the better the signal to noise ratio) at the target depth. An anticipated fold of 30 for the target depth of 35 m (115 ft) below land surface (Figure 5B) was calculated and collected based on the acquisition design described above. The field acquisition was performed with a Geometrics 120 channel StrataView® seismograph with 40 Hz geophones and consisted of pairs of one active source line and one receiver line. An accelerated weight drop (Digipulse Model 100AE) with 4 to 6 stacks per shot was used as the seismic source for a total of 2906 shots.

DATA PROCESSING

Data processing was focused on the enhancement of reflected energy within the vadose zone and below the water table. Also, efforts were made to preserve the seismic amplitude for attributes analysis. At SRS, because of the shallow, unconsolidated sediments, the generation of surface waves during seismic acquisition represents a major challenge. To attenuate the surface waves, various 2-D filtering techniques were applied, including frequency-wave-number (f-k) and bandpass filtering.

Processing the data set as a 3-D volume instead of a series of closely spaced 2-D lines allowed better interpretation of the target horizons, which are the lower clay and the sand directly above the clay. Processing as a volume allows the seismic data to be interpolated from crossline to crossline and from inline to inline. Then the data can be interpreted on each inline and crossline within the 3-D volume. Table 2 lists the processing steps completed using Landmark Graphics' ProMax® in generating the 3-D volume. The first and most critical step was creating the geometry from the field notes and acquisition design from the GEDCO OMNI® 3-D software so that the data could be binned into a bin grid of 2 by 2 m (6 by 6 ft) totaling 1462 bins. The binning process merged the 17 individual 2-D lines into a volume with 17 inlines and 86 crosslines with 1462 CDPs (one CDP in each bin). After the field geometry was completed and loaded to the data set headers, the subsequent processing steps were used to generate the 3-D volume and enhance the reflectivity.

To increase the overall quality of the image, the data processing started with seismic trace editing to eliminate the noisy traces and to reverse the polarity of some traces. After trace editing, elevation statics were applied to account for topographic changes in the survey area. Elevations were collected for each receiver station of the survey using a TOPCON Total Station method. To account for amplitude loss caused by spherical spreading and attenuation, a spherical divergence correction was applied using a $1/(\text{time} \times [\text{velocity}]^2)$ function with a 0.0002 inelastic attenuation correction, a velocity function of 330 m/s (1083 ft/s) at 100 ms and 1500 m/s (4921 ft/s) below 100 ms, with a time-power constant

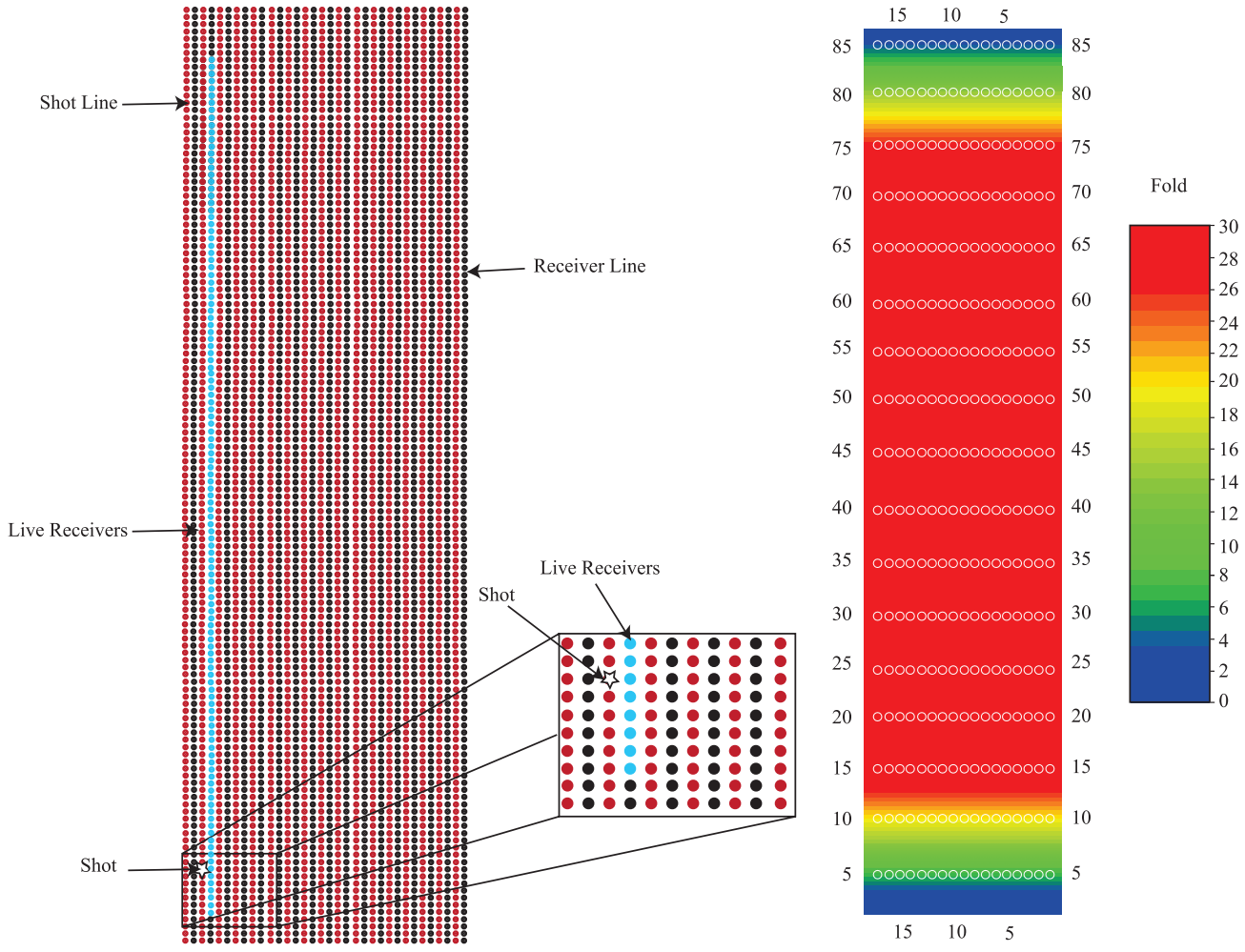

Figure 5. (A) Map showing the receiver and shot lines. (B) Map showing fold coverage, using the receiver and shot line configuration from panel A.

of 1.4. The next processing step involved predictive or spiking deconvolution using minimum phase spiking with an operator length of 20 ms and an operator white noise level of 0.1.

To remove as much unwanted noise as possible, a zero-phase Ormsby bandpass filter was applied with a 60-Hz notch for the overhead power lines and corner frequencies of 50-70-250-500 Hz. After the bandpass filter, an amplitude gain correction (automatic gain control) was applied using an operator window length of 20 ms. A progression of the processing steps can be seen in Figure 6, which shows a resulting shot gather with significantly improved signal-to-noise ratio.

An f-k filter was used to remove coherent linear noise (Yilmaz, 1987), in the case of this data set, ground roll or surface waves. Figure 6 shows a shot gather before and after the application of the f-k filter. A significant improvement in the ground roll suppression can be noticed as the underlying reflections are substantially enhanced (Figure 6). After the rejecting polygon was designed in the f-k domain, it was applied to the shot gathers before the velocity analysis.

After achieving an acceptable level of noise reduction in the prestack data, a velocity analysis was performed to obtain optimal stacking velocities. Because the stratigraphy and structure of the upper 40 m (131 ft) in the study area are fairly simple, a conventional normal move-out (NMO) stacking velocity analysis was used to obtain reliable root-mean-square velocities. As a guide for the velocity analysis, we used the VSP velocities. After velocity analysis (Figure 7), the resulting stacking velocities were smoothed and used to stack the data.

Subsequent processing was performed on the poststack data to further increase the signal-to-noise ratio and enhance the reflections. The residual statics was one such application that made a significant improvement in

Table 2. Processing Steps Used in Generating the Final Stack

Description	Parameters
Geometry	Defined using field notes, OMNI software, and loaded to headers
Trace edits	Eliminated bad or noisy traces and reversed trace with reverse polarity
Elevation statics	Applied from elevations of stations
Spherical divergence	Applied 1/(time $\times$ [velocity]^2) function with a 0.0002 inelastic attenuation correction, a velocity function of 300 m/s for 100 ms and 1500 m/s (4921 ft/s) between 100 ms, with a time-power constant of 1.4
Deconvolution	Spiking or predictive deconvolution using minimum-phase spiking with an operator length of 20 ms and an operator white noise level at 0.1 with a picked decon gate
Bandpass filter	Zero-phase Ormsby filter with a 60-Hz notch and corner frequencies of 50-70-250-500 Hz
Automatic gain control	20-ms operator length
f-k filter	An arbitrary polygon used to reject noise
Residual statics	Applied residual statics
Velocity analysis	Analysis from shot gathers, constant velocity stacks with semblance plots
Stack	NMO-corrected CMP gathers added
f-xy deconvolution	Number of inlines and crosslines in filter was 3, the rate of adaptation was 0.5 with starting and ending frequencies at 70 and 300 Hz, respectively
Time and depth conversion	Used VSP velocities to generate velocity profile

picking velocities in the next iteration of velocity analysis. Once satisfied with the stacking velocities, we tested several coherency filters to improve the appearance of the targeted interfaces.

An f-xy deconvolution filter was used to enhance the coherency along reflections (Figure 8). This filter was used with a rate of adaptation 0.5 with starting and ending frequencies at 70 and 300 Hz, respectively. Prior to the application of the f-xy deconvolution filter, the reflections seen in the stacked data were not as pronounced and coherent horizontally as they were afterwards. After the f-xy deconvolution filter, the seismic volume was migrated with a velocity function derived from the VSP velocities. This same velocity function was used to convert the 3-D volume to depth.

RESULTS

After data acquisition and processing, the final result is a 3-D volume consisting of 86 crosslines and 17 inlines that enhance the geologic model for the site. The seismic data are shown in Figure 9 as a 34 by 170 by 150 m (558 by 492 ft) in depth volume with good reflectivity throughout. Because of the relatively lower fold coverage, the reflection coherency is lost at the edges of the volume as compared to that of the center zone. In Figure 9, two highly reflective areas between 20–60 and 120–150 m (66–197 and 394–492 ft) are observed. Between 20 and 60 m (66 and 197 ft) is the area of interest consisting of the upper clay, middle sand, middle clay, lower sand, and lower clay units. These two areas show reflections that are for the most part subhorizontal. However, the reflections below the POS wells dip slightly. The dip becomes more extreme deeper in the volume, for example, note the reflections at 100 and 140 m (328 and 459 ft). The seismic volume was integrated with the geophysical well data in Kingdom® Suite and produced interpretable results with reference to our original hypothesis of adding supporting data to the conceptual model.

Based on the initial interpretations of cross section AA′ (Figure 4) based on well and CPT information, the upper and middle clay layers appear to be continuous laterally across the study area. However, through a closer look, the thickness of the upper clay is thin compared to those of the other two clay layers, and the middle clay in the vicinity of POS-3 appears to be truncated, to almost disappear. The depth extension of the gamma data for POS-1 also has a limitation because of the shallower construction depth of this well, therefore the thickness of the middle clay is interpolated from the surrounding well data. Because of the presence of gravel deposits

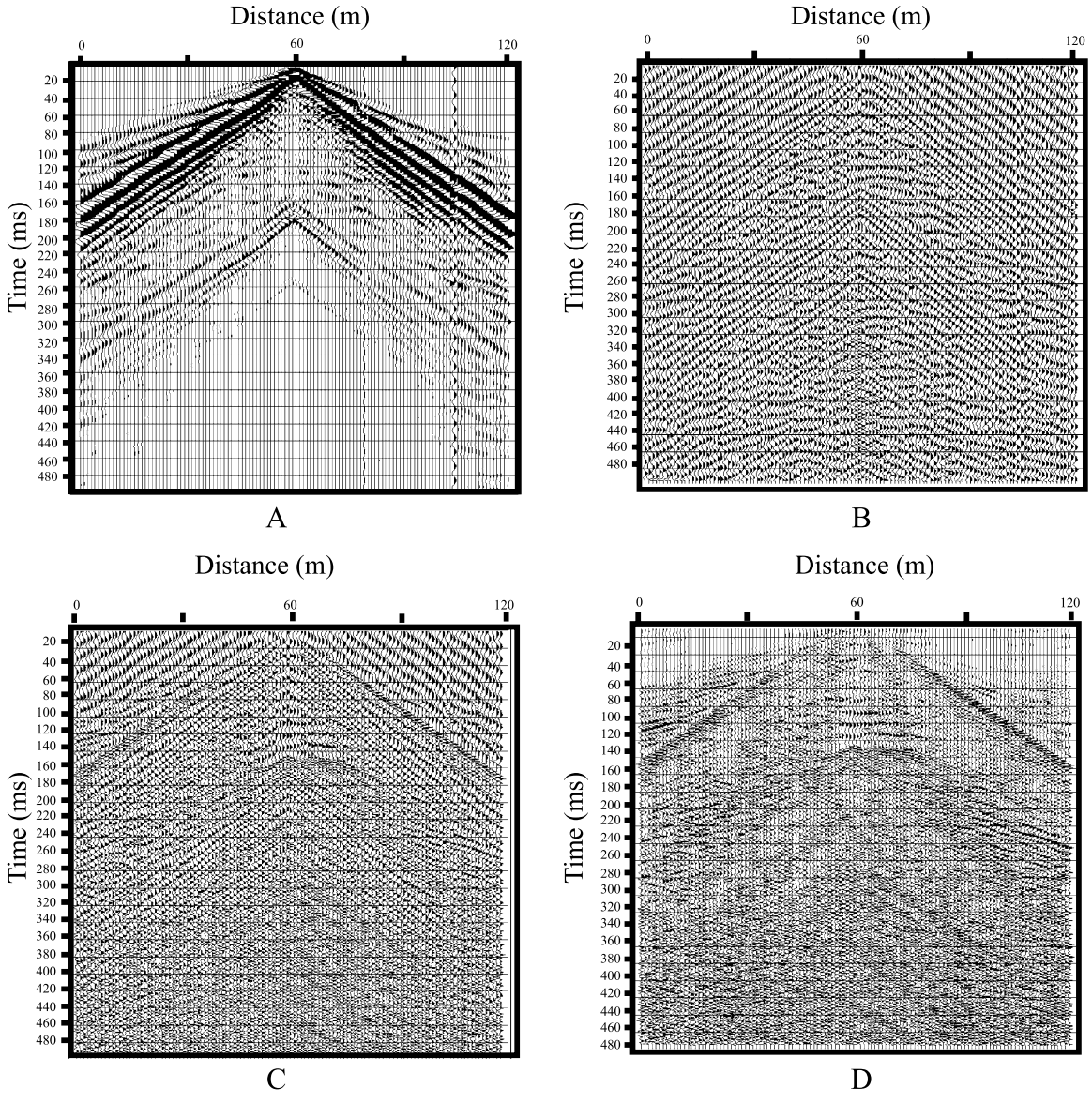

Figure 6. (A) A sample shot gather (FFID 1790) showing raw data. (B) The same shot gather, but with spherical spreading correction, bandpass filter, and automatic gain control (AGC) applied. (C) The same as in panel B but with spiking deconvolution applied. (D) The same as in panel C but with the addition of the f-k filter. automatic gain control (AGC).

below and above the upper clay unit, along with the variable thicknesses of the upper and middle clay layers, one can interpret that the gamma logs are sensitive to the clay lenses that are present from a fluvial depositional environment as mentioned by Fallaw and Price (1995).

Figure 10 shows an image of crossline 27 from the 3-D survey oriented in the same direction as the geologic cross section AA′ in Figure 4. Crossline 27 shows a clipped part of the volume to a depth of 100 m (328 ft) with the position of the three POS wells, the gamma logs for POS-1 and -3, and the clay horizons interpreted across the section. Crossline 27 shows the yellow horizon as the top of the lower clay and the green horizon as the top of the middle clay, which are the two units that contain the middle sand where the TCE plume is located. The blue horizon located on well POS-2 is where the top of the upper clay should be if it were present. Continuous throughout the section, the most well-defined reflection is the top of the lower clay unit, which is interpreted based on the thickness of this unit. The reflections attributed to the middle and lower clays at the POS wells correspond well with the gamma logs. The seismic crossline interpretation is essentially the same as the geologic cross section in Figure 4, with the

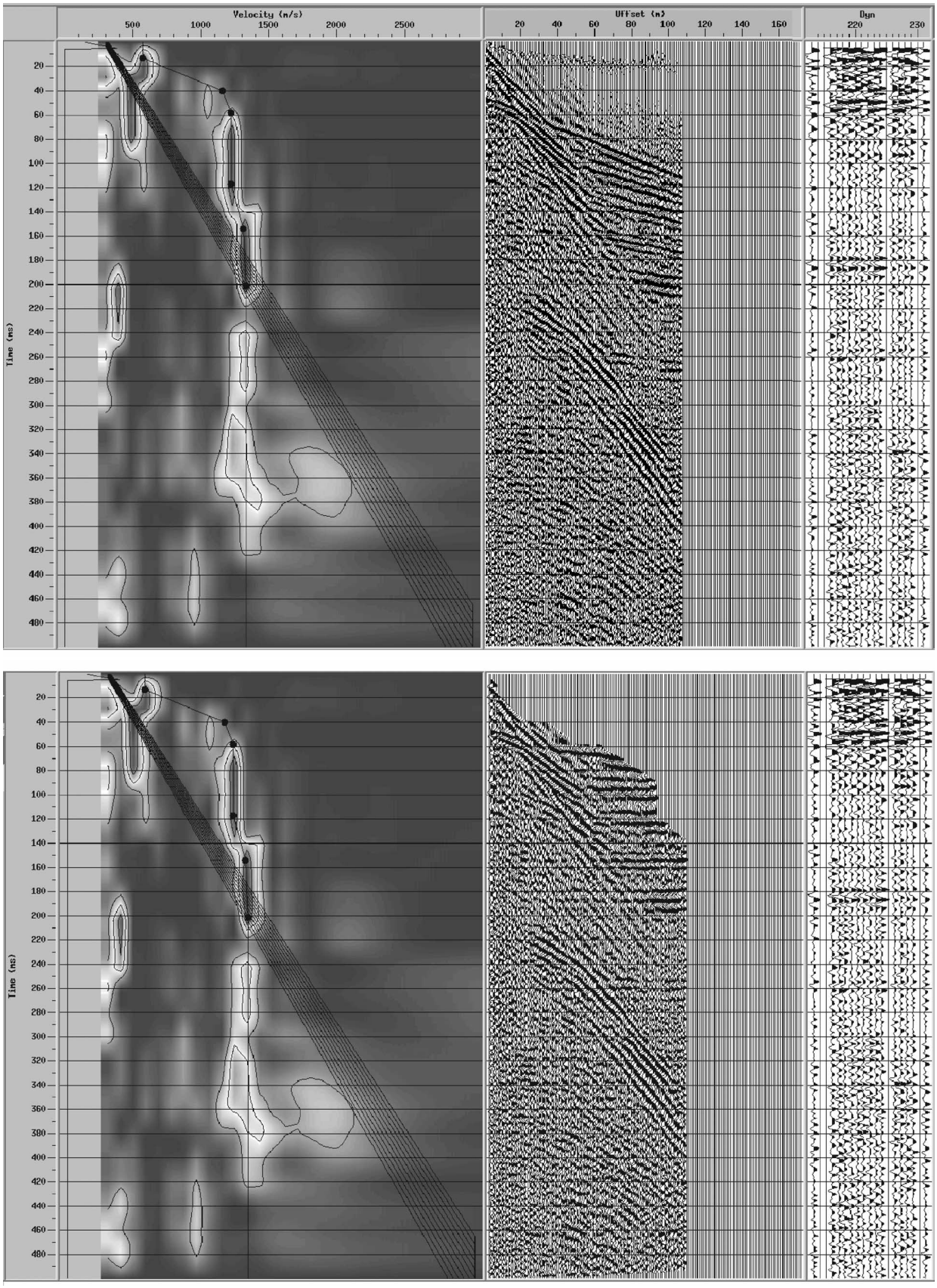

Figure 7. Velocity spectra and picks for the CDP supergather 222 (top) before and (bottom) after the NMO correction and 30% stretch mute application.

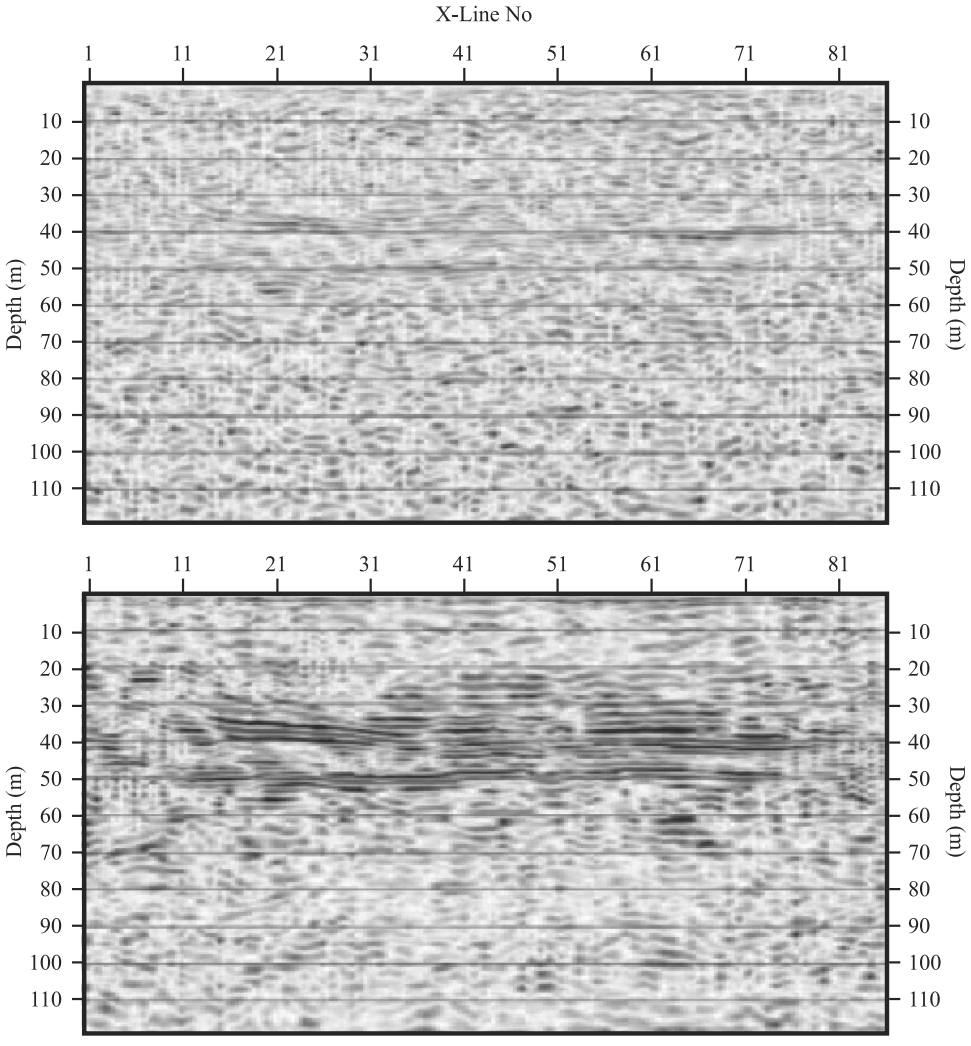

Figure 8. Stacked/inline 10 (top) without the f-xy deconvolution filter and (bottom) with the f-xy deconvolution filter. The reflections between 20 and 60 m (66 and 197 ft) show increased amplitudes and lateral coherency with the applied filter (bottom).

exception of the upper clay being absent on the seismic data.

Because the seismic data were processed as a volume, it allows the interpreter to analyze it in any arbitrary direction. Figure 11 is inline 10, which is perpendicular to crossline 27 shown in Figure 10. Starting from the southeastern end of the section near a depth of 10 m (33 ft) is a feature that is interpreted as a buried channel, which appears to incise down to 30 m (98 ft) through the upper and middle clay units and possibly the lower clay unit. In addition, another channel is interpreted starting from roughly northwest of crossline 50 that also appears to incise the upper and middle clay units. Because the TCE and POS wells are located in the southeastern channel (red), this will be denoted as the primary channel and the channel interpreted toward the northwest (blue) will be denoted as the secondary channel.

Using ArcMap, we compared the depths of the channel complexes to the geometry of the plume inferred from the CPT and well data. Figure 12 shows a map view of the contoured channel complex depths on top of the TCE plume concentration map. Good well-data coverage of the TCE concentrations east of and within the seismic survey area allows for higher confidence in the plume concentration map. The deepest parts of the channel complex are near the POS wells. The plume source is located to the right in Figure 12 and flows from east to west on the map but narrows near the POS wells. Of note is a linear feature of the primary channel of depths (22–25 m) that trends north–south within the survey area in the vicinity of the POS wells. Although part of the linear trend may be caused by the depth conversion contouring in ArcMap, we believe that this feature is geologic because it is supported by the well data that illustrate (Figure 4) a difference in thickness of the

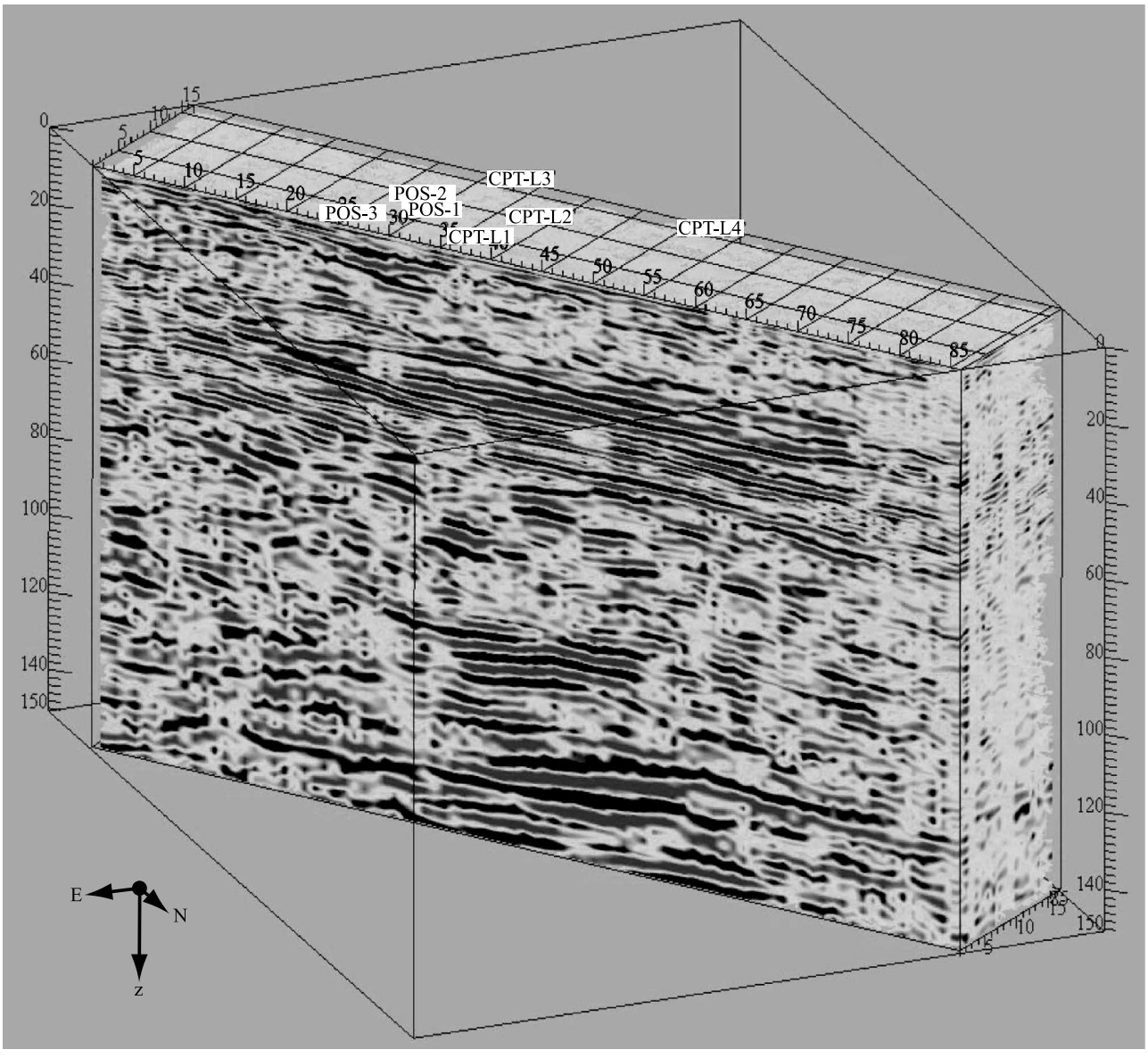

Figure 9. Final processed 3-D volume of the seismic reflection data. Volume dimensions are 170 by 34 by 150 m (558 × 111 × 492 ft). CPT = cone penetrometer. Position (POS) wells 1, 2, and 3 are also shown.

middle clay unit between POS-3 and CPT-L1. The narrowing of the plume within the seismic survey area corresponds to the linear feature of the deepest part of the primary channel.

DISCUSSION

Some of the significant results of this study are that (1) two new channel complexes, which are not present in the conceptual model, were identified in the upper 60 m of the section, and (2) the upper and middle clay units are not as continuous laterally as previously thought. The presence of these two channels is confirmed by the location of the TCE plume below the middle clay near well POS-3 and the presence of gravel deposits in the core samples taken from the POS wells.

In Figure 12, the geometry of the primary channel has been transposed over the plume to investigate potential correlations between the shape of the plume and the presence of the primary channel. From the spatial relationship between the TCE plume and the mapped channels, the primary channel appears to act like a conduit for the TCE plume by causing a change (narrowing) in the shape of the plume. Looking at the hydrogeological aspects of this geometry, the plume's trajectory

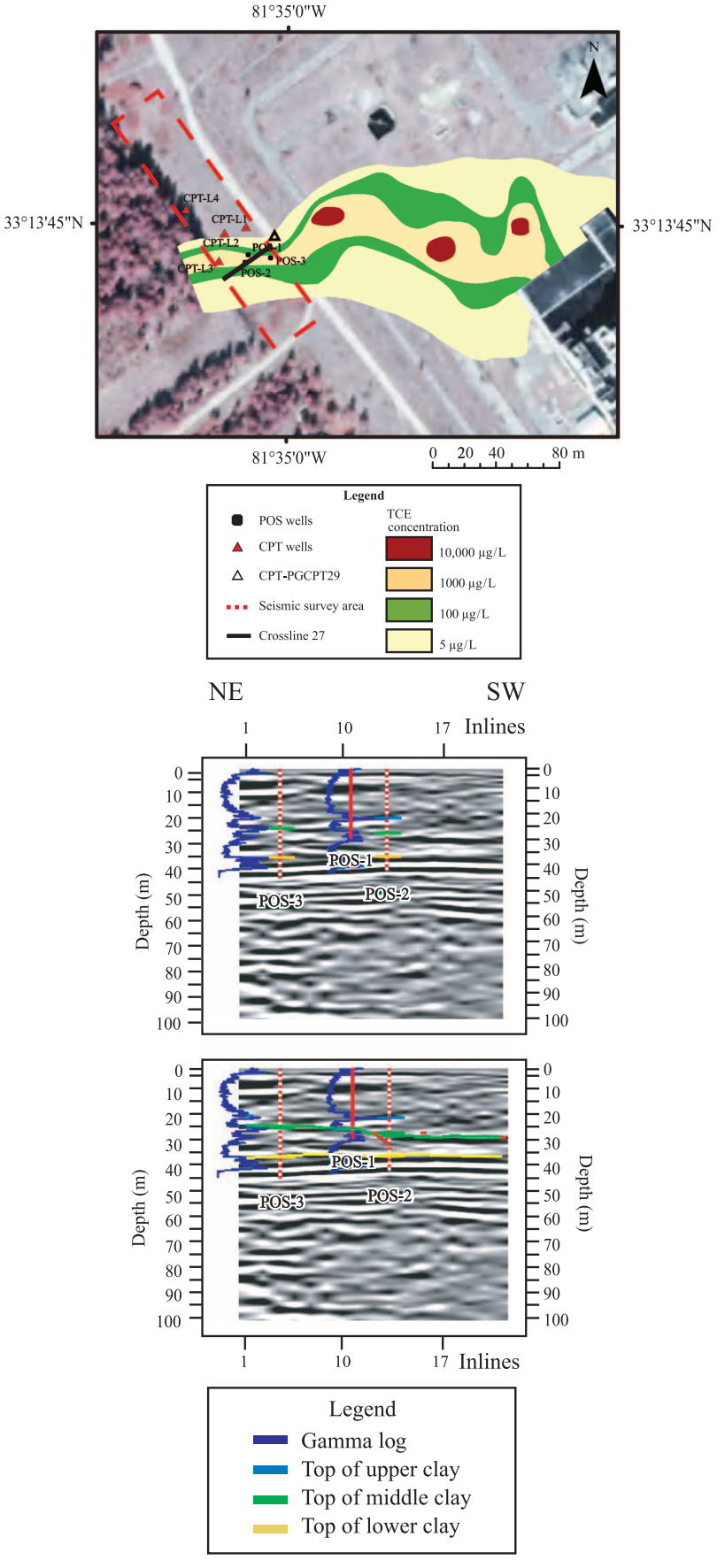

Figure 10. Crossline 27 is oriented in the same direction as Figure 3. The yellow horizon is the top of the lower clay and the green horizon is the top of the middle clay. The blue horizon located on well POS-2 is where the top of the upper clay should be if it were present. CPT = cone penetrometer; TCE = trichloroethylene; POS = position well.

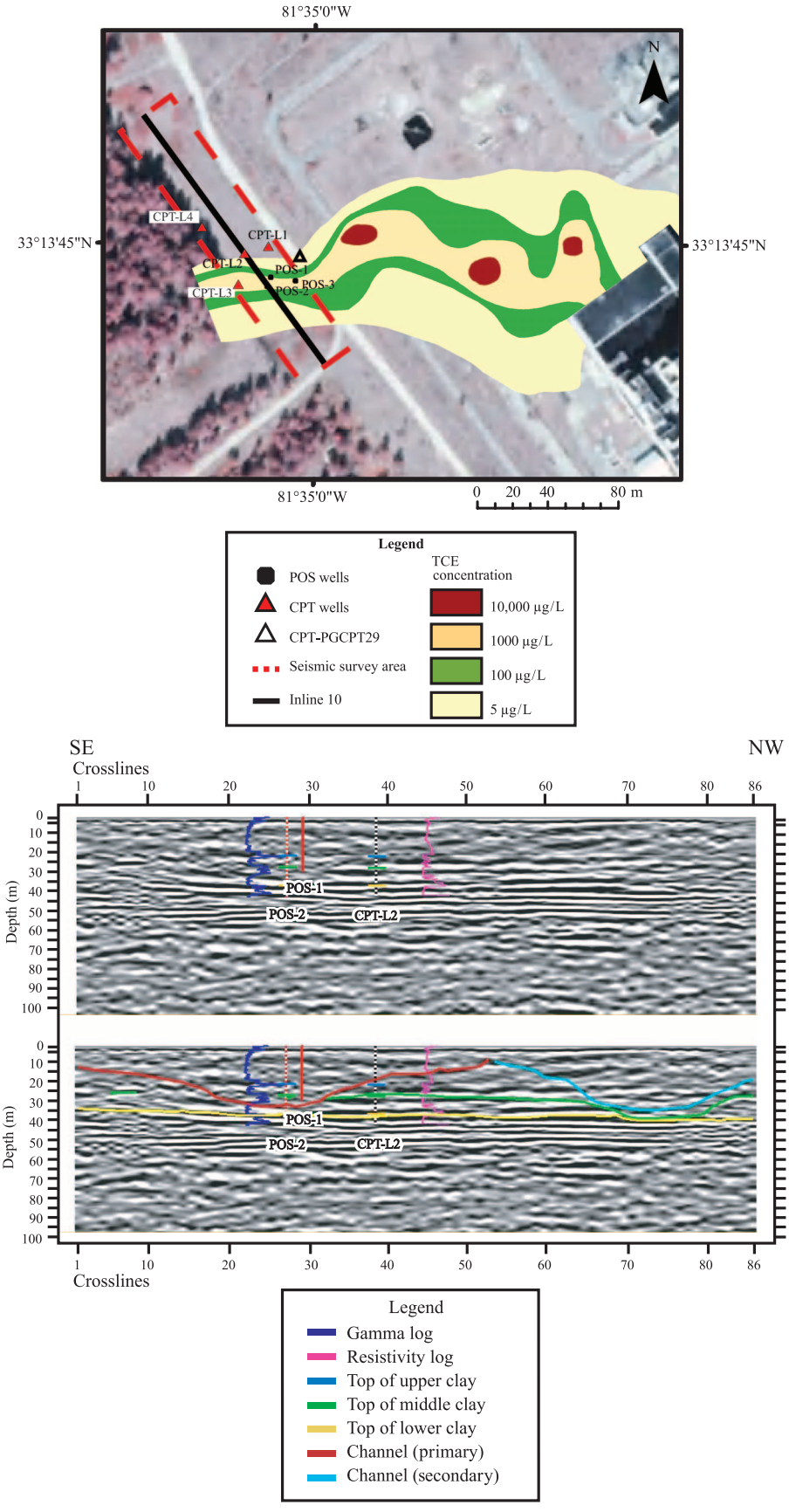

Figure 11. Inline 10 is oriented perpendicular to crossline 27. The yellow horizon is the top of the lower clay, the green horizon is the top of the middle clay, and the dark blue horizon is the top of the middle clay. The top of the upper clay appears to be absent on the seismic data. CPT = cone penetrometer; TCE = trichloroethylene; POS = position well.

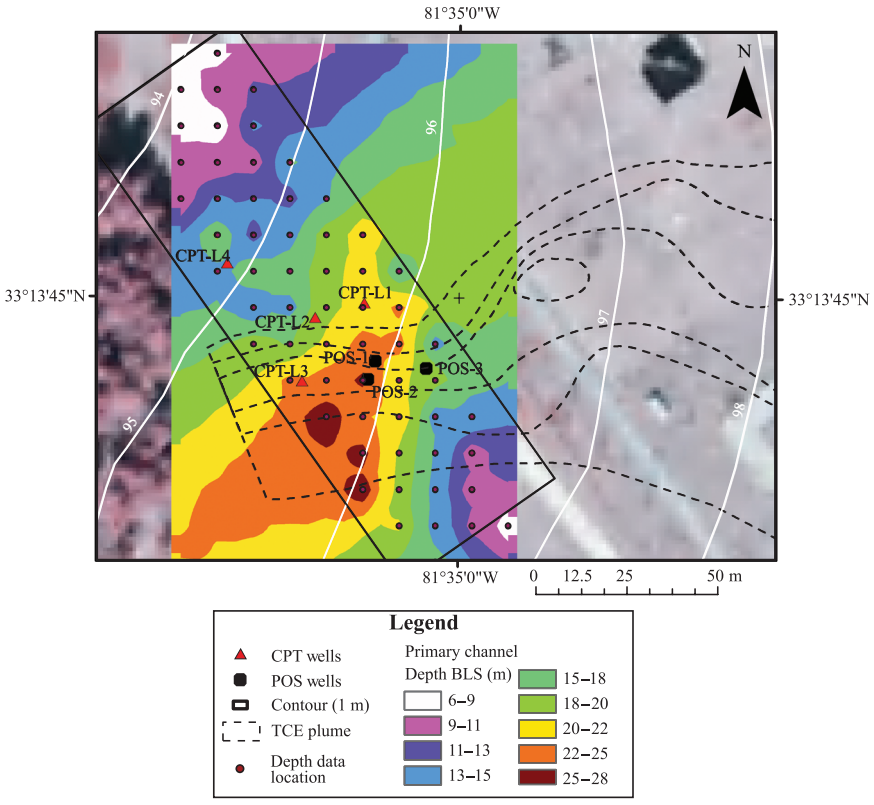

Figure 12. Isobaths of the two channel complexes gridded from the seismic data overlying the TCE concentration plume. The primary channel lies within the POS well cluster, whereas the secondary channel lies to the northwest. The deepest part of the primary channel lies to the east of POS-3 ranging from 22 to 28 m (72 to 92 ft) below land surface. CPT = cone penetrometer; TCE = trichloroethylene; POS = position well; BLS = below the surface.

appears to be controlled by the potentiometric surface whereas its shape could be controlled by the dispersion. Generally, with dispersion in typical porous media, the plume shape should become wider as it moves from the source point; however, here we see the opposite. A possible explanation could be that the channel is a conduit for the plume migration, which is consistent with the potentiometer data that indicate a convergence of groundwater flow (parallel to the primary channel) near the area northwest of the POS wells.

In the comparison between the initial conceptual model and the new conceptual model with the addition of the seismic data, some significant differences that also provide an explanation for the geometry of the plume migration are observed. The initial conceptual model was a simplified geologic characterization of the subsurface based on well data only. Although well data are important, they only provide point data, which are difficult to use when addressing a 3-D problem. The initial conceptual model consisted of continuous horizontal layering of the stratigraphy, whereas the seismic data show two channels that incise the horizontal layering.

In terms of further work with the existing 3-D data, we plan to derive seismic attributes, such as acoustic impedance, and see how they correlate with the geology and hydrogeology at the study area. The seismic attributes will be integrated with the other hydrogeophysical data and used in the modeling part of the project. We will also look at methods of improving our processing to improve the accuracy of any hydrogeophysical parameters estimated from the data such as porosity and hydraulic conductivity.

CONCLUSIONS

The P-reactor area at the SRS is located in South Carolina along the border with Georgia, consisting of 350-m-thick (1148-ft-thick) consolidated sands, clays, and gravels of the Atlantic coastal plain. The TCE was discovered at the site, and a conceptual model was created from previous works and well data. When characterizing a contaminated site, one has to develop a conceptual model to locate potential pathways for contaminant migration. These conceptual models generally are based on limited well data, tend to be simplistic, and in some cases do not properly represent the subsurface geology. A pseudo 3-D P-wave seismic reflection survey (34 × 170 m; 111 × 558 ft) was collected and processed in developing a more robust conceptual model for site characterization at the P area as part of a multiscale resolutions hydrogeophysical project.

The results of the seismic survey indicate that at least two significant revisions of the conceptual model are needed, one related to the spatial continuity of the upper and middle clay units and the other one related to the discovery of two buried channels in the study area. The seismic data show not only that the upper and middle clay units are not continuous as previously thought, but that two buried channels that were not illustrated in the conceptual model are present. We were able to take the geometric information from the channel complexes from the seismic data and integrate it with the map view of the plume data for comparison. The comparison illustrated that the primary (southeast) channel correlates well with the shape of the plume near the well cluster, suggesting that the channel may influence the plume migration that is at odds with the general stratigraphy. Overall, the pseudo 3-D seismic data have enhanced our understanding of the subsurface geology at the P area by providing additional information to the conceptual model.

REFERENCES CITED

Aadland, R. K., J. A. Gellici, and P. A. Thayer, 1995, Hydrogeologic framework of west-central South Carolina: Report to the South Carolina Department of Natural Resources, Water Resource Division, 200 p.

Cordsen, A., J. W. Peirce, and M. Galbratith, 1995, Planning and operating a land 3-D seismic survey: Society of Exploration Geophysicists, Continuing Education Program, p. 5.1–5.34.

Fallaw, W. C., and V. Price, 1995, Stratigraphy of the Savannah River site and vicinity: Southeastern Geology, v. 35, no. 1, p. 21–58.

Jean, G., J. M. Yarus, M. K. Harris, G. P. Flach, M. Millings, and F. Syms, 2002, 3-D geological modeling of the general separations area, Savannah River Site: Westinghouse Savannah River Company, p. 14–19.

Millings, M., K. Vangelas, and M. Harris, 2003, Source term determination for P-area reactor groundwater operable unit: Westinghouse Savannah River Company, Savannah River Site, Westinghouse Savannah River Company-TR-2003-00142, 1 p.

Reilly, T. E., and A. W. Harbaugh, 2004, Guidelines for evaluating ground-water flow, models: U.S. Geological Survey Scientific Investigations Report 2004-5038, Reston, Virginia, 1 p.

Rex, R., B. Goodway, C. Martin, and G. Uswak, 2003, The impact of azimuthal anisotropy AVO and petrophysical response in a fracture Wabamun gas reservoir (abs.): Canadian Society of Exploration Geophysicists/Canadian Society of Petroleum Geologists, p. 3–4.

Sheriff, R. F., and L. P. Geldart, 1995, Exploration seismology, 2d ed.: New York, Cambridge University Press, 244 p.

Stone, D. G., 1994, Designing seismic survey in two and three dimensions: Geophysical References: Tulsa, Oklahoma, Society of Exploration Geophysicists, no. 5, 141 p.

Wyatt, D. E., 2000, Savannah River site overview and general site information, *in* D. E. Wyatt and M. K. Harris, eds., Carolina Geological Society 2000 Field Trip Guidebook: Durham, North Carolina, Duke University, p. A9–A48.

Yilmaz, O., 1987, Seismic data processing: Investigations in geophysics, 2d ed.: Tulsa, Oklahoma, Society of Exploration Geophysicist, 69 p.

Structural and stratigraphic control on the migration of a contaminant plume at the P Reactor area, Savannah River site, South Carolina

Antonio E. Cameron González, Camelia C. Knapp, Michael G. Waddell, Adrian D. Addison, and John M. Shafer

ABSTRACT

Geophysical methods, including a shallow seismic reflection (SSR) survey, surface and borehole ground-penetrating radar (GPR) data, and electrical resistivity imaging (ERI), were conducted at the Savannah River site (SRS), South Carolina, to investigate the shallow stratigraphy, hydrogeophysical zonation, and the applicability and performance of these geophysical techniques for hydrogeological characterization in contaminant areas. The study site is the P Reactor area located within the upper Atlantic coastal plain, with clastic sediments ranging from Late Cretaceous to Miocene in age. The target of this research was the delineation and prediction of migration pathways of a trichloroethylene (TCE) contaminant plume that originates from the northwest section of the reactor facility and discharges into the nearby Steel Creek. This contaminant plume has been migrating in an east-to-west direction and narrowing away from the source in an area where the general stratigraphy along with the groundwater flow dips to the southeast. Here, we present the results from a stratigraphic and hydrogeophysical characterization of the site using the SSR, GPR, and ERI methods. Although detailed stratigraphic layers were identified in the upper approximately 50 m (164 ft), other major findings include (1) the discovery of a shallow (~23 m [75 ft] from the ground surface) inverse fault, (2) the detection of a paleochannel system that was previously reported but that seems to be controlled by the reactivation of the interpreted fault, and (3) the finding that the hydraulic gradient seems to have a convergence of groundwater flow near the area. The interpreted fault at the study site appears to be of upper Eocene age and may be associated with other known reactivated faults within the Dunbarton

DOI:10.1306/eg.08180909012

AUTHORS

ANTONIO E. CAMERON GONZÁLEZ ~ *Department of Earth and Ocean Sciences, University of South Carolina, 701 Sumter St., EWS 617, Columbia, South Carolina 29208; acameron@geol.sc.edu*

Antonio Cameron is a Ph.D. candidate in the Department of Earth and Ocean Sciences at the University of South Carolina. He received M.S. and B.S. degrees in geology from the University of Puerto Rico at Mayagüez and worked for 3 years as a researcher in the Puerto Rico Seismic Network. His research interests include exploration and environmental geophysics, earthquake seismology, and geostatistics.

CAMELIA C. KNAPP ~ *Department of Earth and Ocean Sciences, University of South Carolina, 701 Sumter St., EWS 617, Columbia, South Carolina 29208*

Camelia Knapp received a Ph.D. in geophysics from Cornell University and B.S. and M.S. degrees in geophysical engineering from the University of Bucharest (Romania). She worked with the Romanian State Oil Company and the National Institute for Earth Physics. Currently at the University of South Carolina in the Department of Earth and Ocean Sciences, her research interests include exploration and environmental geophysics, crustal-scale seismology, and gas hydrates.

MICHAEL G. WADDELL ~ *Earth Sciences and Resources Institute, University of South Carolina, 1233 Washington St., Suite 300, Columbia, South Carolina 29208*

Michael Waddell completed his graduate studies at Earth Sciences and Resources Institute-University of South Carolina (ESRI-USC), in 1982 and remained at ESRI-USC until 1984 when he became a reservoir geologist in Houston working on petrographic investigations of hydrocarbon reservoirs worldwide. In 1986, he returned to ESRI-USC to start an environmental geophysics group and is presently its manager.

ADRIAN D. ADDISON ~ *Earth Sciences and Resources Institute, University of South Carolina, 1233 Washington St., Suite 300, Columbia, South Carolina 29208*

Adrian Addison received his Ph.D. in geological sciences from the University of South Carolina.

He received a B.S. degree in geophysics from the University of Oklahoma and worked for 4 years as a geophysicist with the U.S. Geological Survey. He recently joined ESRI-USC as a researcher associate, and his research interests include borehole and near-surface geophysics, environmental geology, and signal processing.

JOHN M. SHAFER ~ *Earth Sciences and Resources Institute, University of South Carolina, 1233 Washington St., Suite 300, Columbia, South Carolina 29208*

John Shafer received his Ph.D. in civil engineering from Colorado State University, his M.S. degree in resource development from Michigan State University, and his B.S. degree in earth science from Penn State University. His research focus includes integrated site characterization, coupled simulation-optimization approaches to solving groundwater problems, and groundwater susceptibility and contamination potential analysis.

ACKNOWLEDGEMENTS

We thank Duke Brantley from the Earth Sciences and Resources Institute; Susan Hubbard, John Peterson, Michael Kowalsky, and Kenneth Williams from Lawrence Berkeley National Laboratory; and Gregg Flach, Marry Harris, and Margaret Milling from Savannah River National Laboratory. Special thanks go to James Knapp and Jose Manuel Bacale as well as to the Geophysical Exploration and the Tectonics Geophysical Laboratories from the Department of Earth and Ocean Sciences at the University of South Carolina. We also acknowledge Landmark Graphics Corporation, Seismic Micro-Technology Inc., and Environmental Systems Research Institute (ProMax®, Kingdom® Suite and ArcGISTM software packages) for the University Grants Programs. This work was made possible through a grant by the Office of Science-Biological and Environmental Research of the U.S. Department of Energy (grant DE-FG02-06ER64210).

Triassic Basin. The coincident use of the SSR and ERI methods in conjunction with the complementary 50-, 100-, and 200-MHz GPR antennas allowed us to generate a detailed geologic model of the shallow subsurface, suggesting that the migration of the TCE plume is constrained by (1) the paleochannel system with respect to its migration direction, (2) the presence of an inverse fault that may also contribute to the paleochannel growth and structural evolution, and (3) the local groundwater flow volume with respect to its longer and narrower shape away from the source updip stratigraphic bedding.

INTRODUCTION

An integrated surface and borehole geophysical investigation, including a shallow seismic reflection (SSR), surface and borehole ground-penetrating radar (GPR), and electrical resistivity imaging (ERI) surveys, were conducted at the P Reactor area, Savannah River site (SRS), South Carolina, to assess the local shallow stratigraphy and structural geology and to test the viability of the combined methods in an area with interspersed sand and clay layers and where the general stratigraphic dip along with the regional groundwater flow is to the southeast (Figure 1). Precharacterization efforts within the study area revealed that the groundwater is primarily contaminated with volatile organic compounds and tritium (Millings et al., 2003). Several contaminant plumes have been identified, and the plume of interest contains trichloroethylene (TCE) that originates from the northwest section of the reactor facility and discharges into the nearby Steel Creek. Moreover, despite the stratigraphic layers having a slight northwest–southeast dip in the study area (Snipes et al., 1993), the contaminant plume seems to flow updip and narrows away to the west from the source area instead of showing an expected broadening pattern and flow migration to the southeast (Figure 2). The P Reactor area at SRS, which is a Department of Energy facility encompassing about 300 mi^2 (777 km^2) of land, lies within the upper Atlantic coastal plain (UACP), a southeast-dipping wedge of unconsolidated and semiconsolidated sediments that extend from its contact with the Piedmont Province at the Fall Line to the edge of the continental shelf (Figure 1). The sedimentary cover (<100 m [328 ft]) ranges from the Paleocene to Miocene in age and comprises layers of sand, muddy sand, and mud with minor amounts of calcareous sediments (Siple, 1967; Marine, 1974; Fallaw et al., 1990; Colquhoun and Muthig, 1991; Nystrom et al., 1991; Sohl and Owens, 1991; Fallaw and Price, 1992, 1995) (Figure 3).

Combined geophysical methods such as SSR, GPR, and ERI have been used in the identification of shallow sediments (<100 m [328 ft]) in different applications such as environmental, hydrological, geotechnical, and engineering studies (Wyatt et al., 1996). Indeed, detection of shallow porous layers, characterization of sediments and shallow layering, recognition of bed rocks, examination

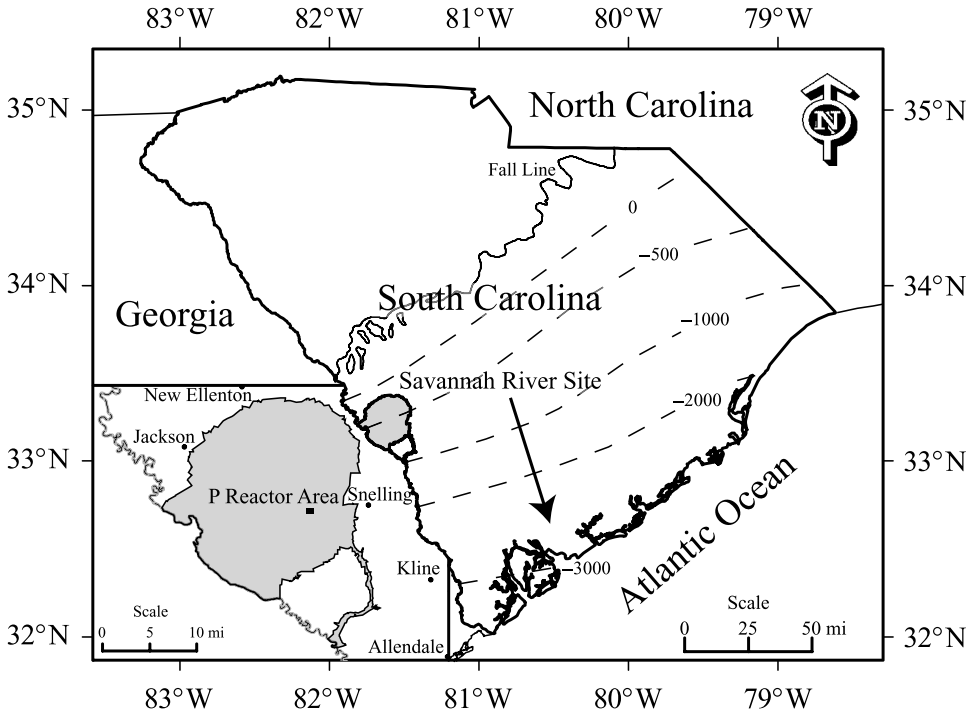

Figure 1. Location map of the P Reactor area at Savannah River site (SRS), west-central South Carolina. The approximate altitude of the basement rock surface in the Atlantic coastal plain is also shown (dashed lines) (from Cederstrom et al., 1979). Contour interval is in feet. The general stratigraphic dip of coastal plain sediments and regional groundwater flow (black arrow) is to the southeast (Aucott, 1996).

of aquifers, and/or location of buried objects and structural features such as faults are some examples of primary interest in shallow subsurface applications, especially in areas with near-surface contamination. In many geological environments, SSR, GPR, and ERI are effective methods for imaging near-surface boundaries due to variations in stratigraphy and in electromagnetic (EM) properties, obtaining detailed, horizontally continuous information about the near subsurface without resorting to invasive and expensive drilling (Neal, 2004). Geologic complexity such as cross-stratification, conflicting dips, joints and faults, or rapid lateral and vertical particle-size variations pose a challenge in the interpretation of the shallow stratigraphy using SSR, GPR, and ERI methods (Wyatt and Temples, 1996; Baker et al., 2001; Gross et al., 2004; Clement et al., 2006). However, the use of a combination of these methods generally improves the chances for a more accurate geologic interpretation.

Seismic reflections arise from changes in seismic-wave velocity and mass density. In contrast, GPR reflections (or near-surface EM boundaries) may be generated by changes in the dielectric permittivity, magnetic permeability, and/or electrical conductivity caused by variable moisture content within a clastic unit, or simply by lithologic variations. Regularly, GPR methods are used to image the upper 10 m (33 ft) of the earth to reconstruct past depositional environments and the nature of sedimentary processes in a variety of geologic settings except where electrical conductivity is uncommonly low, which allows the radar signal to penetrate more deeply. Thus, EM parameters (i.e., dielectric permittivity, magnetic permeability, and electrical conductivity) may change across an interface when bulk density, seismic-wave velocity, and/or resistance to current flow remain constant. However, EM parameters may remain unchanged across an interface when these other physical properties vary. As a result, resistance anomalies would appear in the ERI but not in the GPR data.

In ERI methods, direct current or low-frequency alternating current is applied to the ground surface, and the potential difference is measured between two points. Variations in resistance to current flow at depth cause distinctive variations in the potential difference measurements, which provide information about the subsurface structures and materials. Although these techniques work well in near-surface investigations and are quite similar in terms of how the active energy is applied to the earth, GPR still offers the highest potential resolution of the three methods for shallow imaging in low EM loss materials (Baker et al., 2001).

In site characterization, near-surface geophysical surveys at different resolution scales are critical to model the heterogeneity of the shallow subsurface. These noninvasive geophysical methods respond to changes in the material composition and pore fluid

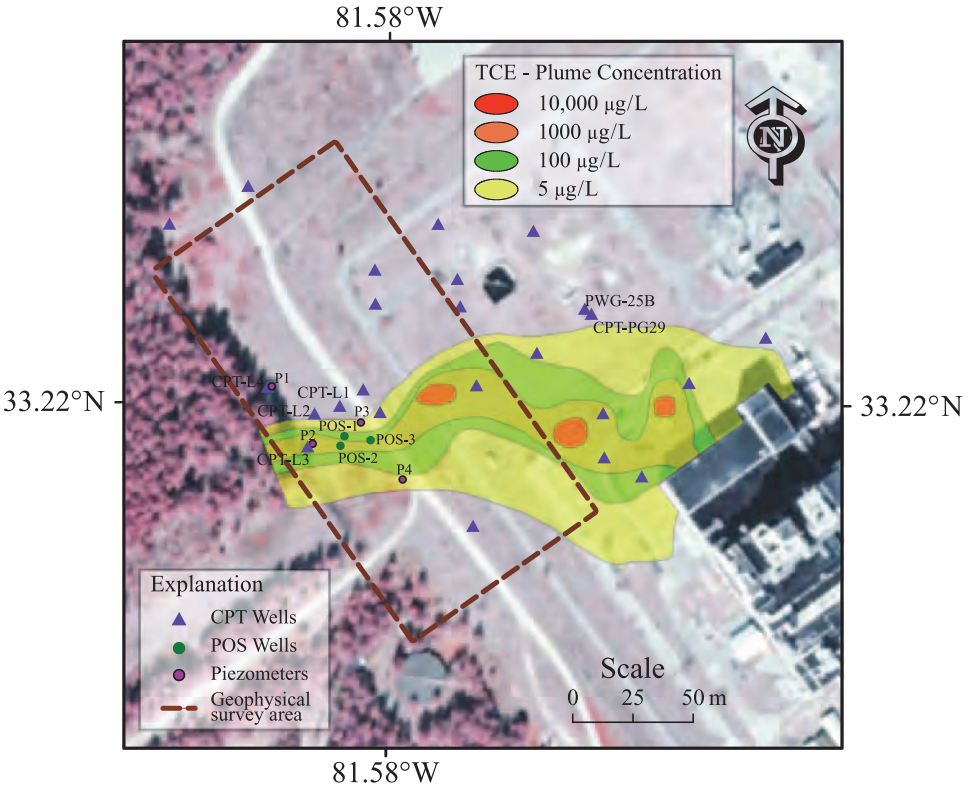

Figure 2. Lateral extension of the trichloroethylene (TCE) plume that originates from the northwest section of the P Reactor facility and discharges into the nearby Steel Creek (west of the study area). The brown dashed line is an outline of the geophysical survey area. The plume map shows concentration ranging from 5 to 10,000 µg/L and were determined from cone penetrometer tests (CPTs) and well data (blue triangles and green dots). Note that the highest TCE concentrations are not very well constrained because of the sparse coverage of the CPT wells. Core and natural gamma logs (POS wells; POS stands for position) as well as four piezometers (magenta dots) for potentiometric surface data used in this investigation are also shown.

of the subsurface, therefore, corresponding and complementary imaging of the subsurface can be achieved by these three methods. Moreover, they have the potential to provide more cost-effective and reliable information for performance monitoring of contaminated site characterization.

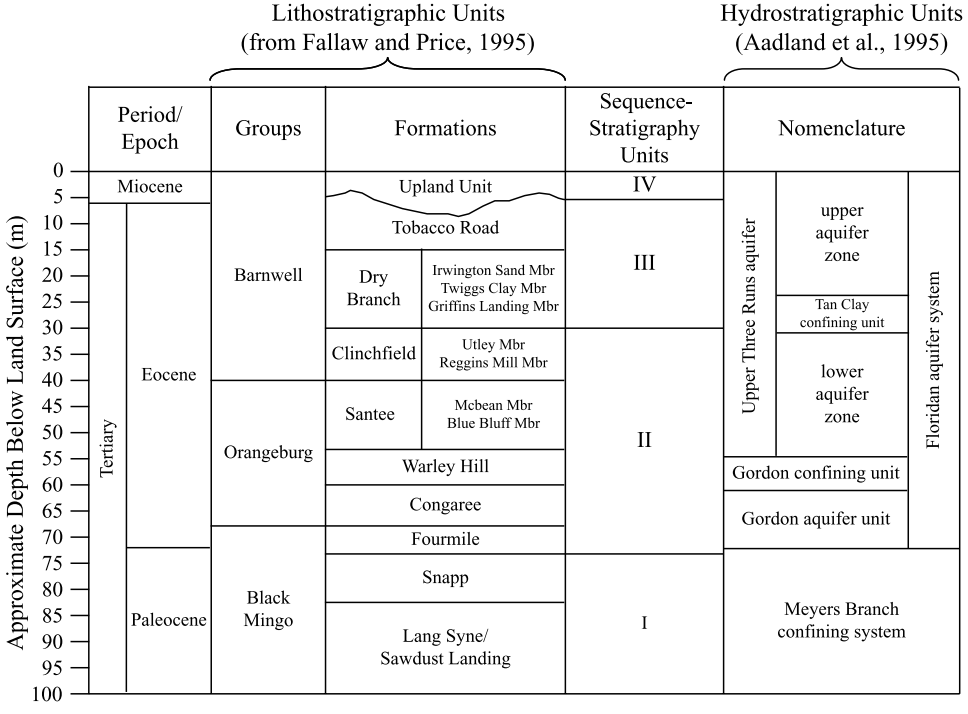

Figure 3. Shallow stratigraphic units, including lithostratigraphy (modified from Fallaw and Price, 1995), sequence stratigraphy, and hydrostratigraphy (modified from Aadland et al., 1995) for the SRS region.

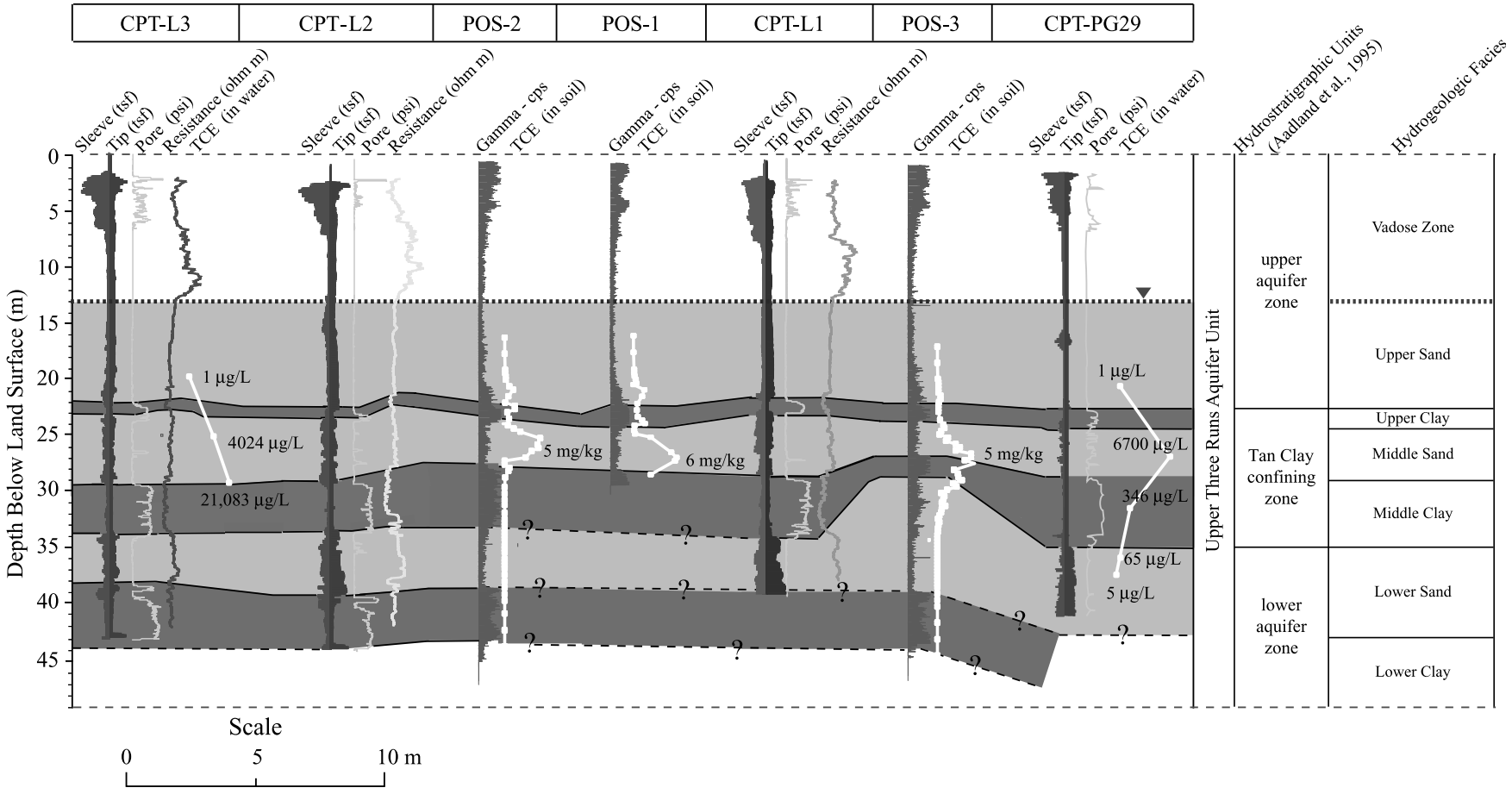

Figure 4. Cone penetrometer tests (CPT) and natural gamma log correlation with hydrostratigraphic units and hydrogeologic facies for our study area (modified from Addison et al., 2009). The water table is approximately at 13-m (43-ft) depth dividing the upper Three Runs aquifer into seven hydrogeologic facies. Wyatt et al. (2000) indicated that the upper aquifer zone consists of massive beds of sand and clayey sand with minor interbeds of clay, the Tan Clay confining zone contains light-yellowish tan to orange clay and sandy clay interbeded with clayey sand and sand, and the lower aquifer zone is composed of siliciclastic and calcareous sediments of the Santee Formation and parts of the Dry Branch Formation. tsf = tons per square foot; TCE = trichloroethylene.

STUDY AREA AND HYDROGEOLOGIC SETTING

The shallow (~75 m [246 ft]) hydrogeologic units at SRS involve Tertiary-age sediments, mainly Eocene to Miocene in age (Figure 3). The updip part of the Floridan aquifer system includes the Gordon aquifer, the Gordon confining unit, and the upper Three Runs aquifer (UTRA) (Aadland et al., 1995). The UTRA includes the Upland unit, Tobacco Road Sand, Dry Branch Formation, Clinchfield Formation, and Santee Limestone. At the P Reactor area, the UTRA is informally divided in lower and upper aquifer zones (LAZ and UAZ) separated by the Tan Clay confining zone (TCCZ). For the purpose of this article, the UTRA has been divided among seven major hydrogeologic facies, which address specific characteristics for the UAZ, the TCCZ, and the LAZ (Figure 4).

The regional groundwater flow system in the Atlantic coastal plain of South Carolina is considered to be a stratified system (Aucott, 1996), where water enters the system as recharge in topographically high areas between rivers and lakes, flows southeast down the hydraulic gradient, and discharges to other rivers, lakes, swamps, and/or to the Atlantic Ocean. However, in a local spatial scale, based on potentiometric surface data from depth-discrete piezometers, the shallow groundwater in the study site appears to have a predominantly west to southwest flow direction.

Several studies of coastal plain geology at, and in the vicinity of, SRS (e.g., Higgins et al., 1978; Zoback et al., 1978; Behrendt et al., 1983; Hamilton et al., 1983; Schilt et al., 1983; Talwani, 1986; Shedlock and Harding, 1988; Snipes et al., 1993; Wyatt and Temples, 1996; Wyatt et al., 1996) have documented faults in the coastal plain sediments that appear to be closely related to the Mesozoic extensional basement structure. To recognize the coastal plain sediments as a layer-cake model is an oversimplification of an area where faulting is present in several localities. Based on seismic data from Behrendt et al. (1983) and Chapman and Di Stefano (1989), Cenozoic movements were documented above several Triassic basins in South Carolina that caused reactivation of Triassic normal faults as inverse faults.

DATA ACQUISITION AND PROCESSING

This study included (1) geophysical data collection and interpretation, (2) hydrogeophysical characterization of the study area, and (3) integration and analysis of site characterization results as they relate to the study of the TCE contaminant plume. The SSR survey was performed with a Geometrics 120-channel StrataView® seismograph, the surface and crosshole GPR data were acquired with the PulseEKKO 100 system by Sensors & Software, Inc. with 50-, 100-, and 200-MHz antennas, and the ERI was conducted with the SuperSting R8 IP with an 8-channel multielectrode resistivity system (Figure 5). Three cone penetrometer tests (CPTs) and three natural gamma logs with the associated core descriptions for three wells (POS-1, -2, and -3; POS stands for position) were provided by the Savannah River National Laboratory (SRNL) (Figure 4). These techniques and the subsequent results are described below.

Cone Penetrometer Tests and Natural Gamma Logs

The CPT is a subsurface soil exploration method that involves pushing a conical-shaped probe into a soil deposit and records sleeve frictions and tip resistance along with electrical resistivity, natural gamma, spontaneous potential, velocity data, piezometric values, and a variety of other geophysical parameters (Lunne et al., 1997). Natural gamma-ray measurements were used to characterize the rock or sediments in three boreholes (POS wells) by detecting variations in the natural radioactivity originating from changes in concentrations of the trace elements uranium (U) and thorium (Th) as well as changes in concentration of the major rock-forming element potassium (K). Because the concentrations of these naturally occurring radioactive elements vary between different rock types, natural gamma-ray logging provides an important tool for lithologic mapping and stratigraphic correlation. Natural gamma logs are sometimes used in mineral exploration and water-well drilling but most commonly for formation evaluation in oil- and gas-well drilling (Paillet and Ellefsen, 2005). The locations of the CPT and natural gamma logs (POS wells) are shown in Figure 2.

Shallow Seismic Reflection Data

A pilot two-dimensional (2-D) SSR survey was conducted at the study site during the summer of 2007 to provide larger depth control for the regional stratigraphic and structural geologic characterization and to serve as a calibration tool for a future three-dimensional

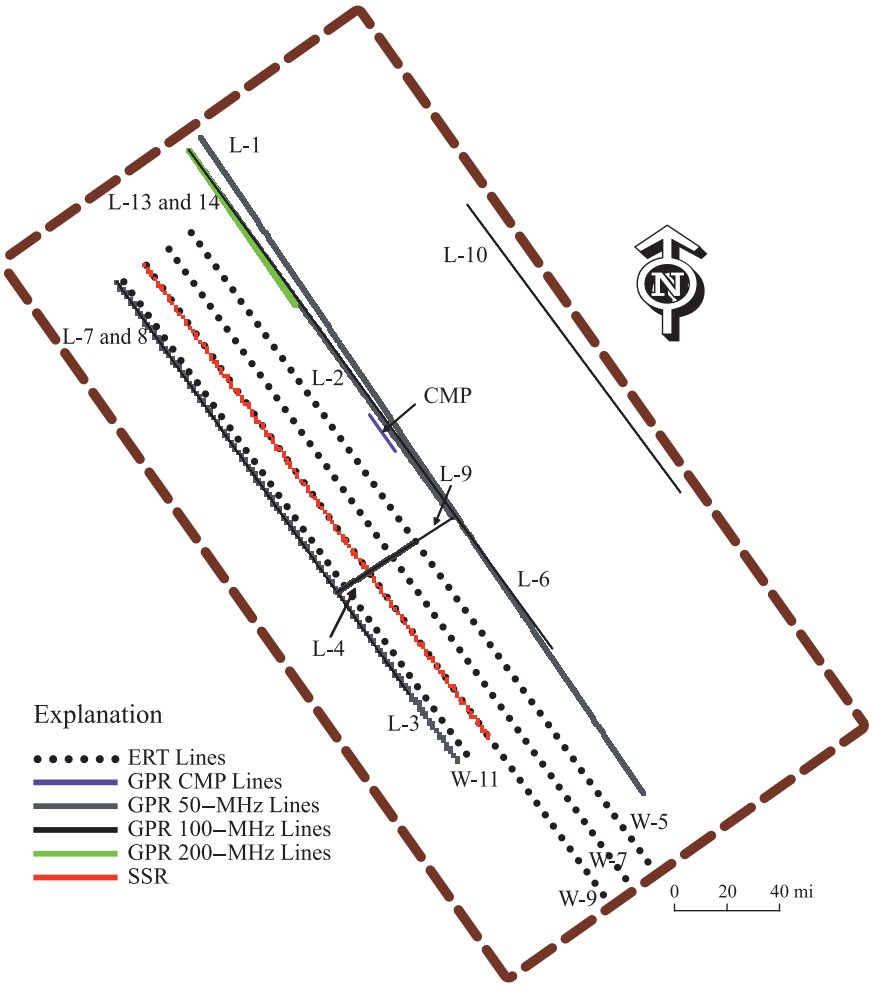

Figure 5. Layout of the shallow seismic reflection (SSR), ground-penetrating radar (GPR), and electrical resistivity imaging (ERI) lines.

(3-D) seismic reflection survey (Addison et al., 2009) (Figure 5). To improve the quality of the SSR data, several critical acquisition factors have been considered, including a fast sample rate (0.5 ms) and close spatial sampling (1 m [3 ft]) to improve the vertical and horizontal resolutions. The specific acquisition parameters for the SSR survey are shown in Table 1. The seismic data were processed with the Landmark Graphics' ProMax® software using the following sequence: (1) geometry assignment, (2) trace edits, (3) elevation statics, (4) top mute, (5) spherical divergence correction, (6) F-K filter, (7) bandpass filter, (8) deconvolution, (9) velocity analysis, (10) amplitude scaling, (11) normal move out and sectioning, (12) migration, and (13) time to depth conversion. Table 2 lists the processing sequence used in generating the final 2-D seismic section shown in Figure 6. The SSR line was imported for further interpretation along with the natural gamma and electrical resistivity logs from the POS and CPT wells into Kingdom® Suite.

Surface Ground-Penetrating Radar

Nine common offset GPR transects were acquired at the study site (Figure 5). In addition, two common-midpoint (CMP) gathers were used to identify reflection events

Table 1. Acquisition Parameters for the Shallow Seismic Reflection (SSR) Data Collected at the P Reactor Area, Savannah River Site, South Carolina

Acquisition Parameter	Value
Geophone spacing	1 m
Sample rate	0.5 ms
Record length	500 ms
10-ft sledge hammer	4 to 6 stacks
Total shots	170
Fold	30
Geophone frequency	40 Hz

Table 2. Generalized Processing Sequence in Generating the Final Seismic Section

Processing	Parameter
Geometry	Straight line geometry
Trace edits	Eliminated noisy traces
Elevation statics	Elevation corrections of stations
Top mute	Eliminated refraction arrivals
Spherical divergence correction	Applied 1/(time × [velocity]^2 function with a 0.0002 inelastic attenuation correction, a velocity function of 300 m/s for 100 ms and 1500 m/s between 100 ms, with a time-power constant of 1.4
F-K filter	Arbitrary polygon to reject ground-roll noise
Bandpass filter	Single filter Ormsby bandpass with corner frequencies of 50–100–300–400 Hz
Deconvolution	Spiking/predictive deconvolution using minimum-phase spiking with an operator length of 20 ms and an operator white noise label at 0.1 with a picked decon gate
Velocity analysis	Analysis from shot gathers, constant velocity sections with semblance plots
Amplitude scaling	10-ms operator length
Normal move out and sectioning	With sectioning velocities
Migration	F-K migration with maximum frequency to migrate of 300 Hz
Time/depth conversion	Used vertical seismic profiling velocities from the PGW-25B well to generate velocity profile
Import into Kingdom® Suite for interpretation	

on the common-offset GPR gathers and to determine EM wave velocities. Seven of these lines were oriented along the geologic strike of the underlying stratigraphy, and two were acquired perpendicularly for a pseudo 3-D control of the ground subsurface. All the GPR antennas were oriented parallel to each other and perpendicular to the survey line to obtain maximum overlap of the radar footprint along the profile (Annan and Davis, 1992). The specifications of the main acquisition parameters are listed in Table 3.

Processing of the GPR transects was performed with the Sensors and Software's, Inc. EKKOView Deluxe® and Landmark Graphics' ProMax® software packages. Most of the assumptions that apply to processing and interpretation of seismic reflection data also apply to surface GPR (Sangree and Widmier, 1979; Yilmaz, 1987, 2001). A general processing flow is detailed in Table 4 and includes the following flow: (1) WOW removal, (2) hand static corrections, (3) bandpass filter, (4) deconvolution, (5) migration, (6) time to depth conversion, and (7) amplitude scaling. The CMP velocities were used to migrate and convert to depth the time sections. Finally, the GPR transects were imported into the Kingdom® Suite software along with the 2-D SSR section, the natural gamma and resistivity logs for a more accurate interpretation.

Crosshole Ground-Penetrating Radar

The crosshole GPR field data analyzed in this study were collected between each pairs of POS-1, POS-2, and POS-3 wells (Figure 2). The POS-1 and POS-2 wells were approximately 6 m (20 ft) apart, the POS-2 and POS-3 wells were 15 m (49 ft) apart, and the POS-1 and POS-3 wells were 13 m (43 ft) apart. The depths of the wells ranged from 30 (POS-1) to 45 m (148 ft) (POS-2 and -3). The borehole antennas used for the crosshole survey had center frequencies of 50- and 100-MHz. The 100-MHz antennas were only used between POS-1 and -2 because of the relatively close separation distance between these two wells. The receiver antenna was moved every 0.25 m (0.82 ft). For each receiver location, the transmitter antenna was fired every 0.25 m (0.82 ft) as it was raised up the borehole. The resulting data set contains more than 21,000 traces. We only processed those traces where both the transmitter and receiver antennas were located entirely below the water table (based on water-level measurements to be approximately 13 m (43 ft) below the ground surface at the time of the survey).

To account for robust crosshole tomograms, we followed the recommendations provided by Peterson (2001) that include the following corrections: (1) drift

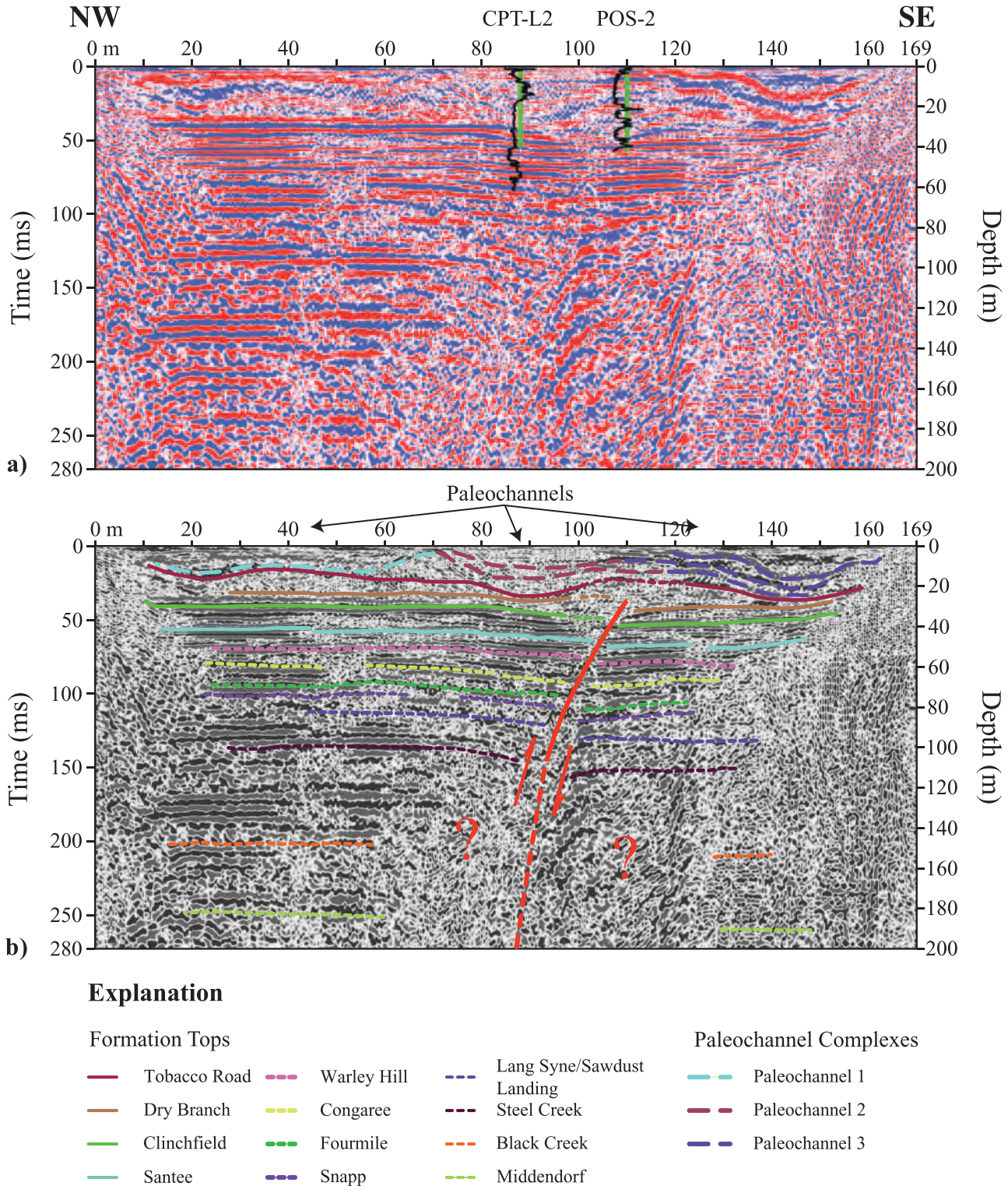

Figure 6. An uninterpreted (a) and interpreted (b) part of the shallow seismic reflection profile trending northwest–southeast in the study site confirming the presence of paleochannel complexes in the first 30+ m (98+ ft) depicted by the cyan, brown, and violet thick dashed lines (from Addison et al., 2009) and suggesting deeper faulting. Electrical resistivity (CPT-L3) and natural gamma (POS-2) logs used to calibrate the radar reflective horizons are also shown. Solid horizons correspond to formation tops from core data. Thin dashed horizons below 60-m (197-ft) depth correspond to formation tops inferred from the geology of the area. The sense of movement of the inverse fault is inferred from the reflectors adjacent to the interpreted fault and may be variable depending upon the amount of inverse motion. Poor resolution at the edges of the cross section is caused by the decreasing of fold coverage.

Table 3. Survey Parameters for 2-D Surface Ground-Penetrating Radar Acquisition as a Function of the Radar Antenna Frequencies Collected at the Study Site

Antenna Frequency (MHz)	Temporal Sampling Interval (ps)	Step Size (m)	Antenna Separation (m)	Expected Vertical Resolution (m)
50	1600	0.5	2.0	0.5–1.0
100	800	0.25	1.0	0.25–0.5
200	400	0.10	0.5	0.1–0.25

or discrete jumps in the zero time, (2) transmitter and receiver inaccurate geometry correction, (3) high-angle raypath correction, and (4) picked amplitude correction for geometric and radiation pattern. These corrections and processing steps were applied prior to the inversion of the crosshole data sets.

Electrical Resistivity Imaging

Surface resistivity is a well-known shallow geophysical tool and has been used in numerous environmental investigations, particularly in unconsolidated sediments (e.g., Pipan et al., 2003; Mota and Monteiro dos Santos, 2006; Wempe and Mavko, 2006). The ERI data collected involved the 2-D Wenner profiling method because the higher signal-to-noise ratio provided a good vertical resolution for subhorizontal layers as expected at this study site (Ward, 1990; Wyatt et al., 1996). Four Wenner configuration transects were acquired at the study site to provide a pseudo 3-D resistivity subsurface characterization (Figure 5). The same electrode configuration (4-m [13-ft] spacing) was used for each transect to improve the field logistics and to decrease the acquisition time.

RESULTS

The coincident use of the SSR and ERI methods in conjunction with the complementary GPR data using the 50-, 100-, and 200-MHz antennas allowed us to perform a detailed shallow stratigraphic characterization of the study site that is further needed for the contaminant plume geometry characterization and migration pathways. For the purpose of this study, we focused our characterization efforts in the upper 45 m (148 ft) of the ground subsurface where the TCE concentration is located (Figure 4). The water table depth during the geophysical surveys varied roughly between 12 and 14 m (39 and 46 ft) below the ground surface.

Table 4. Generalized Processing Diagram for Surface Ground-Penetrating Radar Data

Processing	Parameter
Download from GPR unit	
Import into EKKOView Deluxe®	
WOW removal	Removed unwanted electrostatic low frequency noise
Reformat to SEGY	
Import into ProMax®	
Hand static corrections	Used to specify and apply static shift corrections
Bandpass filter	Single filter Ormsby bandpass, corner frequencies varied with the antenna frequency used
Deconvolution	Spiking/predictive deconvolution using minimum-phase spiking with an operator length of 4 ns and an operator white noise label at 0.001 with a picked decon gate
Migration	Interval velocity in time from CMP gathers
Time/depth conversion	Used CMP gather velocities
Amplitude scaling	10-ns operator length
Import into Kingdom® Suite for interpretation	

The results of each geophysical technique were compared against and calibrated with the CPT and natural gamma logs.

Cone Penetrometer Tests and Natural Gamma Logs

Figure 4 shows a hydrogeologic cross section derived from the CPT and natural gamma logs in conjunction with the hydrostratigraphic units and hydrogeologic facies identified in the study area. The CPT curves L-1, L-2, and L-3 represent one-dimensional sleeve and tip friction, pore-pressure and electrical resistivity curves showing the sediments' shear strength, effective stress, and ability to conduct electrical current scaled in units of ohm meters. Natural gamma curves POS-1, -2, and -3 show the difference in radioactivity in counts per second between clays and sands. Both techniques showed good vertical resolution down to about 45-m (148-ft) depth. Changes in the electrical resistivity logs (CPT-L1, -L2, and -L3 wells) suggest a strong hydrologic change at approximately 13 m (43 ft), which was interpreted to be the water table. Based on a previous SRNL interpretation, the seven major hydrogeologic facies within the UTRA (i.e., vadose zone, upper sand, upper clay, middle sand, middle clay, lower sand, and lower clay) appear to be laterally continuous across the study area.

Shallow Seismic Reflection Data

The SSR data imaged well-defined subhorizontal reflectors from the surface to about 280 ms (200-m [656-ft] depth) (Figure 6). This part of the section represents the shallow UACP stratigraphy. Shallow formation tops were interpreted in correlation with the core data down to about 45-m (148-ft) depth. Deeper formation tops were interpreted from correlation with data presented in the literature (Fallaw and Price, 1995). These Tertiary formations range in age from early Paleocene to Miocene and were deposited in fluvial to marine shelf environments (Wyatt et al., 2000). The Tertiary sequence is divided into three groups, the Black Mingo Group, Orangeburg Group, and Barnwell Group, which are further subdivided into formations and members (Figure 2). These groups are overlain by the ubiquitous Upland unit.

Some of the significant findings from the SSR data include (1) a series of, at least three, paleochannel structures in the first 30+ m (98+ ft), (2) the hydrogeologic facies do not appear to be as continuous as previously thought by SRNL, and (3) the presence of a prominent near-vertical discontinuity in the subhorizontal reflectors at approximately 100-m (328-ft) distance from the northwestern end of the line that propagates from above about 25 m (82 ft) down to the bottom of the section and potentially to the crystalline basement. The three paleochannels were interpreted on the seismic section and they appear to incise the top of the Tobacco Road Formation (cyan, brown, and violet thick dashed lines in Figure 6b). Moreover, these paleochannel structures coincide with those imaged and documented by Addison et al. (2009). Based on the cross section derived from the CPT and natural gamma logs (Figure 4), the hydrogeologic facies appear to be continuous laterally across the study area. However, through a closer look, the upper sand, upper clay, and middle sand appear to be interspersed and truncated to one another. The imaged discontinuity is consistent with the interpretation of an inverse fault and appears to be associated with about 5-m (16-ft) vertical offsets in the reflectors (Figure 6b). The key shallow horizons imaging displacements up to approximately 5 m (16 ft) correspond to the Dry Branch Formation in the upper section through the Steel Creek Formation toward the bottom, thus, making the fault upper Eocene in age. The steeply dipping events imaged on the southeastern half of the seismic section may be diffractions from the fault plane.

Surface Ground-Penetrating Radar

Besides the SSR section, the surface GPR sections provided higher resolution and coherent reflectors for the first 16 m (52 ft) of the study site. The surface GPR data were converted from time to depth using interval velocity information provided by CMP gathers collected at the site (Figure 7). From the CMP survey, the EM velocity increases from 0.08 m (0.26 ft)/ns at 50 ns two-way traveltime (TWTT) to 0.09 m (0.29 ft)/ns at 225 ns TWTT, then decreases from 0.09 m (0.29 ft)/ns at 225 ns TWTT to 0.072 m (0.23 ft)/ns at 400 ns TWTT and from 0.05 m (0.16 ft)/ns at 650 ns TWTT to 0.04 m (0.13 ft)/ns at 750 ns TWTT. The propagation velocity of EM waves is a function of the dielectric constant of the subsurface, which in turn is affected by the water content. The subsurface reflections from the interfaces between layers with contrasting dielectric constants appear as hyperbolic events in the CMP section, whereas the air and ground waves are imaged as straight lines in the uppermost part of the CMP gather (Figure 7a).

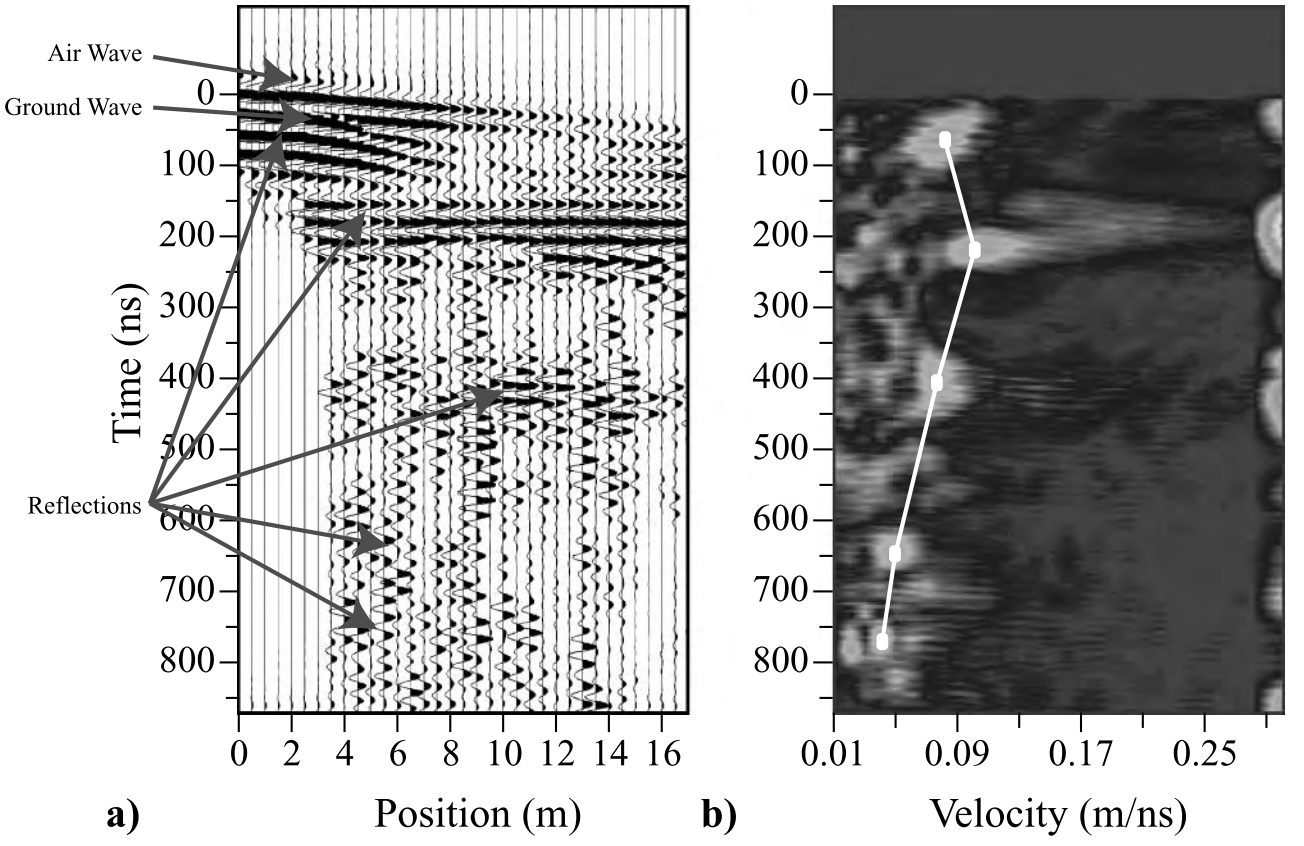

Figure 7. (a) Common-midpoint (CMP) radar gather at the study site. The uppermost two events are the air wave and the ground wave that appear to be highly attenuated beyond a horizontal distance of 10 m (33 ft). Subsurface reflectors are represented by hyperbolas. (b) Velocity profile derived from the CMP gather. Velocity is incremented in 0.001-m (0.003-ft)/ns steps from 0.01 to 0.29 m (0.03 to 0.95 ft)/ns. Dots indicate picked points of maximum coherence that define the velocity profile.

This characteristic shape is based on the assumption that the arrival time for signals from reflectors varies hyperbolically with the separation between the transmitter and the receiver antenna. The poor reflection quality may indicate that the energy is highly attenuated with depth. Figures 8, 9, 10, and 11 show some

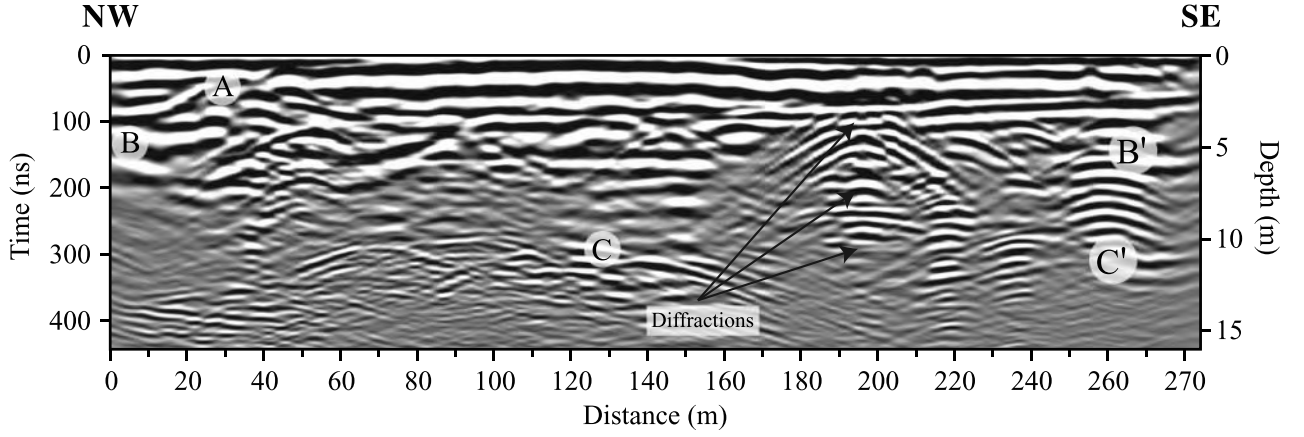

Figure 8. The GPR 50-MHz section (L-1) from the study site. Reflections are evident down to approximately 5-m (16-ft) depth along the northwestern end of the section. Diffractions appear to occur at 3- to 10-m (10- to 33-ft) depth. Reflections discussed in the text are labeled A, B, and C.

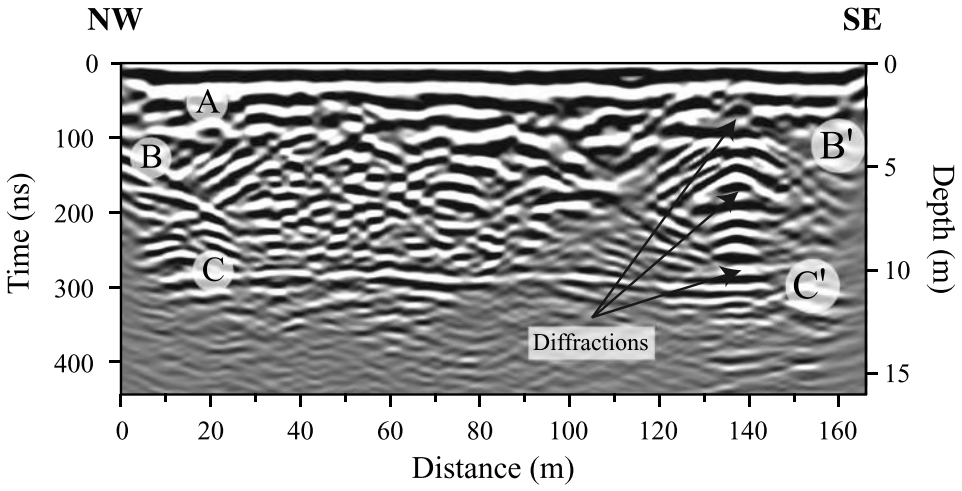

Figure 9. The GPR 50-MHz section (L-3) from the study site. Reflections are evident to 12-m (39-ft) depth along the section (e.g., A, BB′, and CC′). The strong reflection labeled C at 12-m (39-ft) depth belongs to the water table. Note diffraction hyperbolas at 3- to 10-m (10- to 33-ft) depth.

of the surface GPR surveys collected at the study site. Positions of these GPR lines are parallel with the locations of the CPT and POS wells. Line L-1 is shown in Figure 8. Strong coherent reflectors (A) are imaged from about 50 ns TWTT (3-m [10-ft] depth) on the northwestern side to about 100 ns TWTT (4-m [13-ft] depth) in the southeast. The EM energy is highly attenuated between approximately 200 and 300 ns TWTT (7–11-km [4.3–6.8-mi] depth). At 195-m (640-ft) distance from the northwestern end of the line, some diffractions occur with an apex at about 100 ns TWTT (e.g., 4-m [13-ft] depth). A reflector (B) at 150 ns TWTT (5-m [16-ft] depth) at the northwestern end appears on the profile at approximately 170-m (558-ft) distance. A strong reflector (B′), similar to reflector B, starts at about 250-m (820-ft) distance. A weakly coherent reflector (C) can be noticed at approximately 300 ns TWTT (12-m [39-ft] depth) in the 150 m (492 ft) of the section. The reflector ends at the same distance as reflector B. Other reflectors can be seen between approximately 300 and 400 ns TWTT to the southeast of 180-m (590-ft) distance, but they are not as coherent laterally but of poorer quality.

Line L-3 (Figure 9) is parallel to but approximately 40 m (131 ft) apart of line L-1 (Figure 8). The data quality for these two 50-MHz lines is very similar. Thus, the strong coherent reflectors labeled A in line L-1 are also interpreted on line L-3 but deeper in the section at about 300 ns TWTT compared to about 50 ns TWTT in L-1. Reflector B is highly disrupted by diffractions that occur at 140-m (459-ft) distance. However, reflector C, interpreted as the water table, appears

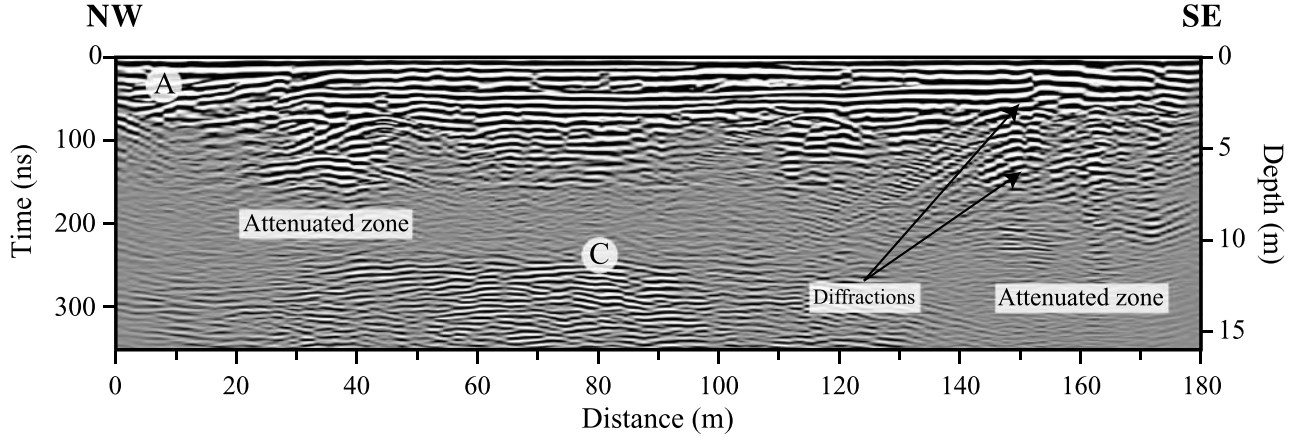

Figure 10. The GPR 100-MHz section (L-6) from the study site. The reflectors labeled A are strong, coherent, and continuous along the section. Weak reflectors at about 150 to 250 ns TWTT (7- to 12-m [23- to 39-ft] depth) at the northwestern side of the section indicate that the energy is attenuated. Label C denotes the water table reflector at about 12-m (39-ft) depth seen at every surface GPR line. Diffractions occur at 3- to 7-m (10- to 23-ft) depth.

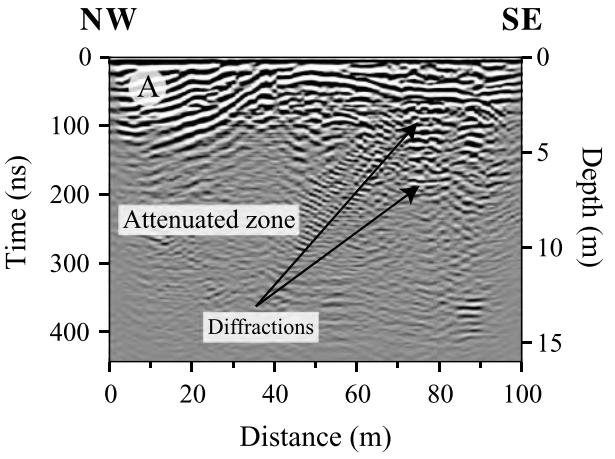

Figure 11. The GPR 100-MHz section (L-6) from the study site. The reflector package labeled A indicates a possible paleochannel structure that may correspond to that interpreted on the 2-D SSR section. Diffractions occur at about 50 and 150 ns TWTT (~3- to 7-m [10- to 23-ft] depth). The energy is strongly attenuated at times greater than approximately 125 ns TWTT (4-m [13-ft] depth).

to be strong, coherent, and continuous along the acquired section.

The surface GPR data quality decreased significantly upon increased antenna frequency. Figure 10 is a GPR section collected at the study site with the center antenna frequency of 100 MHz (line L-6). Poor depth penetration was expected due to the increasing frequency, but surprisingly, this GPR line shows prominent reflectors down to 16 m (52 ft) below the ground surface. The reflector package A seems to be stronger and more coherent than the same interpreted reflectors in lines L-1 and L-3 (Figures 8, 9). However, poor reflectivity contrast is seen at approximately 150 to 250 ns TWTT (7- to 12-m [23- to 39-ft] depth) in the northwestern side of the section. A strong reflection package is seen below approximately 220 ns (12 m [39 ft]) in the northwestern half of the section that is truncated laterally at about 130-m (426-ft) distance. Some diffractions are visible at 150-m (492-ft) distance and about 50 to 150 ns TWTT (3- to 7-m [10- to 23-ft] depth). The diffraction tails are shorter and of weaker amplitude than those in lines L-1 and L-3 (Figures 8, 9). Beneath these diffractions, the energy is strongly attenuated at times greater than approximately 150 ns TWTT (7-m [23-ft] depth).

Line L-10 (Figure 11) was also collected with the 100-MHz antennas. A paleochannel structure is evident at A and appears to be strong, coherent, and continuous through the section. Diffractions occur at 78-m (256-ft) distance at about 50 and 150 ns TWTT (3- to 6-m [10- to 20-ft] depth). The energy is strongly attenuated at times greater than approximately 125 ns TWTT (4-m [13-ft] depth). The water table reflector is not obvious in this section.

Geophysical and core data from CPT L-1, L-2, and L-3, and POS wells -1, -2, and -3 were used to calibrate the radar reflective horizons; however, other than reflectors A, B, and C that appear to be more coherent on the GPR lines, interpreting other deeper, coherent reflectors is difficult. The poor reflectivity contrast between some TWTT intervals throughout the surface GPR sections may be caused by the high clay content interfingered with sands that attenuated the radar signal. Additionally, anomalous or discontinuous reflection zones may be caused by changes in the dielectric constants and/or subsurface conductivity.

Crosshole Ground-Penetrating Radar

The tomographic analysis of the crosshole data used the raypath length of precise measurements of one-way traveltime to determine the velocity structure of the intervening materials. The inversions of the crosshole GPR data resulted in plots of EM wave velocity, attenuation, and conductivity. Because of the limited depth of the POS wells (~30–45 m [98–148 ft]), we only produced reliable tomograms for the upper 36 m (118 ft) of the wells (Figures 12, 13). Low EM wave velocity or higher attenuation is characteristic to high porosity and/or volumetric water content across the plane of investigation. Five hydrogeologic facies were interpreted on the tomograms between POS-1 and POS-2 and were subsequently compared against the CPT and natural gamma logs (Figure 12). The vadose zone in the UAZ approximately corresponds to the upper 13 m (43 ft) of the wells. The upper sand is approximately 8 m (26 ft) thick and correlates well with the CPT and natural gamma log data. The TCCZ with upper clay appears to be very thin (less than 2 m [6 ft]), the middle sand is approximately 6 m (20 ft) thick, and the middle clay is approximately 5 m (16 ft) thick and appears to dip toward the southeastern edge of the study site.

The tomographic inversion for the POS-1 and POS-3 wells (Figure 13) looks very similar to that of the POS-1 and POS-2 wells. The vadose zone of the UAZ corresponds to the upper 13 m (43 ft). The upper sand is 7 m (23 ft) thick, and the TCCZ with upper

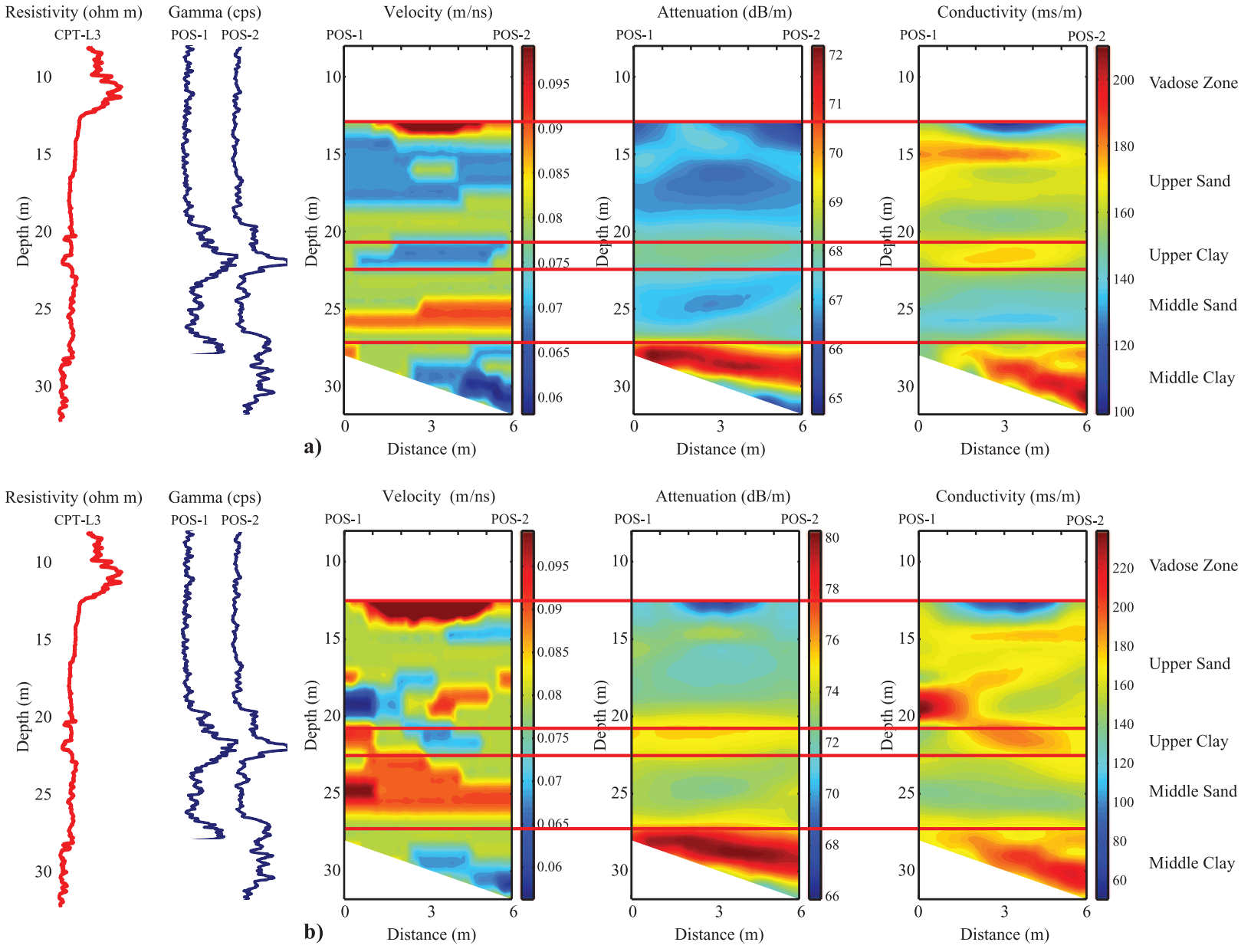

Figure 12. The 50-MHz (a) and 100-MHz (b) crosshole radar EM wave velocity, attenuation, and conductivity tomography plots between POS-1 (Tx) and POS-2 (Rx), showing interpreted hydrogeologic facies (i.e., vadose zone, upper sand, upper clay, middle sand, and middle clay) from data sets collected with the PulseEKKO 100 GPR system. The inverted tomograms were subsequently compared against electrical resistivity (CPT-L3) and natural gamma (POS-1 and -2) logs. The middle clay appears to dip toward the southeastern edge of the study site.

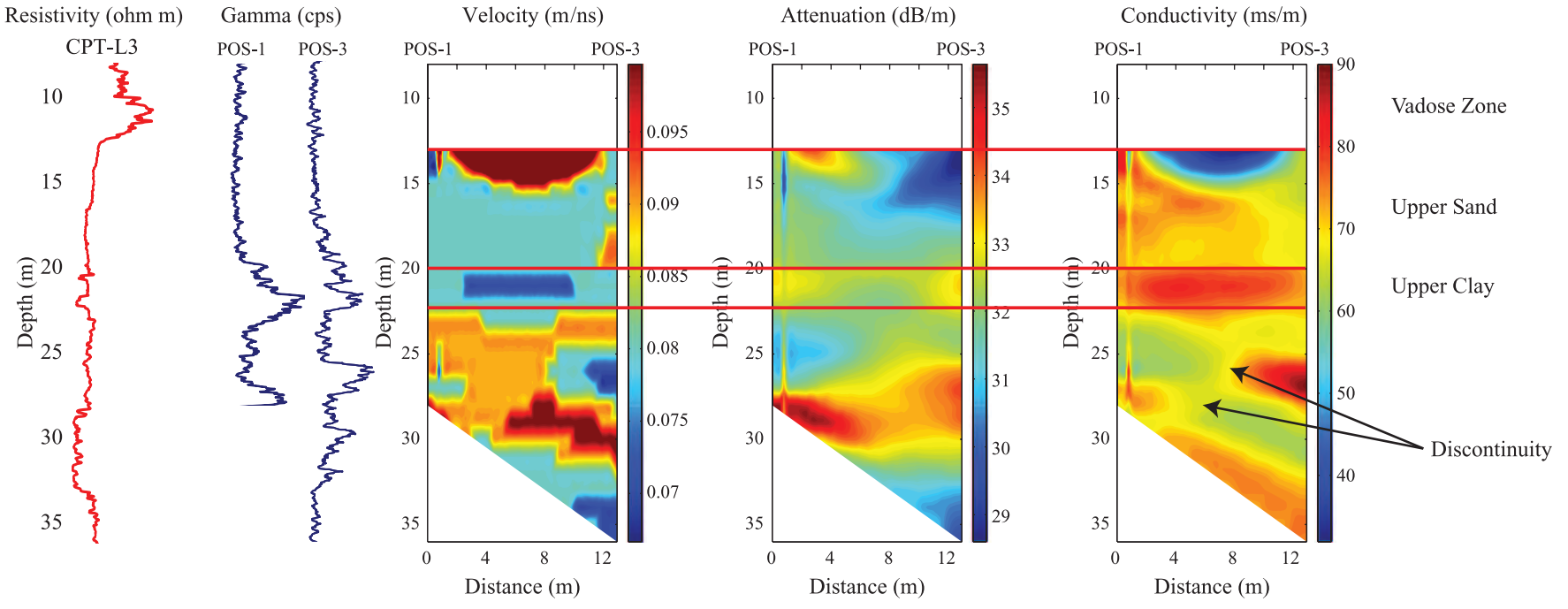

Figure 13. The 50-MHz crosshole radar EM wave velocity, attenuation, and conductivity tomography plots between POS-1 (Tx) and POS-3 (Rx). The inverted tomograms were subsequently compared against electrical resistivity (CPT-L3) and natural gamma (POS-1 and -2) logs. Note the prominent near-vertical discontinuity in the conductivity tomogram stating at 23-m (75-ft) depth.

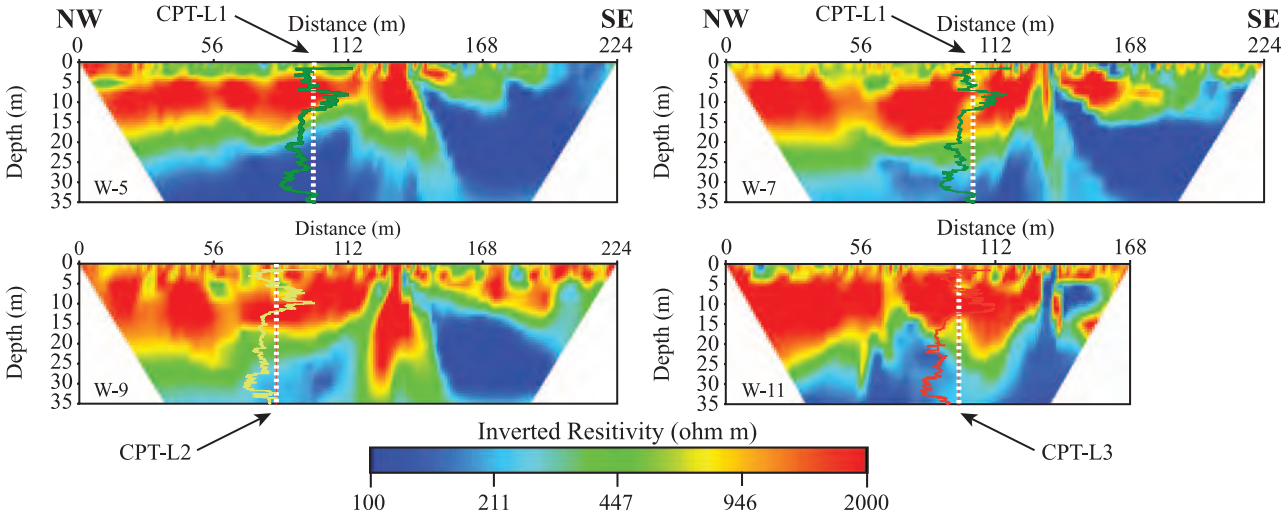

Figure 14. Comparison of the Wenner resistivity data with the CPT resistivity logs. Apparent resistivity values have been calibrated with CPT resistivity logs. Note the vertical low-resistivity discontinuity on each profile.

clay appears to be 2 m (6 ft) thin. However, below approximately 23-m (75-ft) depth, the middle sand and middle clay layers appear to discontinue. This significant discontinuity zone is delineated by the abrupt change in velocity, attenuation, and conductivity between the POS-1 and POS-3 wells (Figure 13) and it appears to correlate spatially with the discontinuity interpreted to be an inverse fault on the SSR section and/or the edge of a paleochannel.

Electrical Resistivity Imaging

The four electrical resistivity profiles collected at the study site with the Wenner array configuration provided high quality images down to about 35 m (115 ft) (Figure 14). The CPT logs were superimposed on the resulting resistivity tomograms as seen in Figure 14. The CPT resistivity logs correlate very well with the resistivity tomograms. The data along lines W-5, W-7, W-9, and W-11 were collected in parallel directions to the surface GPR and SSR surveys (Figure 5). The lengths of the lines were about 224 (W-5, W-7, and W-9) and 168 m (W-11) (735 and 551 ft). The resulting images along these profiles suggest resistivity values in the range of 100–2000 ohm m and show approximately subhorizontal and layered resistivity from near the surface down to about 35 m (115 ft). The water table is not directly observable but may be inferred from the change in resistivity values and correlation with the CPT data at approximately 13-m (43-ft) depth.

High resistivity values are generally seen between approximately 5- and 20+-m depth on each image. They belong to the vadose zone and the upper sand in the UAZ. Lower resistivity values are observed below 20-m (66-ft) depth, but this could be a response of the increased moisture content due to the saturated zone and/or variations of clay and sand contents within the study site. However, a significant nearly vertical anomaly, which propagates throughout all four recorded lines, is observed at about 125-m (410-ft) distance along the profiles. This anomaly propagates from near the surface to large depths and is characterized by rapid changes of several hundreds of thousands of ohm meters in the shallow data. This discontinuity is associated with low resistivity (high conductivity) and marks a sharp change in the subhorizontal resistivity values across it. Moreover, this discontinuity approximately corresponds with the projected position of the discontinuity imaged on the SSR data, making it a potential candidate for a steeply dipping inverse fault as interpreted before.

INTERPRETATION

Although a detailed stratigraphic layering was identified and interpreted in the upper approximately 50 m (164 ft) of the subsurface at the study site using various geophysical techniques, to constrain the TCE plume geometry and how it may relate to the structural geology of the subsurface, a direct correlation among the individual geophysical surveys was performed (Figure 15). In Figure 15, the crosshole GPR, electrical

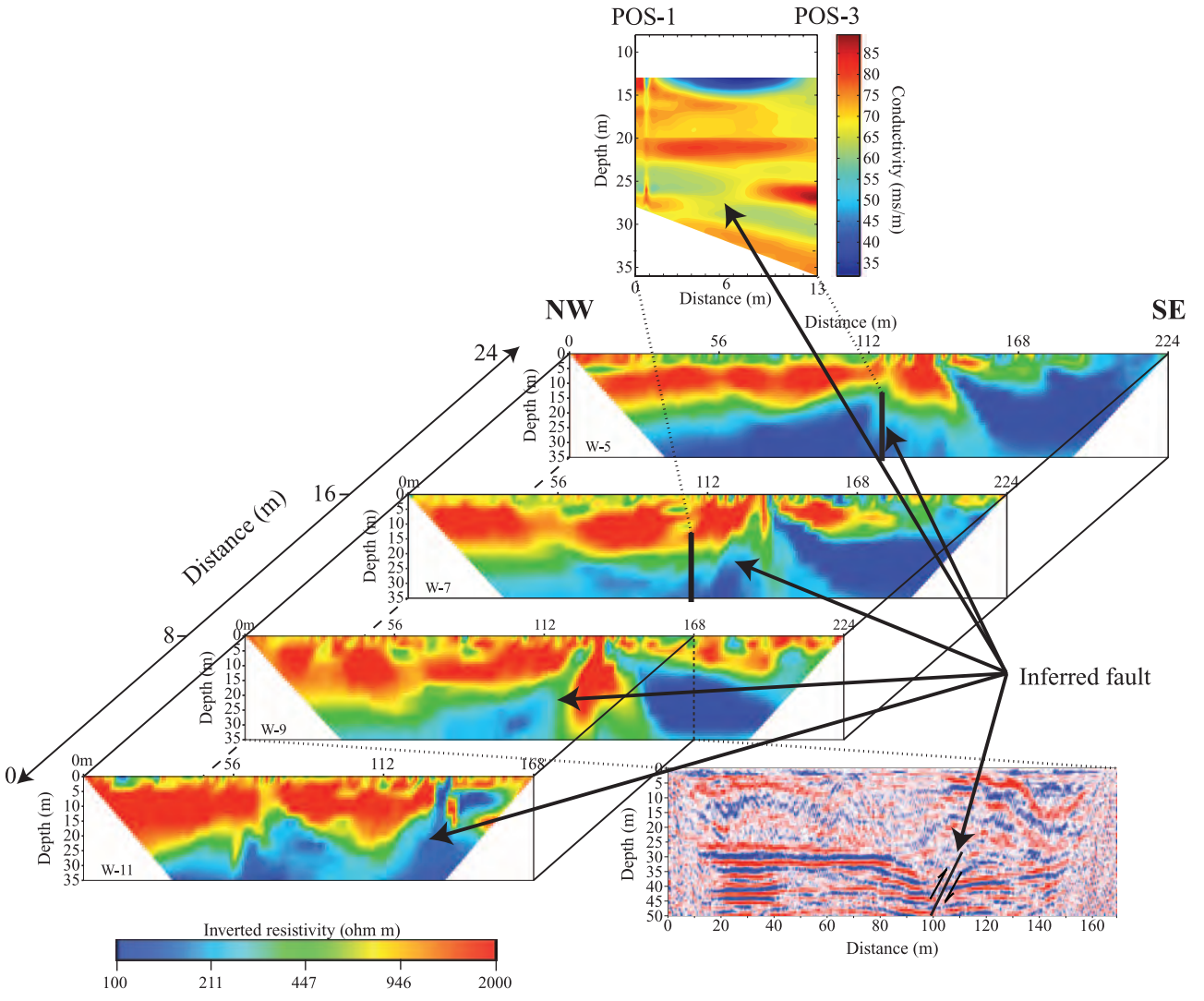

Figure 15. The 50-MHz crosshole radar EM wave conductivity tomogram (POS-1 and POS-3), electrical resistivity Wenner sections (W-5, -7, -9, and -11), and the upper 50 m (164 ft) of the 2-D SSR section correlation. Black arrows correspond to the interpreted inverse fault as described in the text.

resistivity, and seismic sections are shown at the same scale and are geographically aligned. As seen in this Figure 15, the position and orientation of the discontinuity interpreted on the seismic line seem to correlate well spatially with the discontinuity mapped on the resistivity profiles as well as the dipping feature in the crosshole radar tomograms, thus making it a strong candidate for a fault. Based on the seismic line, this inferred fault appears to have an inverse movement and is interpreted with a higher level of certainly below 23 m (75 ft) from the ground surface. Some of the geological and geophysical constraints of the interpreted inverse fault include the following: (1) the seismic image shows reverse movement, consistent with coastal plain faults (Higgins et al., 1978; Zoback et al., 1978; Behrendt et al., 1983; Hamilton et al., 1983; Schilt et al., 1983; Talwani, 1986; Shedlock and Harding, 1988; Snipes et al., 1993; Wyatt and Temples, 1996; Wyatt et al., 1996), (2) the interpreted position of the fault is consistent with the discontinuity mapped on the crosshole GPR tomograms between POS-1 and POS-3 as well as with the high-conductivity anomalies on the coincident resistivity profiles, and (3) the electrical resistivity changes greatly laterally across the high-conductivity anomaly. Although, based on the seismic profile, one can argue that the fault continues farther to the surface, however, the crosshole tomograms between POS-1 and POS-3 suggest that the interpreted fault stops at about 23-m (75-ft) depth. This interpretation makes the fault upper Eocene or older.

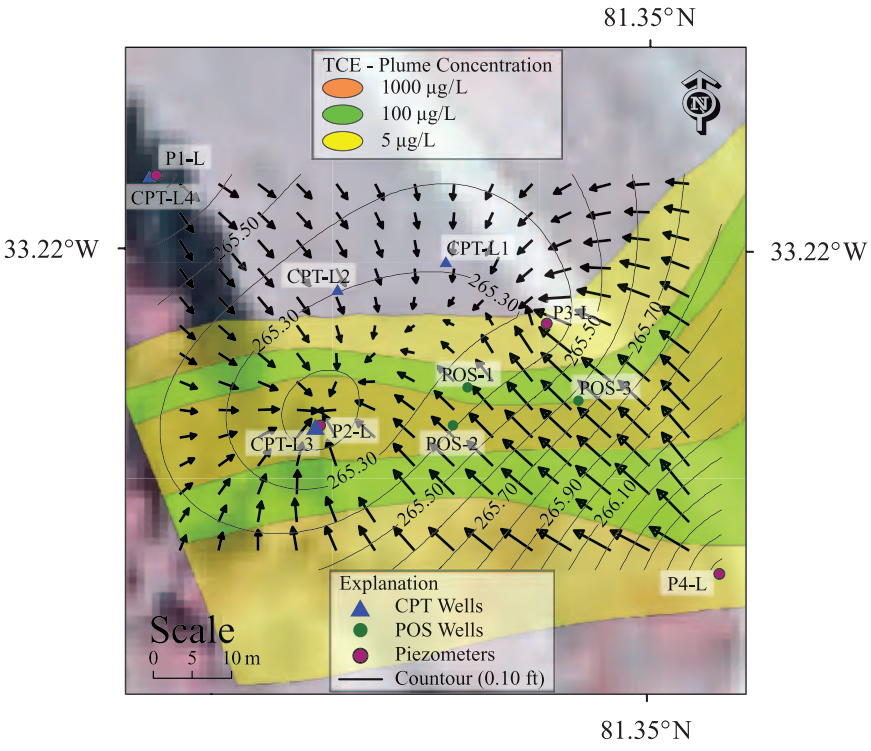

Figure 16. Potentiometric surface map with the hydraulic gradient changing across the study site. Note the convergence of groundwater flow near the area west of the position (POS) wells. CPT = cone penetrometer tests; TCE = trichloroethylene.

The three paleochannels imaged in the SSR section appear to have a control on the shape and migration direction of the TCE plume. Addison et al. (2009) indicated that the paleochannel complexes at the study site are acting as conduits for the plume migration, thus, the slight turn of the plume to the south-southwest near the POS wells. However, the hydraulic gradient calculated from potentiometric surface data between the piezometers (mapped in Figure 2) indicates a convergence of groundwater flow near the area west of the POS wells (Figure 16). This area of convergence appears to be within the paleochannel 2 imaged in the SSR section and by Addison et al. (2009). The groundwater flow, in a local spatial scale, could possibly have a preferred pathway trough paleochannel 2, hence, the plume narrowing down away from the source and flow updip stratigraphic bedding.

Interpretation and analysis of the surface GPR sections provide a detailed image of the overall internal structure and depositional patterns recorded within the sediments in the upper 16 m (52 ft) of a dynamic modern channel system (reflector packages A and B in Figures 8–11). From the surface GPR data, we can compare and correlate the channels with those in the SSR section and in Addison et al. (2009) to develop a relative explanation of the depositional processes that control the channel growth and modification with respect to the fault. Close observation of the surface GPR and SSR sections shows that the vertical offsets in the seismic data occur beneath the interpreted paleochannels. This fault may be the cause of the paleochannel growth, modification, and shape due to inverse faulting in the earliest stages of the paleochannels formation, which could have provided control on the structural evolution of the channels.

Based on a synthesis of all of the geophysical methods used in this study, an interpretive geologic model was generated and shown in Figure 17. Interpreted offsets of about 5 m (16 ft) across the inferred inverse fault are consistent with published literature that indicates faulting in the coastal plain sediments to be post Late Cretaceous. These faults generally exhibit the following features: (1) offsets of about 5 m (16 ft) close to the surface, (2) strike orientation in the northeastern–southwestern quadrant with reverse movement, and (3) movement beginning in the Cretaceous and decreasing with time (Cumbest et al., 1998, 2000). Based on the fault location and sense of movement, these faults can possibly be related to a series of other inverse faults in the region (i.e., Pen Branch, Crackerneck, Atta, Tinker Creek, Steel Creek, and Martin faults) associated with the formation of the Dunbarton Basin. Some of these faults were traced from within the crystalline basement upward into the UACP sediments inferring

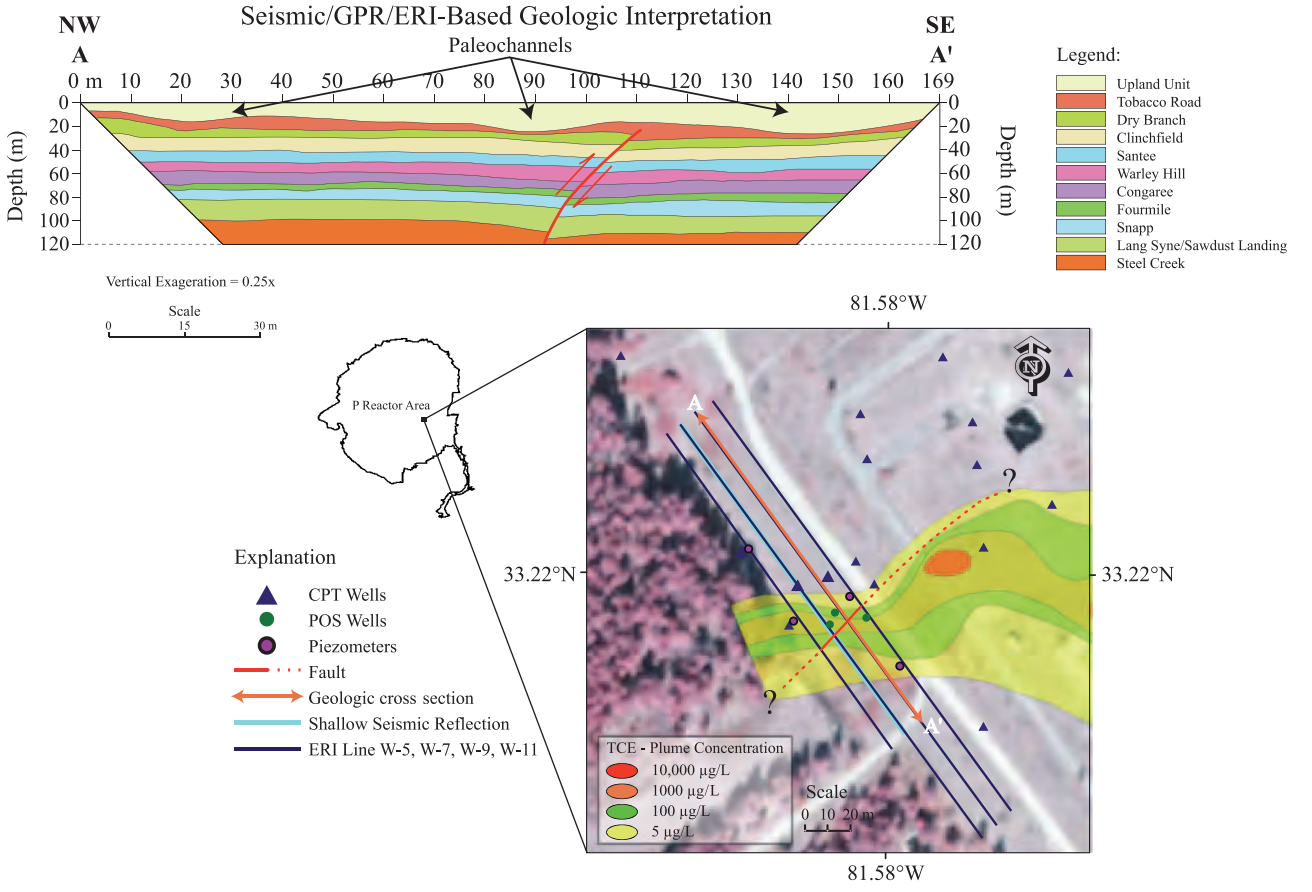

Figure 17. Interpreted geologic model from combined crosshole ground-penetrating radar, shallow seismic reflection, and electrical resistivity imaging (ERI) images. The location and extension of the interpreted inverse fault were traced in red line by correlating all these data sets. Layering discontinuity along the profile suggests horizon displacement of about 5 m (16 ft). CPT = cone penetrometer tests; POS = position; TCE = trichloroethylene.

reactivation of the older Paleozoic–Mesozoic structures during the Cretaceous and Tertiary (Snipes et al., 1993).

The paleochannel complexes are shown in Figure 17, with a series of three potentially distinct channels. Also shown in Figure 17 is the surface projection of the fault plane (red line in the lower right inset). Based on the relative positions of the contaminant plume and the interpreted fault, one can notice a fairly sharp termination of the northern edge of the plume against the fault. However, the behavior of a contaminant plume depends mostly on the type of hydrogeological profile through which it is moving. Indeed, this could also explain why the plume narrows away from the source instead of an expected broadening. The length and width of the plume can be affected by the groundwater flow and velocity and the aquifer's hydraulic conductivity. Contaminant plumes are more elongated in groundwater with high velocity than in groundwater with low velocity (Liu and Liptak, 1999; Fetter, 2001). Moreover, a higher hydraulic conductivity can result in more rapid movement and a longer and narrower plume (Palmer, 1992). Geological structures such as faults and/or channels can affect the rate and direction of a migrating plume. Thus, the interpreted inverse fault can act as a barrier or a conduit to the TCE plume depending on the lithology against the walls of the fault. The interbeded clay lenses in the permeable sand facies (i.e., upper, middle, and lower sand) within the P Reactor area can be splitting or retarding the sinking of the TCE plume and changing its shape course through time. Considering the results reported by Addison et al. (2009) and based on this interpretation, the migration of the plume appears likely to be constrained by (1) the presence of paleochannels in the subsurface (constraints on the plume migration direction), (2) the interpreted inverse fault (constraints on the structural evolution of the paleochannels), and (3) the local groundwater flow (constraint on the plume's longer and narrower shape away from the P Reactor and updip flow).

CONCLUSIONS

Three geophysical techniques were used to image and characterize the lateral and shallow geology at the P Reactor area, SSR, South Carolina. During subsurface characterization efforts, combining a variety of geophysical methods was necessary to improve our understanding on the shallow stratigraphy and structural geology at different resolution scales where the TCE plume seems to migrate across the regional stratigraphic dip and narrow away to the west from the source. The results of this study suggest that (1) the CPT and natural gamma logs correlate well with the SSR, GPR, and ERI data sets; (2) the surface radar data show the presence of modern channels in the uppermost part of the sections; (3) the crosshole radar data provided useful information down to about 36-m (118-ft) depth between the POS-1 and POS-2 wells; (4) the SSR data imaged a subvertical discontinuity with vertical offsets of approximately 5 m (16 ft); (5) the conductivity tomogram between the POS-1 and POS-3 wells shows a dipping near-vertical discontinuity at approximately 23-m (75-ft) depth; and (6) the ERI images show a low-resistivity discontinuity that correlates well with the discontinuity imaged on the SSR and crosshole GPR data. This discontinuity is consistent with the interpretation of a shallow inverse fault. The combination of all different geophysical techniques in this study suggests that the shallow (~23 m [75 ft] from the ground surface) inverse fault within the unconsolidated sediments (upper Eocene and older) appears to contribute to the plume's geometry and shape.

A series of paleochannel structures within the upper 30+ m (98+ ft) were interpreted on the SSR section, and they are also constrained by 3-D seismic data collected at the site (Addison et al., 2009). Interpretation and analysis of the SSR and surface GPR sections provide a detailed image of the overall internal structure and depositional patterns recorded within the sediments in the upper 16 m (52 ft) of a dynamic modern channel system. The hydraulic gradient calculated from potentiometric surface data between the piezometers indicates a convergence of groundwater flow near the area west of the POS wells.

How close to the surface the fault is is still uncertain; however, based on the SSR, crosshole GPR, and ERI data, it can be as shallow as approximately 23 m (75 ft) below ground surface. We believe that the geometry of the TCE plume is constrained by (1) the paleochannel system with respect to its migration direction, also suggested by Addison et al. (2009); (2) the presence of the inferred inverse fault that may contribute to the paleochannel growth and geometry; and (3) the local groundwater flow volume and direction updip stratigraphic bedding.

REFERENCES CITED

Aadland, R. K., J. A. Gellici, and P. A. Thayer, 1995, Hydrogeologic framework of west-central South Carolina: South Carolina Department of Natural Resources, Water Resource Division Report 5, 200 p.

Addison, A. D., M. G. Waddell, C. C. Knapp, D. T. Brantley, and J. M. Shafer, 2009, Developing a robust geologic conceptual model using pseudo 3-D P-wave seismic reflection data: Environmental Geosciences, v. 16, p. 1–16, doi:10.1306/eg.08110808003.

Annan, A. P., and J. L. Davis, 1992, Design and development of a digital ground penetrating radar system, *in* J. Pilon, ed., Ground penetrating radar: Geological Survey of Canada Paper 90-4, p. 49–55.

Aucott, W. R., 1996, Hydrology of the southeastern coastal plain aquifer system in South Carolina and parts of Georgia and North Carolina: U.S. Geological Survey Professional Paper 1410-E, 83 p.

Baker, G. S., D. W. Steeples, C. Schmeissner, M. Pavlovic, and R. Plumb, 2001, Near-surface imaging using coincident seismic and GPR data: Geophysical Research Letters, v. 28, p. 627–630, doi:10.1029/2000GL008538.

Behrendt, J. C., R. M. Hamilton, H. D. Ackermam, V. J. Henry, and K. C. Bayer, 1983, Marine multi-channel seismic evidence for Cenozoic faulting and deep crustal structure near Charleston, South Carolina, *in* G. S. Gohn, ed., Studies related to the Charleston, South Carolina earthquake of 1886—Tectonics and seismicity: U.S. Geological Survey Professional Paper 1313, p. J1–J29.

Cederstrom, D. J., E. H. Boswell, and G. R. Tarver, 1979, Summary of appraisals of the Nation's ground-water resources—South Atlantic-Gulf Region: U.S. Geological Survey Professional Paper 813-O, 35 p.

Chapman, W. L., and M. P. Di Stefano, 1989, Savannah River plant seismic survey, 1987–88: Conoco Inc. Seismic Acquisition Section, Research Report 1809-005-006-1-89, 110 p.

Clement, W. P., W. Barrash, and M. D. Knoll, 2006, Reflectivity modeling of a ground-penetrating radar profile of a saturated fluvial formation: Geophysics, v. 71, p. K59–K66, doi:10.1190/1.2194528.

Colquhoun, D. J., and M. G. Muthig, 1991, Stratigraphy and structure of the Paleocene and lower Eocene Black Mingo Group, South Carolina, *in* W. Horton Jr. and V. A. Zullo, eds., The geology of the Carolinas: Carolina Geological Society 50th Anniversary Volume: Knoxville, Tennessee, The University of Tennessee Press, p. 241–250.

Cumbest, R. J., D. E. Stephenson, D. E. Wyatt, and M. Maryak, 1998, Basement surface faulting for Savannah River site and vicinity: Westinghouse Savannah River Company, Technical Report, WSRC-TR-98-00346, 48 p.: http://www.osti.gov/bridge/servlets/purl/762016-yxu8iD/webviewable (accessed December 17, 1998).

Cumbest, R. J., D. E. Wyatt, D. E. Stephenson, and M. Maryak, 2000, Comparison of Cenozoic faulting at the Savannah River site to fault characteristics of the Atlantic Coast Fault Province: Implications for fault capability, Westinghouse Savannah River Company, Technical Report, WSRC-TR-2000-00310, 24 p.:

http://sti.srs.gov/fulltext/tr2000310/tr2000310.html (accessed November 14, 2000).
Fallaw, W. C., and V. Price, 1992, Outline of stratigraphy at the Savannah River site, *in* W. C. Fallaw and V. Price, eds., Geological investigations of the central Savannah River area, South Carolina and Georgia: Carolina Geological Society, 1992 Annual Field Trip Guidebook, U.S. Department of Energy and SC Carolina Geological Survey, p. 17–40: http://sti.srs.gov/fulltext/ms2000606/ms2000606.pdf (accessed November 15, 2000).
Fallaw, W. C., and V. Price, 1995, Stratigraphy of the Savannah River site and vicinity: Southeastern Geology, v. 35, p. 21–58.
Fallaw, W. C., V. Price, and P. A. Thayer, 1990, Stratigraphy of the Savannah River site, South Carolina, *in* V. A. Zullo, W. Burleigh Harris, and V. Price, eds., Savannah River region: Transition between the Gulf and Atlantic coastal plains: Proceedings of the 2nd Bald Head Island Conference on Coastal Plains Geology, Wilmington, North Carolina, The University of North Carolina at Wilmington, p. 29–36.
Fetter, C. W., 2001, Applied hydrogeology: New Jersey, Upper Saddle River, 598 p.
Gross, R., A. G. Green, H. Horstmeyer, and J. H. Begg, 2004, Location and geometry of the Wellington fault (New Zealand) defined by detailed three-dimensional georadar data: Journal of Geophysical Research, v. 109, p. B05401, doi:10.1029/2003JB002615.
Hamilton, R. M., J. C. Behrendt, and H. D. Ackermam, 1983, Land multi-channel seismicreflection evidence for tectonic features near Charleston, South Carolina, *in* G. S. Gohn, ed., Studies related to the Charleston, South Carolina earthquake of 1886—Tectonics and seismicity: U.S. Geological Survey Professional Paper 1313, p. I1–I18.
Higgins, B. B., G. S. Gohn, and L. M. Bybell, 1978, Subsurface geologic evidence for normal faults in the South Carolina coastal plain near Charleston: Geological Society of America Abstract with Programs, v. 10, 171 p.
Liu, D., and B. G. Liptak, 1999, Groundwater and surface water pollution: Chelsea, Michigan, Lewis Publishers, 160 p.
Lunne, T., P. K. Robertson, and J. J. M. Powell, 1997, Cone penetration testing in geotechnical practice: London, Blackie Academic and Professional, 312 p.
Marine, I. W., 1974, Geohydrology of buried Triassic basin at Savannah River plant, South Carolina: AAPG Bulletin, v. 58, p. 1825–1837.
Millings, M., K. Vangelas, and M. Harris, 2003, Source term determination for P-area reactor ground-water operable unit: Westinghouse Savannah River Company, Savannah River Site, Westinghouse Savannah River Company-TR-2003-00142, 1 p.
Mota, R., and F. Monteiro dos Santos, 2006, 2-D sections of porosity and water saturation percent from combined resistivity and seismic surveys for hydrogeologic studies: The Leading Edge, v. 25, p. 735–737, doi:10.1190/1.2210058.
Neal, A., 2004, Ground-penetrating radar and its use in sedimentology: Principles, problems and progress: Earth-Science Reviews, v. 66, p. 261–330, doi:10.1016/j.earscirev.2004.01.004.
Nystrom Jr., P. G., R. H. Willoughby, and L. K. Price, 1991, Cretaceous and Tertiary stratigraphy of the upper coastal plain, South Carolina, *in* W. Horton Jr. and V. A. Zullo, eds., The geology of the Carolinas: Carolina Geological Society 50th Anniversary Volume: Knoxville, Tennessee, The University of Tennessee Press, p. 221–240.
Paillet, F. L., and K. J. Ellefsen, 2005, Downhole applications of geophysics, *in* D. K. Butler, ed., Near-surface geophysics: Part 1: Tulsa, Oklahoma, Society of Exploration Geophysicists, p. 439–471.
Palmer, C. M., 1992, Principles of contaminant hydrogeology: Chelsea, Michigan, Lewis Publishers, 256 p.
Peterson, J. E., 2001, Pre-inversion corrections and analysis of radar tomographic data: Journal of Environmental and Engineering Geophysics, v. 6, p. 1–18, doi:10.4133/JEEG6.1.1.
Pipan, M., E. Forte, G. Dal Moro, M. Sugan, and I. Finetti, 2003, Multifold ground-penetrating radar and resistivity to study the stratigraphy of shallow unconsolidated sediments: The Leading Edge, v. 22, p. 876–878, doi:10.1190/1.1614161.
Sangree, J. B., and J. M. Widmier, 1979, Interpretation of depositional facies from seismic data: Geophysics, v. 44, p. 131–160, doi:10.1190/1.1440957.
Schilt, S. F., L. D. Brown, J. E. Oliver, and S. Kaufman, 1983, Subsurface structure near Charleston, South Carolina—Results of Consortium for Continental Reflection Profiling (COCORP) reflection profiling in the Atlantic coastal plain, *in* G. S. Gohn, ed., Studies related to the Charleston, South Carolina earthquake of 1886—Tectonics and seismicity: U.S. Geological Survey Professional Paper 1313, p. H1–H19.
Shedlock, K. M., and S. T. Harding, 1988, Structure of the shallow crust near Charleston, South Carolina: Geological Society of America Abstract with Programs, v. 20, 313 p.
Siple, G. E., 1967, Geology and groundwater of the Savannah River plant and vicinity, South Carolina: U.S. Geological Survey, Water-Supply Paper 1841, 113 p.
Snipes, D. S., W. C. Fallaw, V. Price, and R. J. Cumbest, 1993, The Pen Branch fault: Documentation of Late Cretaceous–Tertiary faulting in the coastal plain of South Carolina: Southeast Geology, v. 33, p. 195–218.
Sohl, N. F., and J. P. Owens, 1991, Cretaceous stratigraphy of the Carolina coastal plain, *in* W. Horton Jr. and V. A. Zullo, eds., The geology of the Carolinas: Carolina Geological Society 50th Anniversary Volume: Knoxville, Tennessee, The University of Tennessee Press, p. 191–220.
Talwani, P., 1986, Current thoughts on the cause of the Charleston, South Carolina earthquakes: South Carolina Geology, v. 29, p. 19–38.
Ward, S. H., 1990, Resistivity and induced polarization methods, *in* S. H. Ward, ed., Geotechnical and environmental geophysics: Tulsa, Oklahoma, Society of Exploration Geophysicists, p. 147–189.
Wempe, W., and G. Mavko, 2006, A new method for constraining total porosity: The new total porosity-electrical resistivity upper bound: The Leading Edge, v. 25, p. 714–719, doi:10.1190/1.2210054.
Wyatt, D. E., and T. J. Temples, 1996, Ground-penetrating radar detection of small-scale channels, joints and faults in the unconsolidated sediments of the Atlantic coastal plain: Environmental Geology, v. 27, p. 219–225, doi:10.1007/BF00770435.
Wyatt, D. E., M. G. Waddell, and G. B. Sexton, 1996, Geophysics and shallow faults in unconsolidated sediments: Ground Water, v. 34, p. 326–334, doi:10.1111/j.1745-6584.1996.tb01892.x.
Wyatt, D. E., R. K. Aadland, and F. H. Syms, 2000, Overview of the Savannah River site stratigraphy, hydrostratigraphy and structure, *in* D. E. Wyatt and M. K. Harris, eds., Savannah River site environmental remediation system in unconsolidated upper coastal-plain sediments, stratigraphic and structural considerations: Carolina Geological Society, 2000 Annual Field Trip Guidebook, WSRC-MS-2000-00606, p. A14–A48: http://carolinageologicalsociety.org (accessed November 15, 2000).
Yilmaz, Ö., 1987, Seismic data processing: Investigations in geophysics, 2d ed.: Tulsa, Oklahoma, Society Exploration Geophysics, 69 p.
Yilmaz, Ö., 2001, Seismic data analysis: Tulsa, Oklahoma, Society Exploration Geophysics, 2027 p.
Zoback, M. D., J. H. Healy, J. C. Roller, G. S. Gohn, and B. B. Higgins, 1978, Normal faulting and in situ stress in the South Carolina coastal plain near Charleston: Geology, v. 6, p. 147–152, doi:10.1130/0091-7613(1978)6<147:NFAISS>2.0.CO;2.

SECTION 2

HYDROGEOPHYSICAL DATA INTEGRATION

Publication 3: Kowalsky, M.B., S. Finsterle, E. Gasperikova, G. Moridis, and S.S. Hubbard, 2009, Hydrogeophysical approaches with the TOUGH family of codes, TOUGH Symposium 2009, LBNL, Berkeley, CA, 1-8.

HYDROGEOPHYSICAL APPROACHES WITH THE TOUGH FAMILY OF CODES

M. B. Kowalsky, S. Finsterle, E. Gasperikova, G. Moridis, and S. S. Hubbard

Lawrence Berkeley National Laboratory
1 Cyclotron Road
Berkeley, CA, 94705, U.S.A
e-mail: mbkowalsky@lbl.gov

ABSTRACT

We describe three hydrogeophysical approaches for improving characterization of subsurface flow and transport by integrated simulation of geophysical and hydrogeochemical processes and measurements. Each approach is presented with an example that benefits from recent advances in the TOUGH family of codes. The first example considers the coupled simulation of time-lapse electrical resistivity data (ERT) and hydrogeochemical data to evaluate the impact of recharge on subsurface contamination at the DOE Oak Ridge Integrated Field Challenge site. The second example involves the combination of multiscale hydrogeophysical data integration and dual-domain transport modeling to enable long-term transport prediction at a contaminated site within the DOE Savannah River Site. The third example, based on a site in the Gulf of Mexico, demonstrates how the coupled simulation of gas production and time-lapse seismic surveys can help monitor the evolution of subsurface properties, and thus manage production from a gas hydrate accumulation. While the approaches considered in these examples are entirely different from one another, they share the common goal of improving subsurface characterization by taking advantage of the sensitivity of geophysical data to subsurface fluid distributions and properties that govern flow and transport. This work reflects the substantial progress made in developing approaches for integrating geophysical and hydrogeochemical data in the TOUGH family of codes, in applications ranging from environmental remediation to nuclear waste storage to oil and gas production.

INTRODUCTION

The use of geophysical data for hydrological investigations—broadly referred to as the field of hydrogeophysics—is increasingly popular, due to the sensitivity of geophysical measurements to properties that are (directly or indirectly) related to hydrological processes. The challenge is in extracting information from geophysical data at a relevant scale that can be used quantitatively to inform hydrological models.

A powerful recently developed hydrogeophysical approach involves the coupled modeling of hydrological and geophysical processes, such that simulated geophysical measurements become a function of the hydrological processes. This modeling approach, sometimes referred to as coupled hydrogeophysical modeling, can be used in "inverse mode," wherein hydrological parameters are estimated by minimizing the difference between measured and simulated geophysical and hydrological data using an optimization algorithm. Coupled hydrogeophysical modeling is also useful in "forward mode," for example, to evaluate the sensitivity of different geophysical measurements for monitoring purposes or experimental design.

The TOUGH family of codes has been used for a variety of coupled hydrogeophysical modeling applications. For example, an approach involving time-lapse ground-penetrating radar measurements (Kowalsky et al., 2004; Finsterle and Kowalsky, 2008) was applied to an infiltration experiment at the DOE Hanford site (Kowalsky et al., 2005) and to a drift-scale experiment at the proposed site for nuclear waste disposal at Yucca Mountain (Kowalsky et al., 2008). The use of electrical resistance tomography (ERT) data was also considered (Lehikoinen et al., 2009a; 2009b). Such approaches are applicable when physical properties in the system (e.g., aqueous- or gas-phase saturation, solute concentration, pressure, temperature) are undergoing transient changes, and time-lapse geophysical measurements are available that are sensitive to such changes. These were also local-scale studies, limited to relatively small regions in the vicinity of boreholes.

For studies involving much larger scales, such as the plume scale, time-lapse geophysical data are not always applicable or available for aquifer characterization, and different techniques are needed for integrating hydrogeophysical measurements. While it is impractical to collect high-resolution characterization data over the entire aquifer, various types of hydrogeophysical data are commonly collected that cover a range of scales: from regional-scale surface geophysical data, to local-scale crosshole geophysical data, to well logging and core data. Such data may be accommodated using a multiscale hydrogeophysical data integration framework (Kowalsky et al., 2007) to provide useful information that can be integrated directly into a hydrological model.

Here we describe three examples of recent studies involving the TOUGH family of codes that reflect a

variety of hydrogeophysical approaches: coupled hydrogeophysical modeling of time-lapse electrical resistivity data and hydrogeochemical data to evaluate the impact of recharge on subsurface contamination at the DOE Oak Ridge Integrated Field Challenge site (Example 1); combined multiscale hydrogeophysical data integration and dual-domain transport modeling to enable long-term transport prediction at a contaminated site at the DOE Savannah River Site (Example 2); and examining the feasibility of seismic methods for monitoring a gas hydrate accumulation undergoing production (Example 3).

EXAMPLE 1: COUPLED MODELING OF ELECTRICAL RESISTIVITY DATA AND HYDROGEOCHEMICAL DATA

Here we describe an approach that will be used to help understand the impact of recharge on subsurface contamination at the southern-most corner of the S-3 ponds at the Oak Ridge Integrated Field Research Challenge (IFRC) site in eastern Tennessee. The approach involves the coupled modeling of time-lapse electrical resistivity (ERT) voltage data and hydrogeochemical data, including water level and solute concentration data. Details of the work may be found in Kowalsky et al. (2009a).

At the study site, recharge to groundwater is substantial and highly variable, exerting a major influence on local hydrological processes. Recharge from precipitation fluctuates not only seasonally and annually, but also varies rapidly in response to individual storm events. A related source of recharge—runoff from the S-3 parking lot—enters the formation through intermittent standing water in a drainage ditch. The formation of perched water zones is commonly observed at shallow depths, also affecting local recharge. Heterogeneity at the S-3 site—resulting from a complex mixture of soil, saprolite, and fractured sedimentary rocks—along with preferential flow paths, and a rapid aquifer response to fluctuations in recharge, all lead to spatial and temporal variability of groundwater chemistry and contaminant transport (Van de Hoven, 2005), necessitating the development of new approaches to interpret data and understand hydrological processes at the site.

We developed a coupled hydrogeophysical modeling approach for the site using iTOUGH2 (Finsterle, 2004), which provides forward and inverse modeling capabilities for a variety of hydrogeochemical and geophysical data. The approach integrates a hydrogeochemical forward model (HM) and a geophysical forward model (GM). The HM is TOUGH2 (Pruess et al., 1999), which simulates fluid flow and solute transport, and the corresponding hydrogeochemical measurements. The GM is an electrical resistivity model called CRMOD (Kemna et al., 2002), which simulates electrical current in the subsurface and the corresponding resistivity measurements.

The coupled hydrogeophysical modeling approach (Figure 1) can be used to perform inverse modeling, as follows: (1) a set of hydrogeochemical and geophysical parameters is specified; (2) a hydrogeochemical simulation is performed with the HM, producing the simulated hydrogeochemical data and the information used as input for the GM; (3) a petrophysical model translates the HM output (e.g., water saturation, solute concentration, and porosity) into the relevant geophysical property (e.g., electrical resistivity); (4) the geophysical data are simulated with the GM at the specified geophysical survey times; (5) an objective function is evaluated to measure the dissimilarity between the measured and simulated hydrogeochemical and geophysical data; (6) a new set of hydrological and geophysical parameters are obtained through an optimization algorithm (or a nongradient-based optimization algorithm); and (7) the process is repeated starting at (2), until a set of parameters that sufficiently minimizes the objective function is found, at which point the inversion is complete.

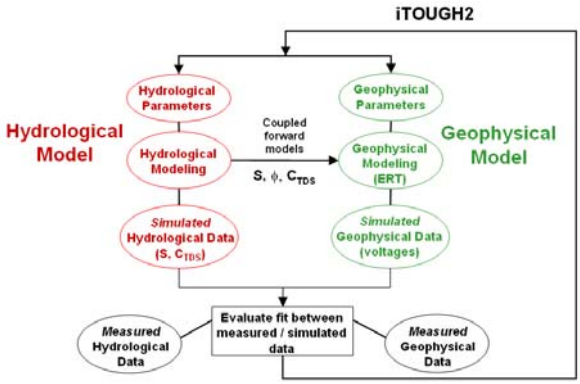

Figure 1. Approach for coupled hydrogeophysical inverse modeling.

For this study, we constructed a local-scale hydrogeochemical model based on field data collected near the S-3 ponds site at Oak Ridge in late 2008 during high precipitation and recharge events. Time-varying infiltration due to rainfall and a drainage ditch drives the system and is implemented based on measured data. As a first step, we consider at present a vertical 1D model (Figure 2); its use makes the implicit assumption that lateral flow is less significant than vertical flow (this assumption will be relaxed in future work). An atmospheric boundary is at the top surface of the model, and a semi-confining layer is at the bottom.

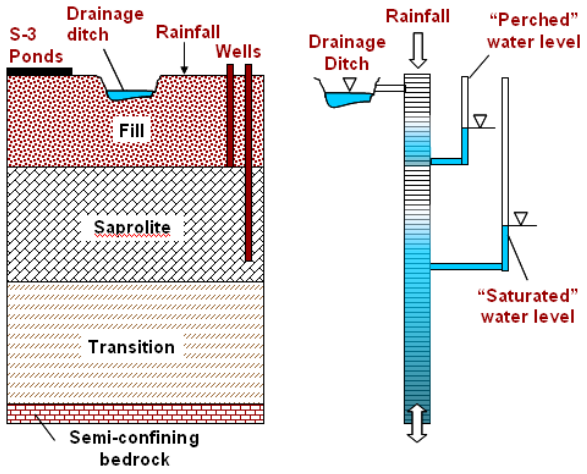

Figure 2. Conceptual model (left), and schematic of 1-D hydrological model (right).

The model is calibrated to water level data measured in wells within the saturated zone and a zone with an intermittently perched water table, and to nitrate concentration data collected from a multilevel sampling well. In Figure 3, preliminarily simulated hydrogeochemical data are compared with measured data.

The 1D hydrogeochemical model described above is coupled to a 2D electrical resistivity model. That is, output from the vertical 1D hydrological grid is projected onto the 2D ERT grid (Figure 4), giving an ERT model with time-varying vertical heterogeneity.

In this study, we consider a subset of the ERT electrode configurations used in the field experiment. The chosen subset is sensitive to vertical variations in properties and time-varying changes thereof, and thus is well suited to the hydrological model. In particular, the subset of measurements includes current dipoles formed with electrodes in opposing boreholes, and potential dipoles formed by receivers in individual boreholes (and only the electrodes that stay below the fluctuating water table are considered). One of the current dipoles and its corresponding measurement dipoles are depicted in Figure 4.

The ERT voltages simulated at four survey times for all current and measurement dipole combinations considered in this study are shown in Figure 5. Note that changes from the first to the second survey are minor, but significant changes from the first to the third and fourth surveys are substantial, indicating good sensitivity of ERT data to the hydrogeochemical processes. In ongoing work, we are performing the coupled hydrogeophysical inversion of these data sets (Figure 3 and 5).

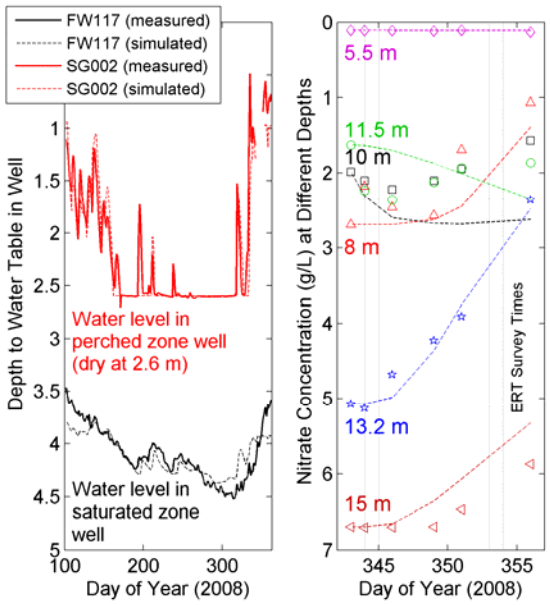

Figure 3. Measured and simulated (left) water level data in the perched and saturated zone wells, and (right) nitrate concentrations at noted depths in a multilevel sampling well. Depths less than 2.6 m indicate the presence of water in the perched zone well.

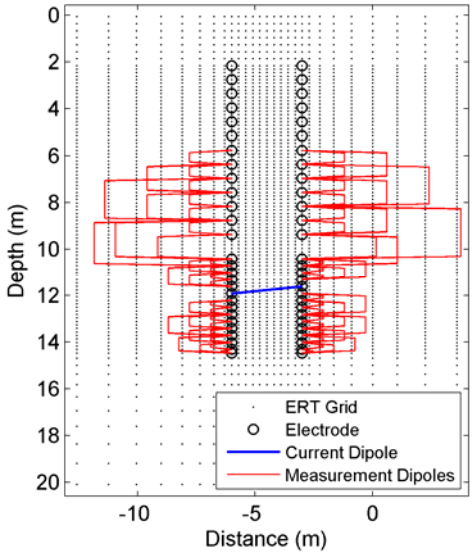

Figure 4. Numerical grid for ERT showing the electrodes for a current dipole (blue line) and the corresponding 67 measurement dipoles (red lines). An additional 20 current dipoles at different depths are also included, each with a different set of measurement dipoles, giving 1,442 measurements per survey. We consider four surveys in all from December 2008.

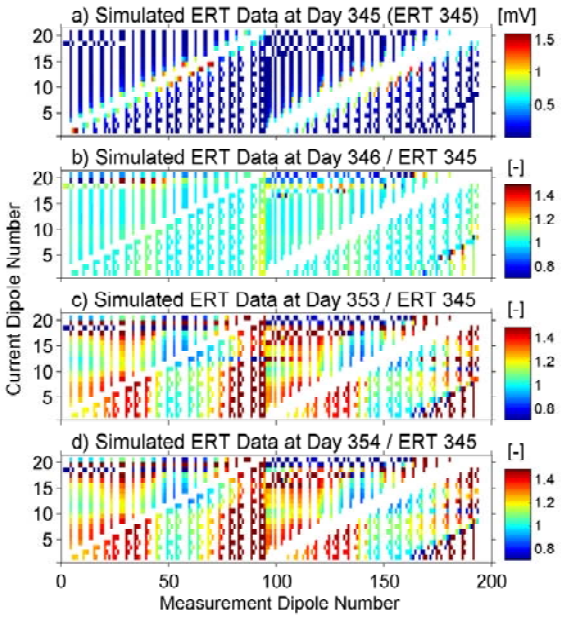

Figure 5. Simulated ERT data as a function of measurement dipole (x-axis) and current dipole (y-axis) for four survey times. Voltages are shown in (a) for the first survey time (Day 343), while voltages for later survey times (Days 344, 353, 354), in (b)–(d), respectively, are normalized by values of the first survey time.

The overall goals in this study are to evaluate the sensitivity of the approach for discerning the hydrogeochemical processes of interest and to evaluate the sensitivity of the electrical resistivity datasets for monitoring freshwater recharge and associated contaminant dilution effects. The insight gained is expected to help guide site-wide efforts examining the influence of recharge on contaminant concentrations and natural attenuation mechanisms. Future work will involve the incorporation of increasingly complex processes (e.g., fracture-matrix interactions), additional hydrogeochemical data types (e.g., isotopic data), and additional geophysical data types (e.g., surface-based ERT, self potential or SP, and surface seismic) into the modeling framework.

EXAMPLE 2: COMBINED HYDROGEOPHYSICAL DATA INTEGRATION AND DUAL-DOMAIN TRANSPORT MODELING

Predicting the long-term behavior of contaminant plumes using conventional characterization and modeling approaches is not reliably accurate for guiding environmental remediation strategies. The deficiency evidently results from an inability to collect high-resolution characterization data over the plume scale, and from the computational burden of high-resolution plume-scale transport simulations. In this example, we discuss an approach that enables more reliable and computationally efficient contaminant transport prediction, through the combination of multiscale hydrogeophysical data integration and dual-domain transport modeling. Details of this work will be provided in a publication that is in preparation; an earlier version was presented by Kowalsky et al. (2007).

Because the approach is developed within the context of a contaminated site (the P-Area) at the DOE Savannah River Site, we assume the aquifer of interest is composed of two dominant facies: one mobile and one immobile (or less mobile). Contaminant interactions between the mobile and immobile facies are expected to play a key role in long-term behavior at the plume scale; such interactions can be accounted for using a dual-domain model (DDM), provided that the necessary parameters are obtainable from characterization data. Accordingly, the approach we developed combines (1) a DDM that relies on field-measurable attributes; and (2) a facies-based multiscale characterization procedure that incorporates different types of hydrological and geophysical data (e.g., seismic and electrical resistivity) collected at various scales (i.e., surface, crosshole, and core scale), as guided by parameterization needs of the DDM.

The progression of the approach is depicted in Figure 6, with the hydrogeophysical data as the first component. The surface-based geophysical data provide information over large regions but with relatively low resolution, while the crosshole data provide higher resolution information but at limited locations. The crosshole data may be useful for mapping the distribution of sand or clay facies, for example, between two wells; lower resolution surface data provide larger-scale (regional) information, such as the average proportion of sand or clay facies within a depositional unit throughout the aquifer. Core data provide point measurements that help to interpret crosshole geophysical data and link them to surface data.

Hydrogeophysical data integration is the second component of the approach (Figure 6). It is performed using a Bayesian statistical model, similar to that developed by Chen et al. (2004), in which the unknowns, cast as random variables, are framed as a joint conditional probability density function (pdf). By sampling the pdf, the regional-scale volume fraction is estimated throughout the aquifer, based on the surface-based geophysical data, while being conditioned to the core data and crosshole geophysical data at a smaller scale. Figure 7 depicts the various scales of data and the unknowns.

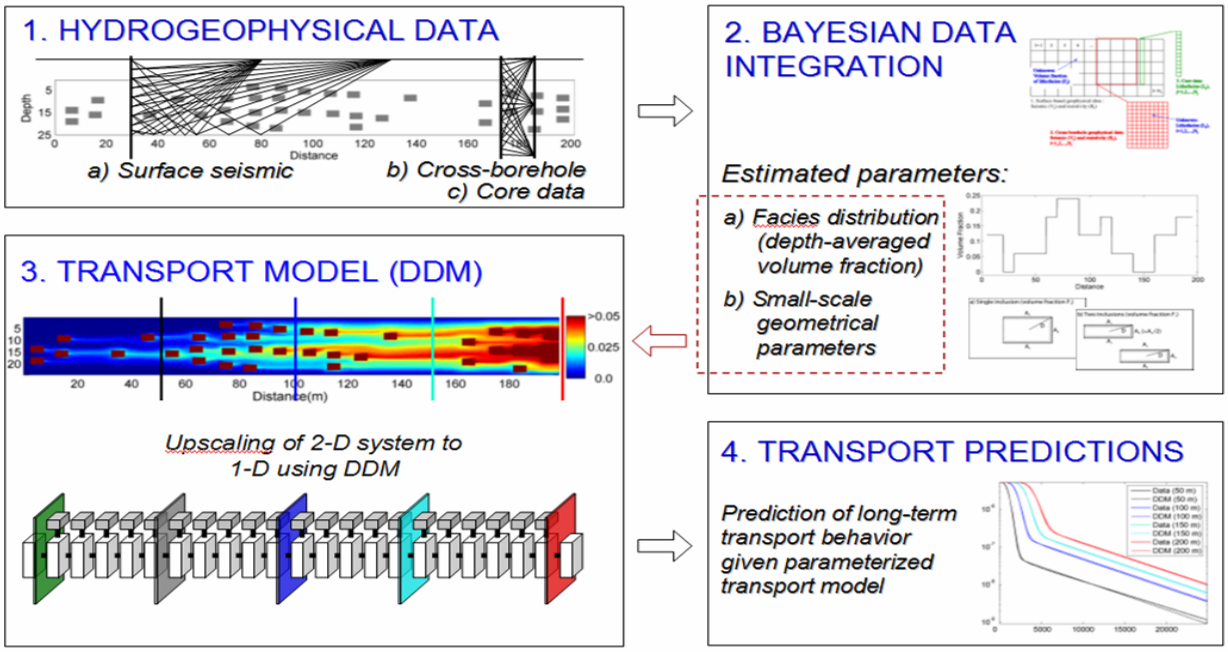

Figure 6. Approach for combined hydrogeophysical data integration and dual-domain transport modeling.

For the transport model (the third component of the approach, as depicted in Figure 6), we employ a 1D DDM with the assumption that it can adequately reproduce the transport behavior of a 2D aquifer containing low-permeability inclusions. Transport between the mobile domain (i.e., high-permeability regions) and the immobile domain (i.e., low-permeability regions) is explicitly accounted for using geometrical features inferred in the data integration approach. Specifically, the transport model requires characterization of the inclusion geometry, the spatially varying volume fraction of each facies, and a mass-transfer parameter.

The last step entails hydrological predictions, such as contaminant breakthrough curves at wells that are downgradient from the contaminant source, using the DDM parameterized with data from the hydrogeophysical data integration (fourth component in Figure 6),.

We performed a synthetic study to explore links between the geophysical data and the DDM parameters, and to test the overall feasibility of the approach. iTOUGH2 was used to (1) develop a high-resolution transport model for generating the "real" data, (2) develop the DDM and incorporate output from the hydrogeophysical data integration, and (3) make transport predictions. An example of the synthetic data is shown in Figure 8.

In summary, we have developed a linked data integration-transport modeling approach for long-term contaminant transport predictions and collected a variety of field-scale hydrogeophysical data at the P-Area to test the approach. We are using a simplified transport model that can be parameterized mechanistically with multiscale characterization data. Currently, the approach is being applied to prediction of trichloroethylene plume behavior at the P-Area at the Savannah River Site.

EXAMPLE 3: MONITORING GAS HYDRATE PRODUCTION WITH SEISMIC DATA

Many studies involving the application of geophysical methods in the field of gas hydrates have focused on determining rock-physics relationships for hydrate-bearing sediments, with the goal of using remote-sensing techniques to delineate boundaries of gas hydrate accumulations, and to estimate the quantities of gas hydrate within such accumulations. However, the potential for using time-lapse geophysical methods to monitor the evolution of hydrate accumulations during production has not been investigated. In this study, we begin to examine the feasibility of using time-lapse seismic methods, vertical seismic profiling (VSP) in particular, for monitoring changes in hydrate accumulations predicted to occur during production of natural gas. This is made possible through a numerical simulation tool we developed for the coupled simulation of (1) large-scale production in hydrate accumulations and (2) time-lapse geophysical surveys. While details of the study have been submitted for publication (Kowalsky et al., 2009b), a brief overview follows.

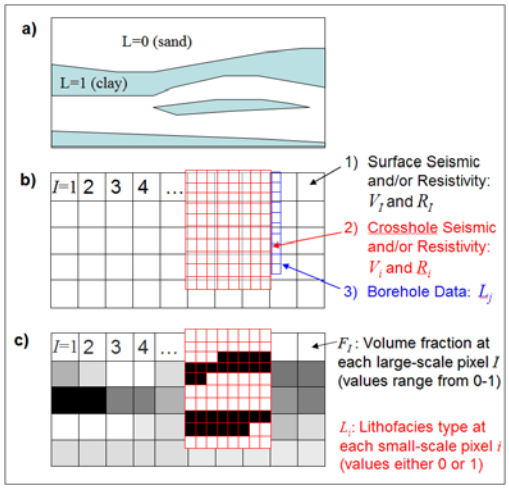

Figure 7. Depiction of data types and scales. Hydrogeophysical data: a) conceptual model, b) data sets at two scales (schematic), c) unknown parameters to be estimated.

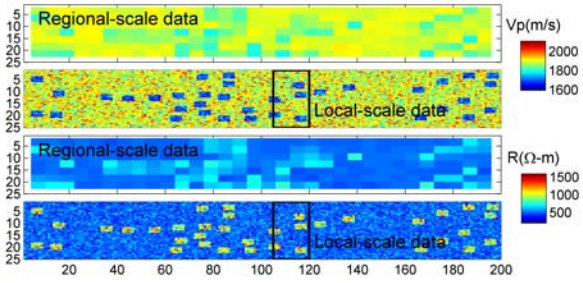

Figure 8. Example of synthetic hydrogeophysical data: regional-scale (surface-based) and local-scale (cross-borehole). The top subplots show seismic; the bottom show resistivity.

We consider a hydrate accumulation in the Gulf of Mexico that represents a promising target for production. The overall goals of the work are to examine the sensitivity of geophysical attributes and parameters to the changing conditions in hydrate accumulations, and to determine optimal sampling strategies (e.g., source frequency, time interval for data acquisition) and measurement configurations (e.g., source and receiver spacing for vertical seismic profiling), while taking into account uncertainties in rock-physics relationships. The study focuses on the use of seismic measurements, but the approach can easily be extended to consider additional geophysical data, such as electromagnetic measurements.

TOUGH+HYDRATE is the code used in this study for simulating gas production from a hydrate accumulation. This code, the successor to an earlier version called TOUGH-Fx/HYDRATE (Moridis et al., 2005), models the nonisothermal hydration reaction, phase behavior, and flow of fluids and heat under conditions typical of natural methane-hydrate deposits in complex geological formations. It includes both equilibrium and kinetic models of hydrate formation and dissociation, and can handle any combination of hydrate dissociation mechanisms, such as depressurization and thermal stimulation. It accounts for heat and up to four mass components (i.e., water, CH_4, hydrate, and water-soluble inhibitors such as salts or alcohols) that are partitioned among four possible phases (gas, liquid, ice or hydrate phases, existing individually or in any of 12 possible combinations).

To simulate seismic measurements within a TOUGH+HYDRATE production simulation, we implemented a code that numerically solves the wave equations for an isotropic linear viscoelastic medium in 2D using a time-domain staggered-grid finite difference formulation. The input for the seismic simulations includes bulk density, and the bulk and shear moduli. The bulk density is a function of the density of the aqueous, gas, and hydrate phases, calculated in TOUGH+HYDRATE as a function of pressure and temperature. The bulk and shear moduli are determined using a rock-physics model.

The numerical grids used for simulating production of natural gas from a hydrate-bearing layer (HBL), as well as the overlapping grid used to simulate the time-lapse seismic surveys, are shown in Figure 9. Seismic properties, calculated using output from the TOUGH+HYDRATE grid, are mapped onto the seismic grid by interpolation.

Evolution of the hydrate and gas saturation is depicted in Figure 10, revealing the occurrence of three moving dissociation fronts within the HBL: the first moving in the radial direction, confined to relatively small distances from the wellbore; the second descending at the upper boundary of the entire HBL; and the third ascending at the lower boundary of the entire HBL. As the HBL undergoes dissociation, hydrate saturation decreases, while gas and water saturation increase. The largest accumulation of gas occurs just above the top of the HBL, but gas is also seen to increase below and within the HBL. A description of the production model and comprehensive analysis of the system behavior are given in Moridis and Reagan (2007).

The changes in physical properties within the HBL described above may be detectable using geophysical monitoring techniques. Using the coupled production-seismic model described above, we simulate vertical seismic profile (VSP) surveys at various times during production. We achieve different angles of VSP measurements by modeling the source as an

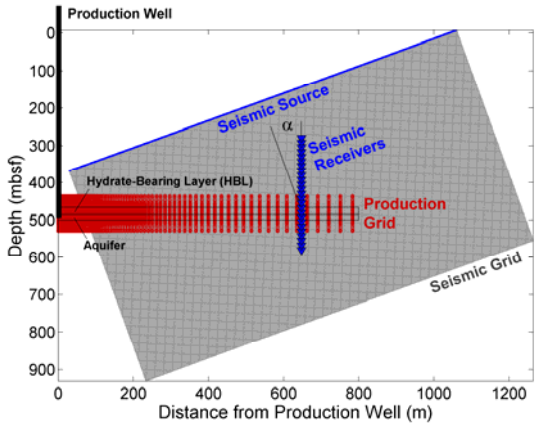

Figure 9. Numerical grids for simulating production of natural gas from a hydrate-bearing layer (red grid) and corresponding time-lapse seismic surveys (gray grid). The seismic source and receivers are shown in blue.

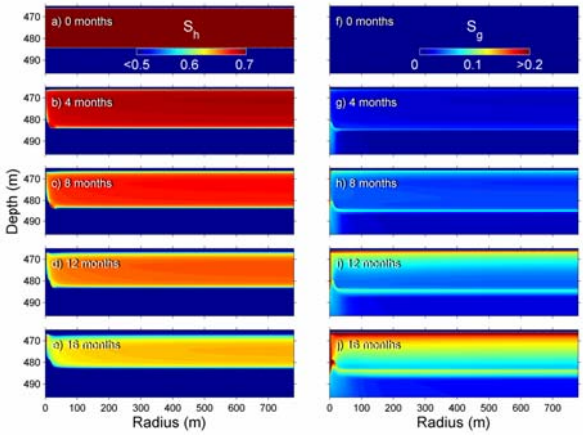

Figure 10. Distributions of simulated gas hydrate saturation (left column) and gas saturation (right column) for increasing times during production (0, 4, 8, 12, and 16 months, respectively). The color scales for S_h and S_g are clipped below 0.5 and above 0.2, respectively, to improve visualization.

incoming plane wave with the desired angle of incidence to the hydrate-bearing layer (the geophysical grid is rotated accordingly to minimize boundary effects). The simulated waveforms are recorded at a string of receivers spanning from above the hydrate-bearing layer to below for each survey.

An example of the simulated seismic response for a receiver located above the HBL at a depth of 355 m is shown in Figure 11. Waveforms are shown at six survey times, up to 20 months after the start of production, for four feasible rock physics models.

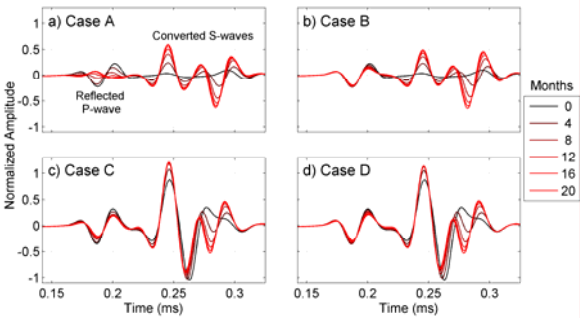

Figure 11. Seismic response during production. Seismic signal recorded above the HBL at a depth of 355 m. Waveforms are shown at six survey times (0, 4 ,8, 12, 16, and 20 months after the start of production) for four rock physics models (a–d).

The initial arrival is the reflected P-wave, as labeled in the figure, followed closely by the converted S-wave arrivals. The converted S-wave evidently provides a good indicator of changes in the HBL during production, but it is important to note that the choice of rock physics model greatly affects the magnitude of change and the shape of the signal in general. In addition, we observed that converted transmitted S-waves recorded below the HBL (not shown) are especially well suited to detect changes occurring in the HBL.

In summary, the application of VSP measurements for monitoring production appears promising, but it is important to accurately determine the rock-physics models and consider uncertainty in the associated parameters.

The numerical simulation tool being developed can provide a means for designing cost-effective geophysical surveys that successfully track the evolution of hydrate properties. This work also serves as a basis for developing a comprehensive method for monitoring production and integrating multiple types of geophysical and hydrological data.

SUMMARY

While the approaches considered in the preceding examples are entirely different from one another, they share the common goal of improving subsurface characterization, by taking advantage of the sensitivity of geophysical data to subsurface fluid distributions and the properties that govern flow and transport. This work reflects the substantial progress made in developing approaches for integrating geophysical and hydrogeochemical data in the TOUGH family of codes in applications ranging from environmental remediation, to nuclear waste storage, to oil and gas production.

ACKNOWLEDGMENT

This work was supported by the U.S. Department of Energy, Contract No. DE-AC02-05CH11231.

REFERENCES

Chen, J., S. Hubbard, Y. Rubin, C. Murray, E. Roden, and E. Majer, 2004. Geochemical characterization using geophysical data and Markov chain Monte Carlo methods: a case study at the South Oyster Bacterial Transport Site in Virginia, *Water Resour. Res.*, *40*(12), W12412.

Finsterle, S., 2004. Multiphase inverse modeling: Review and iTOUGH2 applications, *Vadose Zone J.*, 3: 747–762.

Finsterle, S., C. Doughty, M. B. Kowalsky, G. J. Moridis, L. Pan, T. Xu, Y. Zhang, and K. Pruess, 2008. Advanced vadose zone simulation using TOUGH, *Vadose Zone Journal*, *7*, 601-609.

Finsterle, S., and M. B. Kowalsky, 2008. Joint hydrological-geophysical inversion for soil structure identification, *Vadose Zone Journal*, *7*, 287–293.

Kemna, A., J. Vanderborght, B. Kulessa and H. Vereecken, 2002. Imaging and characterization of subsurface solute transport using electrical resistivity tomography (ERT) and equivalent transport models, *Journal of Hydrology*, *267*(3-4), 125-146.

Kowalsky, M. B., J. Birkholzer, J. Peterson, S. Finsterle, S. Mukhopadhyay, and Y. Tsang, 2008. Sensitivity analysis for joint inversion of GPR and thermal-hydrological data from a large-scale underground heater test, *Nuclear Technology*, *164*(2), 196-206.

Kowalsky, M. B., S. Finsterle, J. Peterson, S. Hubbard, Y. Rubin, E. Majer, A. Ward, and G. Gee, 2005. Estimation of field-scale soil hydraulic and dielectric parameters through joint inversion of GPR and hydrological data, *Water Resour. Res.*, *41*, W11425.

Kowalsky, M. B., S. Finsterle, and Y. Rubin, 2004. Estimating flow parameter distributions using ground-penetrating radar and hydrological measurements during transient flow in the vadose zone, *Adv. in Water Res.*, *27*(6), 583-599.

Kowalsky, M. B., E. Gasperikova, S. Finsterle, D. Watson, S. S. Hubbard, 2009a (submitted). Coupled modeling of hydrogeochemical and electrical resistivity data for exploring the impact of recharge on subsurface contamination, *Geophysics*.

Kowalsky, M. B., S. S. Hubbard, J. Chen, J. E. Peterson, G. P. Flach, 2007. Multiscale hydrogeophysical data integration for parameterization of transport model at Savannah River Site, *EOS Trans. AGU*, *88*(52), Fall Meet. Suppl., Abs. H14C-01.

Kowalsky, M. B., S. Nakagawa, and G. Moridis, 2009b (submitted). Feasibility of Monitoring Gas Hydrate Production with Geophysical Methods, *SPE Journal*.

Kowalsky, M. B., and G. J. Moridis, 2007. Comparison of kinetic and equilibrium reactions in simulating the behavior of gas hydrates. *Energy Conversion and Management*, *48*, 1850–1863.

Lehikoinen, A., S. Finsterle, A. Voutilainen, M. B. Kowalsky, J. P. Kaipio, 2009a. Dynamical inversion of geophysical ERT data: state estimation in the vadose zone, *Inverse Problems in Sci. and Eng.*, 17(6), 715-736..

Lehikoinen, A., J. M. Huttunen, S. Finsterle, M. B. Kowalsky, J. P. Kaipio, 2009b (submitted). Dynamic inversion for hydrological process monitoring under model uncertainties, *Water Resources Res.*

Moridis, G. J., Kowalsky, M. B. Pruess, K. 2005. TOUGH-Fx/HYDRATE v1.0 User's Manual: A code for the Simulation of System Behavior in Hydrate-Bearing Geologic Media, Report LBNL/PUB 3185, Lawrence Berkeley National Laboratory.

Moridis, G. J., M. T. Reagan, 2007. Gas Production From Oceanic Class 2 Hydrate Accumulations. Paper OTC 18866 presented at the 2007 Offshore Technology Conference, Houston, Texas, April 30–May 3, 2007.

Pruess, K., C. Oldenburg, and G. Moridis, 1999. *TOUGH2 User's Guide, Version 2.0*, Report LBNL-43134, Lawrence Berkeley National Laboratory, Berkeley, Calif.

van de Hoven, S. J., D. K. Solomon, and G. R. Moline, 2005. Natural spatial and temporal variations in groundwater chemistry in fractured, sedimentary rocks: scale and implications for solute transport, *Applied Geochemistry*, *20*, 861-873.

SECTION 3

DUAL-DOMAIN CONCEPTS

Publication 4: Flach, G.P., 2012, Relationship between dual-domain parameters and practical characterization data, **Ground Water**, 50(2), 216-229.

Publication 5: Flach, G.P., 2012, Effective porosity implies effective bulk density in sorbing solute transport, **Ground Water**, 50(5), 657-658.

ground water

Relationship Between Dual-Domain Parameters and Practical Characterization Data

by Gregory P. Flach

Abstract

Dual-domain solute transport models produce significantly improved agreement to observations compared to single-domain (advection-dispersion) models when used in an a posteriori data fitting mode. However, the use of dual-domain models in a general predictive manner has been a difficult and persistent challenge, particularly at field-scale where characterization of permeability and flow is inherently limited. Numerical experiments were conducted in this study to better understand how single-rate mass transfer parameters vary with aquifer attributes and contaminant exposure. High-resolution reference simulations considered 30 different scenarios involving variations in permeability distribution, flow field, mass transfer timescale, and contaminant exposure time. Optimal dual-domain transport parameters were empirically determined by matching to breakthrough curves from the high-resolution simulations. Numerical results show that mobile porosity increases with lower permeability contrast/variance, smaller spatial correlation length, lower connectivity of high-permeability zones, and flow transverse to strata. A nonzero non-participating porosity improves empirical fitting, and becomes larger for flow aligned with strata, smaller diffusion coefficient, and larger spatial correlation length. The non-dimensional mass transfer coefficient or Damkohler number tends to be close to 1.0 and decrease with contaminant exposure time, in agreement with prior studies. The best empirical fit is generally achieved with a combination of macrodispersion and first-order mass transfer. Quantitative prediction of ensemble-average dual-domain parameters as a function of measurable aquifer attributes proved only marginally successful.

Introduction

Dual-domain transport formulations have proven effective at representing averaged solute transport behavior in a wide variety of laboratory and field settings. Dual-domain models include the original concept of mobile and immobile regions with first-order, single-rate, mass transfer (Coats and Smith 1964), and subsequent consideration of chemical reactions (Skopp and Warrick 1974), sorption phenomena (van Genuchten and Wierenga 1976), variably saturated conditions (Gaudet et al. 1977), dual-permeability in which advection occurs in both regions (Gerke and van Genuchten 1993), and multiphase transport (Falta 2000). Generalizations to multirate mass transfer (Haggerty and Gorelick 1995; Wang et al. 2005) and fractal transport (Schumer et al. 2003) have been presented. Applications include bimodal permeability fields, such as fractured rock (Bibby 1981; Huyakorn et al. 1983) and aggregated soils (Passioura 1971; Rao et al. 1980), and more recently, granular aquifers exhibiting more continuous permeability distributions. Examples of the latter are the MADE-2 field site (Boggs et al. 1992) on Columbus Air Force Base, Mississippi (Feehley et al. 2000; Harvey and Gorelick 2000; Julian et al. 2001; Zheng and Gorelick 2003; Guan et al. 2008; Llopis-Albert and Capilla 2009), alluvial aquifers near Yucca Mountain, Nevada (Painter et al. 2001) and Tübingen, Germany (Riva et al. 2008), and coastal plain sedimentary aquifers in South Carolina at the U.S. Department of Energy Savannah River Site (Flach et al. 2004) and an Aquifer

Savannah River National Laboratory, Savannah River Site, Bldg. 773-42A, Aiken, SC 29808; (803) 725-5195; fax: (803) 725-7673; gregory.flach@srnl.doe.gov

Received February 2010, accepted May 2011.

doi: 10.1111/j.1745-6584.2011.00834.x

Storage and Recovery (ASR) site near Charleston (Culkin et al. 2008). Other studies focus on laboratory-constructed or synthetic permeability fields involving both binary and continuous permeability variation and varying connectivity of high-permeability zones (Sudicky et al. 1985; Zheng and Gorelick 2003; Zinn and Harvey 2003; Zinn et al. 2004; Gorelick et al. 2005; Liu et al. 2007).

Dual-domain formulations offer a physically based alternative to advection-dispersion models. Plume spreading is handled through the introduction of mobile and immobile porosities and local mass transfer between the two porosities, in addition to a second-order dispersion term. The two approaches exhibit distinctly different behavior. For example, when the hydraulic conductivity (K) field is influenced by the connected preferential flowpaths, the traditional advection-dispersion has been shown to have limited applicability while the mass transfer approach better reproduces plume behavior (Zheng and Gorelick 2003; Liu et al. 2004, 2007). Although present in the dual-domain model, second-order dispersion is secondary to mass transfer for these types of systems.

When used in an a posteriori data fitting mode (Bibby 1981; Harvey and Gorelick 2000; Feehley et al. 2000), dual-domain models produce significantly improved agreement to observations compared to single-domain (advection-dispersion) counterparts, which can be viewed as a subset of the former with fewer degrees of freedom (Griffioen et al. 1998). However, use of dual-domain models in a general predictive manner has been a difficult and persistent challenge (Brusseau et al. 1994; Griffioen et al. 1998; Maraqa 2001; Guswa and Fryberg 2002; Willman et al. 2008), particularly at field-scale where characterization of permeability and flow is inherently limited (Bibby 1981; Painter et al. 2001; Flach et al. 2004). To make predictions in the absence of site-specific tracer data, one would like to relate dual-domain parameter values to aquifer attributes in an optimal manner.

Dual-domain parameters have been related to permeability and flow characteristics for various idealized conditions. For example, the first-order coefficient that preserves the zeroth, first, and second moments between first-order mass transfer and second-order diffusion models has been derived for spherical, cylindrical, and slab inclusions (Parker and Valocchi 1986; Brusseau 1991; Haggerty and Gorelick 1995). Similarly, others have presented analytic expressions for slow advection through lower permeability inclusions with particular idealized geometries (Reichle et al. 1998; Guswa and Freyberg 2002; Cherblanc et al. 2003, 2007). Numerical experiments involving random, high-resolution, permeability fields to provide reference data have provided important insights (Zinn and Harvey 2003; Zheng and Gorelick 2003; Liu et al. 2004; Gorelick et al. 2005; Willman et al. 2008; Fernàndez-Garcia et al. 2009), and a number of researchers have examined experimental datasets at laboratory and field-scale, with the objective of deducing general correlations between dual-domain parameters and characteristics of the permeability and flow fields (Willmann et al. 2008; Zhang et al. 2007; Li et al. 1994; Bajracharya and Barry 1997; Griffioen et al. 1998; Haggerty et al. 2004). Despite these efforts, more work is needed to relate dual-domain model parameters to practical characterization data in field-scale settings, where information is inherently limited and the permeability and flow fields do not align with convenient mathematical constructs (e.g., uniform high-permeability field with embedded inclusions, idealized inclusion shape and size, and diffusion-dominated transport within inclusions).

The objective of our work is to advance understanding of how dual-domain parameters vary with aquifer attributes and contaminant exposure, in order to provide useful guidance to practitioners wishing to apply the modeling technique at particular field sites. We do so by conducting two-dimensional (2D) high-resolution (single-domain) flow and transport simulations for 30 wide-ranging scenarios, followed by one-dimensional (1D) inverse modeling using a dual-domain formulation. We then relate the optimal dual-domain parameter values to characteristics of the permeability distribution, flow field, mass transfer time scales, and contaminant exposure time. We confine our attention to the dual-domain model most commonly used by practitioners, the mobile-immobile, single-rate mass transfer model.

Dual-Domain Transport Formulation

In anticipation of numerical modeling with MT3DMS, we begin with the nomenclature and dual-domain formulation of Zheng and Wang (1999), assuming linear sorption and without first-order decay, internal sources, or groundwater storage. The dual and immobile domain mass balances are

$$\theta_{\mathrm{m}} R_{\mathrm{m}} \frac{\partial C_{\mathrm{m}}}{\partial t} + \theta_{\mathrm{im}} R_{\mathrm{im}} \frac{\partial C_{\mathrm{im}}}{\partial t} = \frac{\partial}{\partial x_i}\left[\theta_{\mathrm{m}} D_{ij} \frac{\partial C_{\mathrm{m}}}{\partial x_j}\right] - \frac{\partial}{\partial x_i}[\theta_{\mathrm{m}} v_{\mathrm{m}} C_{\mathrm{m}}] \tag{1a}$$

$$\theta_{\mathrm{im}} R_{\mathrm{im}} \frac{\partial C_{\mathrm{im}}}{\partial t} = \zeta [C_{\mathrm{m}} - C_{\mathrm{im}}] \tag{1b}$$

where θ_m is void volume in the mobile region divided by total domain volume ("mobile porosity" hereafter), θ_{im} is immobile porosity, R is retardation coefficient, C is solute concentration, v_{m} is pore velocity in the mobile domain, D_{ij} is a diffusion/dispersion coefficient tensor, ζ is a first-order mass transfer coefficient, and the subscripts m and im denote the mobile and immobile domains. Following Zinn and Harvey (2003), we assume that the total porosity is generally composed of mobile and immobile porosities, plus a non-participating porosity which is always devoid of solute:

$$\theta = \theta_{\mathrm{m}} + \theta_{\mathrm{im}} + \theta_{\mathrm{np}} \tag{2}$$

For high-resolution single-domain simulations in two dimensions, the immobile and non-participating porosities are set to zero and the second-order tensor represents molecular diffusion (macrodispersion is accounted for

by the fine-resolution heterogeneous K field). For low-resolution dual-domain simulations in one-dimension with macrodispersion, we assume homogeneous properties, equal retardation in both regions, and redefine the mass transfer coefficient as

$$\alpha = \frac{\zeta}{\theta_{\text{im}}} \tag{3}$$

following a more common convention. We also non-dimensionalize Equations 1 by first defining capacity coefficients

$$\beta_{\text{im}} = \theta_{\text{im}}/\theta_{\text{m}},\ \beta_{\text{np}} = \theta_{\text{np}}/\theta_{\text{m}}, \tag{4a,b}$$

Darcy velocity

$$U = \theta_{\text{m}} v_{\text{m}}, \tag{5}$$

pore velocity based on total porosity

$$v = \theta_{\text{m}} v_{\text{m}}/\theta = U/\theta, \tag{6}$$

and non-dimensional time and space coordinates based on domain length L

$$t' = t/(LR/v) = tU/L\theta R,\ x' = x/L. \tag{7a,b}$$

Using the following timescales for a non-sorbing solute

$t_a = L/v_{\text{m}}$ advection in mobile region (8a)

$t_\theta = L/v$ advection in total region (8b)

$t_D = L^2/D$ dispersion in mobile region (8c)

$t_\alpha = 1/\alpha$ mass transfer between mobile and immobile regions (8d)

Peclet and Damkohler numbers can be defined as

$\text{Pe} = t_D/t_a = v_m L/D$ Peclet number for advection through mobile region (9a)

$\text{Da} = t_a/t_\alpha = \alpha L/v_m$ Damkohler number for advection through mobile region (9b)

$\text{Pe}_\theta = t_D/t_\theta = vL/D$ Peclet number for advection through total region (9c)

$\text{Da}_\theta = \text{t}_\theta/t_\alpha = \alpha L v$ Damkohler number for advection through total region (9d)

$\text{PeDa} = \text{Pe}_\theta \text{Da}_\theta = t_D/t_\alpha$ ratio of diffusion and mass transfer timescales (9e)

With the aforementioned definitions, Equations 1 become

$$\frac{\partial C_{\text{m}}}{\partial \text{t}'} + \beta_{\text{im}} \frac{\partial C_{\text{im}}}{\partial \text{t}'} = \frac{1}{\text{Pe}_\theta} \frac{\partial^2 C_{\text{m}}}{\partial x'^2} - [1 + \beta_{\text{im}} + \beta_{\text{np}}] \frac{\partial C_{\text{m}}}{\partial x'} \tag{10a}$$

$$\frac{\partial C_{\text{im}}}{\partial t'} = \text{Da}_\theta [C_{\text{m}} - C_{\text{im}}] \tag{10b}$$

These mass balance equations, as well as the Peclet and Damkohler numbers, are valid for both sorbing and non-sorbing solutes. Retardation enters only through the definition of non-dimensional time (Equation 7a). For a given domain length, total porosity, and Darcy flow rate (L, θ, U), the independent dimensional parameters (θ_m, θ_{im}, D, ζ) are related to their non-dimensional counterparts (β_{im}, β_{np}, Pe_θ, Da_θ) by

$$\theta_{\text{m}} = \frac{\theta}{1 + \beta_{\text{im}} + \beta_{\text{np}}} \tag{11a}$$

$$\theta_{\text{im}} = \beta_{\text{im}} \frac{\theta}{1 + \beta_{\text{im}} + \beta_{\text{np}}} = \beta_{\text{im}} \theta_{\text{m}} \tag{11b}$$

$$D = \frac{UL}{\theta \text{Pe}_\theta} \tag{11c}$$

$$\zeta = \frac{\text{Da}_\theta U}{L} \frac{\beta_{\text{im}}}{1 + \beta_{\text{im}} + \beta_{\text{np}}} \tag{11d}$$

Equations 11a-d also define MT3DMS code (Zheng and Wang 1999) inputs in terms of the desired non-dimensional parameters. For single-domain, high-resolution, simulation using the total porosity, the governing equations reduce to

$$\frac{\partial C}{\partial t'} = \frac{1}{\text{Pe}_{\theta\text{e}}} \frac{\partial^2 C}{\partial x'^2} - \frac{\partial C}{\partial x'} \tag{12}$$

where the subscript "e" has been added to the Peclet number to denote that the parameter is based solely on an effective molecular diffusion coefficient (D_e) and does not include macrodispersion (D).

Numerical Experiments

We hypothesize that dual-domain parameters depend on permeability distribution, flow field, and mass transfer and contaminant exposure timescales. Binary and bi-modal variations suggest a natural partitioning of the total domain into mobile and immobile porosity regions (Brusseau et al. 1994). For more continuous heterogeneity, the proper partitioning is not obvious, but a case study suggested regions with hydraulic conductivity greater than the effective value might correspond to the mobile domain (Flach et al. 2004). Flow influences the transport timescale for advection compared to dispersion and mass transfer, but orientation with respect to anisotropy is also important. Consider, for example, a system of perfect layers of highly contrasting permeability. Flow parallel to the layering can bypass low-permeability layers, whereas the same flow rate imposed in the perpendicular direction would be forced through all layers, implying very different partitioning. Mass transfer timescales for diffusion and/or slow advection in low-permeability zones are known to affect dual-domain parameters, as well as the duration of an experiment (Haggerty et al. 2004). In this study, we focus on the closely related concept of contaminant exposure time, defined as the amount of time that the domain is exposed to an upgradient source of solute.

Table 1
Test Matrix for Numerical Experiments

Influence	Attribute	Discrete Cases	Continuous Cases
K distribution	Proportion (%) 25, **50**, 75 (low, moderate, high K proportion)	d2, **d1**, d3	N/A
K distribution	Contrast (10^x:1) $x = \mathbf{3}$, 2, 1 (high, moderate, low K contrast)	**d1**, d4, d5	N/A
K distribution	Variance ($\ln K$) 5, **10**, 20 (low, moderate, high K contrast)	N/A	c2, **c1**, c3
K distribution	Connectedness S, **N**, E (Suppressed, Neutral, Enhanced connectedness of high K)	d6, **d1**, d7	c4, **c1**, c5
K distribution	Anisotropy (λ_h/λ_v) **1**, 10 (isotropic, layered)	**d1**, d8-10	**c1**, c6-8
Flow field	Flow orientation w.r.t. anisotropy (deg) **0**, 45, 90 (parallel, cross, perpendicular to layering)	**d1&d8**, d9, d10	**c1&c6**, c7, c8
Mass transfer time (and K distribution)	Correlation length ($\lambda_v/L = 10^x$) $x = -0.5, \mathbf{-1}, -1.5$ (large, moderate, small-scale K features)	d11, **d1**, d12	c9, **c1**, c10
Mass transfer time	Peclet number for diffusion ($\mathrm{Pe}_{\theta e} = vL/\mathrm{D_e} = 10^x$) $x = 2, \mathbf{3}, 4$ (high, moderate, low diffusion relative to advection)	d13, **d1**, d14	c11, **c1**, c12
Solute exposure time	Injection duration/exposure time ($t'_e = 10^x$) 0, **0.5**, 1 (short, moderate, long exposure of medium to solute)	d15, **d1**, d16	c13, **c1**, c14

Numerical experiments were devised to test each of the aforementioned considerations for 30 scenarios involving both discrete (binary) and continuous synthetic permeability fields, as summarized in Table 1. For computational feasibility, high-resolution simulations are defined in two dimensions. A drawback of this approach is that 3D conductivity fields will exhibit more connectivity than 2D fields, all else being equal. However, subsequent interpretations will focus on interpretation and prediction strategies in terms of connectivity itself (which may change with dimensionality) for generality (cf., Knudby and Carrera 2005, section 3.1). Nonetheless, the dimensionality of this analysis may introduce biases in results with respect to field applications. The high-resolution 2D domain is viewed as a heterogeneous volume that will subsequently be treated as a homogeneous medium in dual-domain transport modeling. As such, the domain could encompass an entire plume (Harvey and Gorelick 2000) or represent a single grid block within a numerical model. The domain length (L), Darcy velocity (U), and retardation coefficient (R) are taken as 1 (without loss of generality), and the total porosity (θ) is assumed to be 0.4 (typical of granular aquifers).

High-Resolution Single-Domain Simulations

The heterogeneous fields for the nominal discrete (d1) and continuous (c1) cases were generated using Sequential Indicator Simulation (SIS) and Sequential Gaussian Simulation (SGS) respectively, as implemented in GSLIB (Deutsch and Journel 1998). The discrete realizations were also cleaned using the maximum a-posteriori selection (MAPS) algorithm of Deutsch (1998). An isotropic spherical variogram was selected with a range (λ) set to 10% of the domain length. Heterogeneity at much larger scales than $\lambda/L = 0.1$ cannot be well captured in a domain of length L, and heterogeneity at much smaller scales is more likely to produce equilibrium between high- and low-permeability features and negate the need for a dual-domain model. The additional cases (d2-16, c2-14) are the same as the nominal cases, except as noted in Table 1. Proportion refers to the high conductivity facies, and contrast is the ratio of high to low permeability. For the discrete cases, the higher conductivity was set to 1. For the continuous cases, the distribution was centered around $\ln(K) = 0$. These magnitudes are arbitrary as the Darcy velocity is fixed at $U = 1$. Suppressed (S) and Enhanced (E) connectivity fields for Cases c4-5 were generated using the technique described by Zinn and Harvey (2003), followed by the digital filter

$$K_{ij}^{\text{smoothed}} = \frac{1}{49} \sum_{j'=-3}^{+3} \sum_{i'=-3}^{+3} K_{i+i',j+j'} \qquad (13)$$

which was found to remove some fine-scale granularity (similar to the MAPS algorithm) and somewhat improve connectedness. Suppressed and enhanced connectivity for discrete Cases d6-7 were generated by following the aforementioned steps for a continuous field, and then assigning facies based on a conductivity cutoff to achieve the desired binary proportions. For each case, 30 realizations were generated on a 425 by 425 grid with a cell size of 0.003. Figure 1 shows example realizations for Cases d1, d7, c1, and c5. Table 2 provides the geometric (K_g), arithmetic (K_a), and harmonic (K_h) means for each heterogeneity case, averaged over the 30 realizations.

Flow and transport were simulated over a sub-domain of side dimension $L = 1$. The side length of the permeability fields is 1.425, which allows a centered flow and transport domain to be oriented at any angle (e.g., 45° in Cases d9 and c7). With this approach, the same anisotropic permeability realizations can be used for Cases d8-10, and similarly for Cases c6-8, by rotating the flow and transport modeling domain. Flow was simulated using MODFLOW-2000, version 1.18.00 (Harbaugh et al. 2000). Hydraulic head was prescribed uniformly across the left and right boundaries, and no flow was permitted through the top and bottom boundaries. Inlet head was automatically calibrated to achieve the desired Darcy flow ($U = 1$). The effective conductivity (K_e) for each realization was computed from the prescribed flow rate and head difference across the domain and shown in Table 2. For the continuous heterogeneity cases, the porosity with conductivity exceeding effective conductivity is also indicated.

High-resolution transport simulations were performed with MT3DMS in single-porosity mode and considering only molecular diffusion (no macrodispersion) in the Peclet number (Equation 12, Table 1; numerical dispersion is also present). Initially the domain is devoid of solute. During solute injection, concentrations of 1 and 0 were associated with the inlet and outlet boundary flows from MODFLOW-2000 for the durations noted in Table 1. Total simulation time is set to contaminant exposure (injection) time plus at least 10 times the mean solute residence time (t_θ from Equation 8b; Haggerty et al. 2004), specifically, non-dimensional total durations of 11, 13.16, or 25. A post-injection duration of $10t_\theta$ was judged to be adequate to capture the plume tail for the two shorter injection times. A duration of $15t_\theta$ was chosen to follow the longest injection time to allow additional time for solute to leach from the immobile domain. To minimize numerical dispersion, the third order TVD option was selected and the time step was automatically set such that the maximum cell Courant number was 0.75. For the baseline diffusion coefficient $D_e = 0.0025$ ($\mathrm{Pe}_{\theta e} = 10^3$), the nominal grid Peclet number is 3. The total solute mass discharge rate across the outlet boundary ("breakthrough curve" hereafter) was recorded for each realization. The 30 breakthrough curves for each case were then averaged to produce a composite reference curve for dual-domain optimization. Figure 2 illustrates the resulting ensemble-average breakthrough curves for each of the cases incorporating the nominal solute injection duration (Cases d1-14, c1-12).

Plume Tailing and Transport Formulations

The ensemble breakthrough curves in Figure 2 generally exhibit significant tailing. Exceptions are Case d5 which drops below 0.001 at $t = 2.2$, and Case c10 which intercepts 0.001 near $t = 2.8$. Although the latter cases can likely be adequately modeling using only advection and dispersion, mass transfer is needed in general to reproduce the observed tailing. Pure advection produces a breakthrough curve in the form of a square wave (no tailing), and an advection-dispersion model with high dispersion ($\mathrm{Pe}_\theta \to 0$; completely mixed system) produces more gradual exponential tailing in proportion to the solute residence time. A dual-domain model with single-rate mass transfer and no dispersion exhibits two-stage tailing: a rapid advective flush followed by exponential mass transfer. This behavior is illustrated in Figure 3 for a best fit to the high-resolution reference curve for Case d1. Adding an optimal amount of dispersion significantly improves the fit, as shown by the second fitted dual-domain curve. Here advective and dispersive processes are key to matching early attenuation, and first-order mass transfer controls later attenuation.

Preliminary optimization using unconstrained dual-domain models frequently produced empirical fits with very high dispersion, i.e., $\mathrm{Pe} \ll 10$. As a point of reference, the practitioner's rule of thumb of setting longitudinal dispersivity to 10% of transport distance (Zheng and Bennett 1995) corresponds to $\mathrm{Pe} = 10$, or $\mathrm{Pe}_\theta = 5$ assuming mobile porosity is half of the total. Empirical values for Pe_θ much below 5 are unrealistic in light of field studies (Gelhar et al. 1992), and considered to be an artifact of a bounded model domain and optimization to downstream mass discharge in this study. Nonphysical effects of high dispersion, such as significant upgradient dispersion, are not discounted in the present optimization framework. To compensate for this limitation, the constraint $\mathrm{Pe}_\theta \geq 5$ was imposed in subsequent optimizations. A detailed description of the optimization process is provided in the following section.

Another consideration is whether single-rate mass transfer is an appropriate model for matching the observed breakthrough curves. The late-time reference curves are not strictly linear when plotted in semi-log coordinates, indicating that multirate mass transfer could produce a better empirical fit. However, a multirate model would introduce additional parameters requiring estimation. Single-rate mass transfer is viewed in this study as a reasonable model approximation that introduces minimal additional parameters to be predicted from characterization data, and thus suited for practical field applications.

Optimization of Dual-Domain Parameters

The high-resolution breakthrough curves are viewed as the "truth" to be reproduced to the extent possible through dual-domain modeling at low-resolution, meaning a 1D domain of length L with uniform properties.

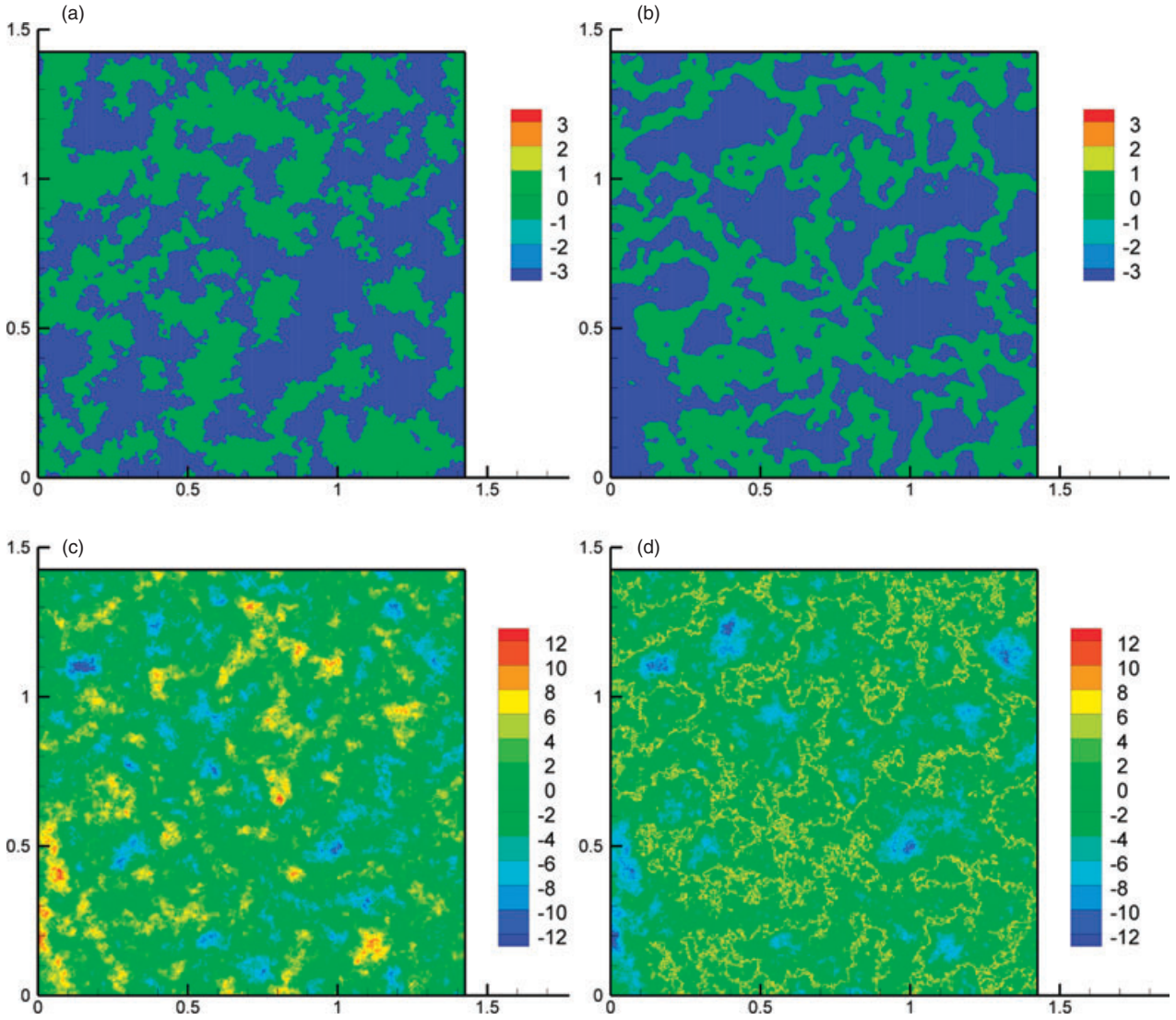

Figure 1. Example heterogeneity realizations: log10(K) for Cases (a) d1 and (b) d7, and ln(K) for Cases (c) c1 and (d) c5.

Dual-domain simulations were performed numerically with MT3DMS and a grid spacing of 0.01, which is sufficiently small to avoid significant numerical dispersion. As with the prior single-domain simulations, the TVD algorithm and a maximum cell Courant number of 0.75 were chosen. Dual-domain parameters were optimized by minimizing a weighted L2 norm for the dual-domain ($\dot{m}_{DDM}$) and high-resolution reference ($\dot{m}_{ref}$) breakthrough curves following Chakraborty et al. (2009):

$$\int \frac{(\dot{m}_{DDM}(t) - \dot{m}_{ref}(t))^2}{\dot{m}_{ref}(t)} dt \qquad (14)$$

Note that this objective function gives preferential weight to the low concentration tail of the solute plume. Optimization was performed using APPSPACK version 5.0.1 (Kolda 2005; Gray and Kolda 2006; Griffin et al. 2008) and HOPSPACK version 2.0 (Plantenga 2009).

The results for optimization using all four dual-domain parameters (β_{im}, β_{np}, $Pe_\theta \geq 5$, Da_θ) are displayed in Table 3, along with their dimensional counterparts. Cases d5 and c10 produced a large Damkohler number, which implies the mobile and immobile regions are nearly in equilibrium and could be well represented by a single-domain model, that is, mobile porosity equal to total porosity. These specific observations point to a general tendency of highly correlated parameters and corresponding non-uniqueness, as others have pointed out. For this reason, and the fact that we are dealing with fits to ensemble-average breakthrough curves rather than individual realizations, we focus more on trends than numerical values. Optimization results for individual realizations are presented later.

The following qualitative behaviors are observed relative to the nominal cases (d1, c1):

1. The mobile porosity increases for (1) lower contrast (d4, d5 recognizing the implications of a large Da_θ) or variance (c2), (2) smaller spatial correlation length (d12, c10 recognizing the implications of a large Da_θ), (3) lower connectivity of high K (d6), and (4) flow

Table 2
Summary Statistics for Random Heterogeneous Fields

Case	K_g	K_a	K_h	K_e	θ_{highK}
(a) Discrete heterogeneity					
d1	3.0E-02	4.9E-01	2.0E-03	4.4E-02	0.2
d2	5.8E-03	2.5E-01	1.3E-03	2.7E-03	0.1
d3	1.6E-01	7.3E-01	3.7E-03	3.4E-01	0.3
d4	9.7E-02	4.9E-01	2.0E-02	1.0E-01	0.2
d5	3.1E-01	5.4E-01	1.8E-01	3.1E-01	0.2
d6	2.7E-02	4.7E-01	1.9E-03	6.9E-03	0.2
d7	3.9E-02	5.3E-01	2.1E-03	1.4E-01	0.2
d8	3.8E-02	5.1E-01	2.1E-03	3.4E-01	0.2
d9	3.8E-02	5.1E-01	2.1E-03	7.5E-02	0.2
d10	3.8E-02	5.1E-01	2.1E-03	3.7E-03	0.2
d11	3.6E-02	4.8E-01	2.0E-03	8.8E-02	0.2
d12	3.1E-02	5.0E-01	2.0E-03	2.9E-02	0.2
d13	3.0E-02	4.9E-01	2.0E-03	4.4E-02	0.2
d14	3.0E-02	4.9E-01	2.0E-03	4.4E-02	0.2
d15	3.0E-02	4.9E-01	2.0E-03	4.4E-02	0.2
d16	3.0E-02	4.9E-01	2.0E-03	4.4E-02	0.2
Case	K_g	K_a	K_h	K_e	$\theta_{K>Ke}$
(b) Continuous heterogeneity					
c1	1.0E+00	1.8E+02	1.0E-02	9.5E-01	0.20
c2	1.0E+00	1.3E+01	8.9E-02	9.7E-01	0.20
c3	1.0E+00	2.3E+04	2.5E-04	9.5E-01	0.20
c4	8.5E-01	9.0E+01	6.7E-03	2.2E-01	0.27
c5	1.3E+00	1.5E+02	2.3E-02	3.8E+00	0.14
c6	1.1E+00	8.1E+01	3.8E-02	4.8E+00	0.13
c7	1.1E+00	8.1E+01	3.7E-02	1.6E+00	0.19
c8	1.1E+00	8.1E+01	3.8E-02	2.6E-01	0.28
c9	1.5E+00	8.1E+01	4.1E-02	1.7E+00	0.20
c10	1.0E+00	1.5E+02	7.7E-03	8.6E-01	0.21
c11	1.0E+00	1.8E+02	1.0E-02	9.5E-01	0.20
c12	1.0E+00	1.8E+02	1.0E-02	9.5E-01	0.20
c13	1.0E+00	1.8E+02	1.0E-02	9.5E-01	0.20
c14	1.0E+00	1.8E+02	1.0E-02	9.5E-01	0.20

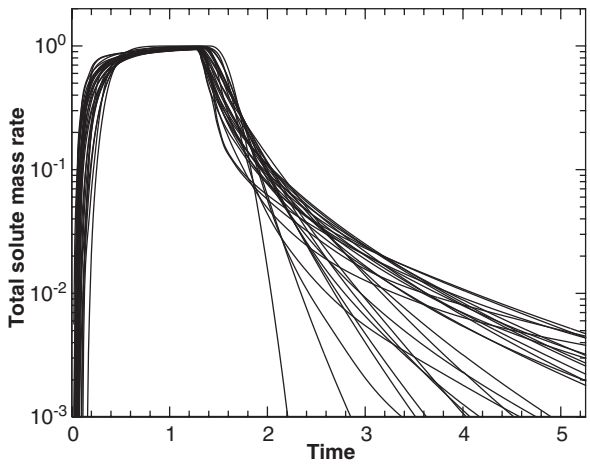

Figure 2. Reference ensemble-average breakthrough curves for nominal injection Cases d1-d14, c1-12.

oriented perpendicular to strata (d10, c8). The latter two observations are apparently a result of flow being less able to bypass low K regions. Case c4 did not produce a high mobile porosity, but the higher Damkohler number indicates enhanced communication between the mobile and immobile porosities, with similar effect.

2. The presence of a nonzero non-participating porosity is generally important toward achieving the best possible empirical fit, as Zinn and Harvey (2003) similarly observed. The non-participating porosity is observed to be larger for discrete Cases d8 (flow more aligned with strata) and d15 (larger scale low K regions). Higher non-participating porosity could be expected for d14 (lower diffusion coefficient), but was not observed. Within the continuous cases, the larger values occur for Cases c7 (flow more aligned with strata), c9 (larger scale low K regions), and c12 (lower diffusion coefficient). Case c3 (higher variance) did not produce a higher non-participating porosity, but the immobile porosity was notably higher than the base case.
3. The Damkohler number tends to be close to, but less than, 1.0. The median and mean values (discounting Cases d5 and c10 for the reason mentioned earlier) are 0.81 and 0.97, respectively. An equivalent statement from Equation 9d is that the mass transfer timescale is equal to or greater than the mean solute residence time

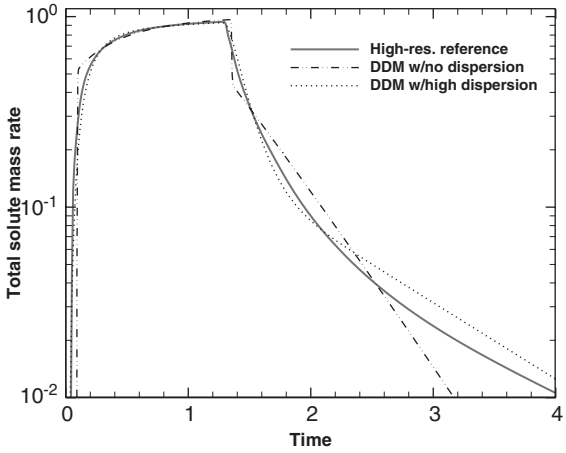

Figure 3. Example dual-domain fit to high-resolution reference breakthrough curve (Case d14 from Table 3).

(t_θ) (Haggert et al. 2004). Cases d15, d16, c13, and c14 indicate a weak dependence on contaminant exposure time t_e, which was chosen to be greater than or equal to t_θ. Taken together, these observations suggest a primary dependence on t_θ and a secondary dependence on t_e. These findings are consistent with Haggerty et al. (2004). We note in particular that $\log10(\mathrm{Da}_\theta)$ plots as a straight line on their Figure 1d, and $\mathrm{Da}_\theta \approx 10^0$ provides a reasonable fit to the data shown. The dependence on t_e implies a decreasing mass transfer coefficient with time. Guan et al. (2008) have recently shown that the mass transfer coefficient decreases with experiment duration.

4. The optimal Peclet number is generally at the prescribed lower bound of 5. The inverse of the Peclet number is the non-dimensional dispersion coefficient (Equation 9c). The median value of $1/\mathrm{Pe}_\theta$ across all cases except Cases d5 and c10 is 0.20. Significant dispersion, combined with mass transfer, produces the best empirical fit to the reference data.

An alternative optimization strategy for evaluating trends is to individually fit each realization within a case, and then compute the ensemble-average of each dual-domain parameter. The results of that exercise for the four-parameter model with the constraint $\mathrm{Pe}_\theta \geq 5$ are provided in Table 4. The geometric average of each set of parameters is indicated. The qualitative trends in parameter values for the discrete cases are similar to Table 3. For several cases, the conditions leading to higher mobile porosity in Table 3 tend to instead produce higher Damkohler number in Table 4. An increase in Damkohler number or mobile porosity has a similar effect on breakthrough. The differences in values also point to inherent non-uniqueness issues with largely unconstrained four-parameter optimization, which are addressed in the following.

Figure 4 illustrates the distributions of dual-domain parameters derived from fitting each realization in Cases d1 and c1. Even though the 30 realizations within each class are statistically identical, transport simulations produced a wide variety of breakthrough curves and optimized model parameters. Also shown in Figure 4 are the geometric mean of the distribution from Table 4 (solid line) and the corresponding value from Table 3 (dashed line). The two values are similar for each parameter, with the exception of β_{np} from Case d1. The latter values correspond to a relatively small fraction of the total porosity, so the difference is not particularly important. Similar variability was observed for other cases from Table 1.

Prediction of Dual-Domain Parameter Trends

Although the dual-domain model with four largely unconstrained inputs is capable of producing excellent empirical fits to data, model parameters must be related to field-measurable attributes of an aquifer system for the formulation to be useful as a predictive tool. Unfortunately, the parameter variability observed within Cases d1 and c1 (Figure 4) and similarly for other classes suggests that accurate prediction of optimal dual-domain parameters for a specific site is not generally feasible based on knowledge of global statistical and deterministic attributes of the system such as those defining each case in Table 1. Evidently the particulars of each realized conductivity field have a strong influence on the optimal dual-domain model approximation, which is perhaps not surprising. With this realization, we consider the more modest goal of qualitatively predicting the variation in ensemble-average behavior between classes, that is, quantitative trends.

With this objective in mind, we first strive to reduce the parameters to a more manageable number, while avoiding excessive sacrifice in model performance. Parameter reduction is motivated in part by inherent issues of non-uniqueness. The parameter estimates for Case d5 ($\mathrm{Da}_\theta \gg 1$) were observed to be practically non-unique, as noted earlier. Although other cases were more determinant, the optimal values typically occur at a shallow minimum of the objective function, implying that other parameter values can be employed to achieve a similar fit. For example, the parameters β_{im} and Da_θ tend to be positively correlated, that is, a higher immobile porosity coupled with a larger mass transfer coefficient has a comparable effect, and vice versa. If β_{im} and Da_θ are defined in a sequential manner, the first parameter assignment can be made with some degree of arbitrariness (within reason), and the second parameter assignment tailored to the precedence set by the first. The work of Haggerty et al. (2004) suggests a strategy of defining the Damkohler number first, followed by capacity coefficients.

The mass transfer rate tends to be correlated to the mean solute residence time and the inverse of the solute exposure time, as noted previously. A crude power-law fit to Da_θ from Cases d1, d15, d16, c1, c13, and c14 in Table 3 motivated by this observation is

$$\mathrm{Da}_\theta = 1.2(\mathrm{t}_\theta/\mathrm{t}_e)^{0.19} \qquad (15)$$

Table 3
Optimization Results for Four-Parameter Dual-Domain Model Fit to Ensemble-Average Breakthrough Curves with the Constraint $Pe_\theta \geq 5$

Case	Objective Function	β_{im}	β_{np}	Pe_θ	Da_θ	θ_m	θ_{im}	θ_{np}	$\theta_{im} + \theta_{np}$	D	ζ
d1	0.021	1.54	0.45	5.0	0.78	0.13	0.21	0.06	0.27	0.50	0.40
d2	0.001	0.03	0.01	7.1	0.64	0.38	0.01	0.01	0.02	0.35	0.02
d3	0.003	0.43	0.08	10.2	0.65	0.27	0.11	0.02	0.13	0.25	0.19
d4	0.005	0.90	0.03	5.0	1.91	0.21	0.19	0.01	0.19	0.50	0.89
d5	0.000	0.59	0.03	33.5	12.03	0.25	0.15	0.01	0.15	0.07	4.40
d6	0.003	0.17	0.01	5.0	1.04	0.34	0.06	0.00	0.06	0.50	0.15
d7	0.004	0.97	0.14	5.0	0.63	0.19	0.18	0.03	0.21	0.50	0.29
d8	0.003	0.84	0.43	6.2	0.45	0.18	0.15	0.08	0.22	0.40	0.17
d9	0.041	1.38	0.02	5.0	0.21	0.17	0.23	0.00	0.23	0.50	0.12
d10	0.001	0.10	0.03	13.6	0.63	0.35	0.04	0.01	0.05	0.18	0.06
d11	0.014	0.58	0.69	5.0	0.67	0.18	0.10	0.12	0.22	0.50	0.17
d12	0.007	1.51	0.01	5.0	1.57	0.16	0.24	0.00	0.24	0.50	0.94
d13	0.017	1.00	0.10	5.0	1.00	0.19	0.19	0.02	0.21	0.50	0.48
d14	0.022	1.43	0.45	5.0	0.58	0.14	0.20	0.06	0.26	0.50	0.29
d15	0.014	1.65	0.65	5.0	1.07	0.12	0.20	0.08	0.28	0.50	0.54
d16	0.027	1.49	0.19	5.0	0.54	0.15	0.22	0.03	0.25	0.50	0.30
c1	0.006	0.75	0.01	5.0	1.15	0.23	0.17	0.00	0.17	0.50	0.49
c2	0.001	0.16	0.01	5.2	1.34	0.34	0.06	0.00	0.06	0.48	0.19
c3	0.018	1.46	0.01	5.0	0.78	0.16	0.24	0.00	0.24	0.50	0.46
c4	0.004	0.70	0.04	5.0	1.98	0.23	0.16	0.01	0.17	0.50	0.80
c5	0.013	1.04	0.02	5.0	0.82	0.19	0.20	0.00	0.21	0.50	0.41
c6	0.018	1.65	0.02	5.0	0.75	0.15	0.25	0.00	0.25	0.50	0.46
c7	0.017	0.95	0.37	5.0	0.70	0.17	0.16	0.06	0.23	0.50	0.29
c8	0.003	0.28	0.04	7.9	0.96	0.30	0.08	0.01	0.10	0.32	0.20
c9	0.011	0.87	0.31	5.0	0.80	0.18	0.16	0.06	0.22	0.50	0.32
c10	0.000	0.40	0.02	5.0	88.58	0.28	0.11	0.01	0.12	0.50	24.75
c11	0.002	0.28	0.01	5.0	2.02	0.31	0.09	0.00	0.09	0.50	0.44
c12	0.009	0.71	0.15	5.0	0.93	0.22	0.15	0.03	0.18	0.50	0.36
c13	0.005	0.84	0.00	5.0	1.33	0.22	0.18	0.00	0.18	0.50	0.61
c14	0.007	0.75	0.02	5.0	1.12	0.23	0.17	0.00	0.17	0.50	0.48

Equation 15 produces Damkohler numbers around 1.0 for the test matrix in Table 1. An equivalent expression to Equation 15 considering Equation 9d is

$$t_\alpha = 0.83 t_\theta^{0.81} t_e^{0.19} \tag{16}$$

which implies a mass transfer timescale primarily dependent on the mean solute residence time t_θ and mildly on the solute exposure time t_e. The former dependence can be interpreted as follows. Any low-permeability regions interacting with high K zones at timescales significantly shorter than t_θ are effectively in equilibrium with the latter, and should be included in the "mobile" domain. Any low-permeability zones that interact with high K zones at timescales significantly longer that t_θ are effectively isolated, and should be assigned to the non-participating porosity. The remaining immobile porosity constitutes low K zones that are capable of interacting with the mobile porosity on the same timescale as advection.

Considering the variability in optimal Da_θ in Table 3 for the same t_θ and t_e in Table 1, the secondary dependence of Da_θ on t_e can be neglected for the range of t_e considered in this study. Thus going forward we simplify Equation 15 to $Da_\theta = 1.0$ and optimize only the three remaining parameters: β_{im}, β_{np}, and $Pe_\theta \geq 5$. As noted earlier, this simplification is consistent with Haggerty et al. (2004). Table 5 provides the optimized results for the reduced model. In place of Da_θ (=1), the sum of the two capacity coefficients is listed. In a few cases, the objective function is slightly smaller in Table 5, which indicates that the four-parameter optimization converged on a local rather than global minimum. This outcome is a manifestation of the inherent shallow minima and non-uniqueness issues discussed earlier. Prescribing Da_θ has the beneficial effect of eliminating non-uniqueness in the advection-dispersion dominated cases such as Case d5. Here advection-dispersion behavior is achieved through a mobile porosity nearly equal to the total porosity, rather than very large Damkohler number which has the identical effect.

We now consider whether the observed variations in optimal β_{im} and β_{np} from the ensemble-average breakthrough curves can be related to practical characterization data. Note that the Peclet number is generally fixed at its prescribed lower bound for heterogeneous cases requiring a mass transfer approach, and thus does not require estimation. Thus only two parameters effectively require prediction. For this study, the available

Table 4
Optimization Results for Four-Parameter Dual-Domain Model with the Constraint $Pe_\theta \geq 5$; Geometric Average of Parameters Derived from Individual Realizations

Case	Objective Function	β_{im}	β_{np}	Pe_θ	Da_θ	θ_m	θ_{im}	θ_{np}	$\theta_{im} + \theta_{np}$	D	ζ
d1	0.014	1.67	0.08	8.3	1.04	0.15	0.24	0.01	0.25	0.30	0.63
d2	0.006	0.68	0.02	12.4	44.46	0.24	0.16	0.00	0.16	0.20	17.86
d3	0.015	0.62	0.05	38.5	1.04	0.24	0.15	0.01	0.16	0.07	0.39
d4	0.007	1.12	0.01	14.3	2.69	0.19	0.21	0.00	0.21	0.18	1.41
d5	0.002	0.70	0.03	119.1	11.53	0.23	0.16	0.01	0.17	0.02	4.66
d6	0.007	0.77	0.02	19.0	4.23	0.22	0.17	0.00	0.18	0.13	1.82
d7	0.011	1.17	0.03	11.2	0.64	0.18	0.21	0.01	0.22	0.22	0.34
d8	0.016	1.08	0.24	108.9	0.44	0.17	0.19	0.04	0.23	0.02	0.21
d9	0.022	1.36	0.28	26.7	0.41	0.15	0.21	0.04	0.25	0.09	0.21
d10	0.009	0.27	0.02	97.9	2.48	0.31	0.08	0.01	0.09	0.03	0.52
d11	0.023	1.09	0.13	38.8	0.43	0.18	0.20	0.02	0.22	0.06	0.21
d12	0.004	1.56	0.01	5.9	1.48	0.16	0.24	0.00	0.24	0.42	0.90
d13	0.008	1.10	0.01	5.7	1.26	0.19	0.21	0.00	0.21	0.44	0.65
d14	0.017	1.46	0.15	10.4	0.54	0.15	0.22	0.02	0.25	0.24	0.30
d15	0.012	1.89	0.05	10.8	0.99	0.14	0.26	0.01	0.26	0.23	0.64
d16	0.017	1.58	0.04	8.0	0.69	0.15	0.24	0.01	0.25	0.31	0.42
c1	0.006	0.87	0.01	5.8	1.21	0.21	0.18	0.00	0.19	0.43	0.56
c2	0.003	0.47	0.01	10.2	3.57	0.27	0.13	0.00	0.13	0.25	1.14
c3	0.012	1.58	0.03	5.0	0.81	0.15	0.24	0.01	0.25	0.50	0.49
c4	0.004	0.85	0.01	8.2	2.99	0.21	0.18	0.00	0.19	0.31	1.36
c5	0.011	1.11	0.05	5.0	0.86	0.19	0.21	0.01	0.21	0.50	0.44
c6	0.013	1.84	0.03	5.1	0.73	0.14	0.26	0.00	0.26	0.49	0.47
c7	0.017	1.11	0.09	6.2	0.78	0.18	0.20	0.02	0.22	0.40	0.39
c8	0.010	0.64	0.03	30.0	3.18	0.24	0.15	0.01	0.16	0.08	1.22
c9	0.012	0.89	0.04	7.0	0.59	0.21	0.18	0.01	0.19	0.36	0.27
c10	0.001	0.43	0.02	5.2	129.72	0.28	0.12	0.00	0.12	0.48	38.66
c11	0.002	0.36	0.01	6.5	3.32	0.29	0.11	0.00	0.11	0.39	0.87
c12	0.010	0.75	0.10	5.6	0.91	0.22	0.16	0.02	0.18	0.44	0.37
c13	0.005	0.97	0.01	6.1	1.35	0.20	0.20	0.00	0.20	0.41	0.66
c14	0.006	0.82	0.01	5.7	1.14	0.22	0.18	0.00	0.18	0.44	0.51

system attributes are taken as L, θ, D_e, U, K_e, K_h, and λ. The length L can be defined as the scale of the plume or other domain of interest. Total porosity θ and effective molecular diffusion coefficient D_e are typically known or can be readily measured in the laboratory. The Darcy velocity U and effective conductivity K_e can be defined from flow model calibration or aquifer testing prior to transport modeling. The harmonic mean K_h (or similar measure of low permeability) can be estimated from small-scale measurements (e.g., core samples) or an approximate statistical distribution for a hydrogeologic unit (e.g., a log-normal distribution). The spatial correlation length λ is more difficult to characterize, but can be estimated using a variety of approaches, such as borehole logging, geophysical testing, and knowledge of the depositional environment in the case of sedimentary aquifers. We purposefully avoid relying on more sophisticated/detailed characterization of aquifer heterogeneity, information that is not likely to be available in practice.

As discussed earlier, the immobile porosity should conceptually be the portion of low K zones that interacts with the mobile porosity at a timescale equal to the mean solute residence time, consistent with the prescribed mass transfer rate $Da_\theta = 1.0$. The mass transfer rate for the entire low K region can be estimated based on timescales for diffusion and slow advection as follows. The Damkohler number defined by Equation 9d is recognized as the non-dimensional mass transfer coefficient in Equation 10b. For diffusional transport, the mass transfer rate is proportional to the timescale for advection through the whole domain divided by the timescale for diffusion within immobile regions

$$Da_{\theta,d} \propto \frac{L/v}{\lambda^2/d} = \left(\frac{L}{\lambda}\right)^2 \frac{d}{vL} \tag{17}$$

where d is the effective molecular diffusion coefficient within the designated immobile region, and vL/d is recognized as a Peclet number. Similarly, for slow advective transport at velocity v_λ in immobile regions,

$$Da_{\theta,a} \propto \frac{L/v}{\lambda/v_\lambda} = \frac{L}{\lambda}\frac{v_\lambda}{v} = \frac{L}{\lambda}\frac{K_\lambda}{K_e} \approx \frac{L}{\lambda}\frac{K_h}{K_e} \tag{18}$$

where the conductivity of the immobile domain K_λ is approximated with the harmonic mean K_h in the final term. Assuming additive effects, the combination of diffusion and slow advective transport has the functional

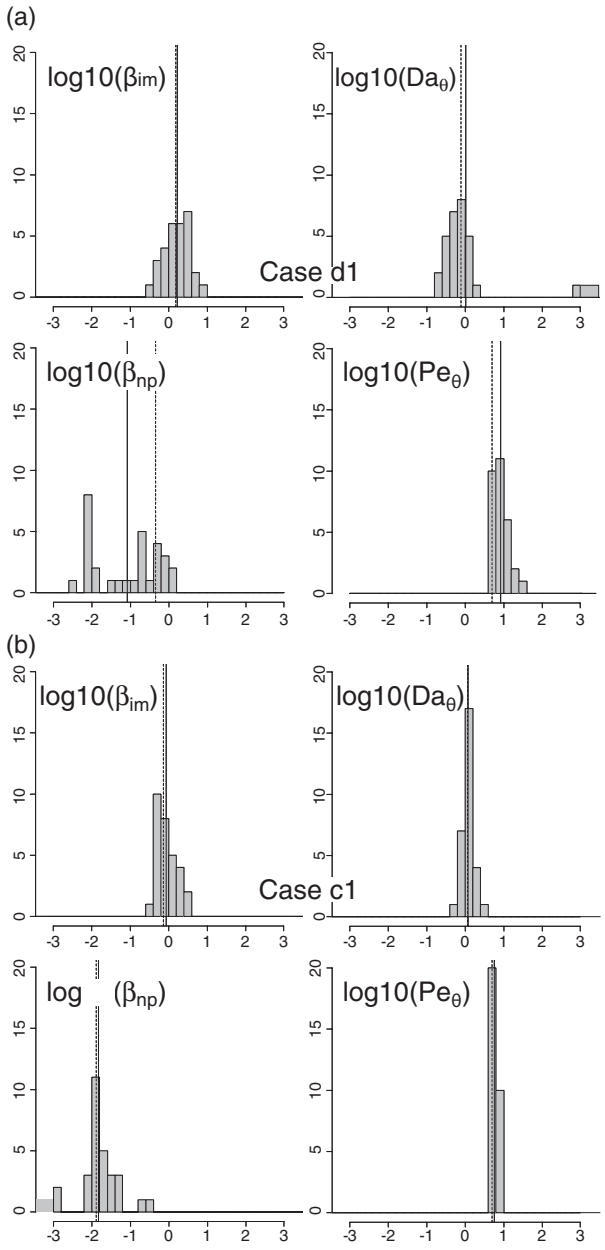

Figure 4. Distribution of optimal dual-domain parameters fit to individual realizations for (a) Case d1 and (b) Case c1; the solid vertical line corresponds to the geometric mean from Table 4, and the dashed line to the value from Table 3.

form

$$\mathrm{Da}_{\theta,\mathrm{da}} = A\left[\left(\frac{L}{\lambda}\right)^2 \frac{d}{vL} + B\cdot\frac{L}{\lambda}\frac{K_\mathrm{h}}{K_\mathrm{e}}\right] \qquad (19)$$

which bears some similarity to the expression presented by Gorelick et al. (2005) for a dendritic network.

One could speculate that (1) large values of $\mathrm{Da}_{\theta,da}$ (>1) would correlate with low K zones being assigned to the mobile domain during optimization, that is, mobile porosity equal to total porosity, (2) small values (<1) would correlate with a large non-participating porosity and nonzero immobile porosity, and (3) intermediate values (~ 1) would correlate with relatively large immobile porosity. To test this hypothesis, we searched for a strong correlation between $\log10(\beta_{\mathrm{np}})$, $\log10(\beta_{\mathrm{im}})$, and $\log10(\Sigma\beta)$ and the function $\log10(\mathrm{Da}_{\theta,da}/A)$ by adjusting coefficient B (because the global multiplier A does not affect correlation coefficients). The strongest correlation between $\log10(\Sigma\beta)$ and $\log10(\mathrm{Da}_{\theta,da}/A)$ occurs when $B = 0.5$. Figure 5 compares the capacity coefficients to the Damkohler function for this setting. The values of correlation coefficient squared (R^2) for $\log10(\mathrm{Da}_{\theta,da}/A)$ vs. $\log10(\beta_{\mathrm{np}})$, $\log10(\beta_{\mathrm{im}})$, and $\log10(\Sigma\beta)$ are 0.26, 0.39, and 0.47, respectively.

Assessment of Parameter Predictions

We were generally unable to accurately relate optimal dual-domain parameters for individual realizations to the global statistical and deterministic attributes of each system configuration summarized in Table 1, given the variability between individual realizations. Quantitative prediction of parameter trends between cases was only marginally successful (e.g., $R^2 = 0.47$ for the sum of capacity coefficients vs. Equation 19). Thus, although good predictions of dual-domain have been achieved for particular systems (Gorelick et al. 2005), accurate forecasts applicable across our wide range of attributes proved elusive in our study. Nonetheless, the concepts and prediction strategy elucidated here may provide useful qualitative guidance to modeling practitioners for considering the influence of physical heterogeneity, flow field characteristics, and mass transfer and contaminant exposure timescales on single-rate mass transfer model parameters.

As a starting point for a modeling exercise, the following general guidance can be suggested for aquifer systems requiring a mass transfer approach, based on the findings of this study:

1. Set hydrodynamic dispersion using traditional methods, for example, longitudinal dispersivity equal to 10% plume length (Pe = 10) for a relatively homogeneous model K field, or lower to the extent that physical heterogeneity is explicitly represented in the model K field.
2. Set the mass transfer coefficient α (or ζ) such that $\mathrm{Da}_\theta = 1$, or possibly lower if the contaminant exposure time is long.
3. Assign capacity coefficients based on an estimated Damkohler number for low K regions taken as a whole (e.g., Equation 19 or comparable expression) relative to the aforementioned specification of Da_θ.

These recommendations should be used with caution given the limitations of this study (e.g., 2D, synthetic K fields, boundary effects) and large prediction uncertainties.

Summary and Conclusions

Numerical experiments were conducted to better understand how dual-domain transport parameters

Table 5
Optimization Results for Three-Parameter Dual-Domain Model

Case	Objective Function	β_{im}	β_{np}	Pe_θ	$\Sigma\beta$	θ_m	θ_{im}	θ_{np}	$\theta_{im} + \theta_{np}$	D	ζ
d1	0.021	1.76	0.64	5.0	2.41	0.12	0.21	0.08	0.28	0.50	0.52
d2	0.001	0.04	0.02	7.4	0.06	0.38	0.01	0.01	0.02	0.34	0.04
d3	0.007	0.45	0.15	13.7	0.61	0.25	0.11	0.04	0.15	0.18	0.28
d4	0.011	0.32	0.01	5.0	0.32	0.30	0.10	0.00	0.10	0.50	0.24
d5	0.000	0.00	0.02	19.1	0.02	0.39	0.00	0.01	0.01	0.13	0.00
d6	0.003	0.16	0.01	5.0	0.17	0.34	0.05	0.00	0.06	0.50	0.14
d7	0.013	1.04	0.34	5.0	1.38	0.17	0.17	0.06	0.23	0.50	0.44
d8	0.022	0.70	0.79	8.3	1.49	0.16	0.11	0.13	0.24	0.30	0.28
d9	0.022	1.00	1.31	5.0	2.31	0.12	0.12	0.16	0.28	0.50	0.30
d10	0.003	0.12	0.05	15.4	0.17	0.34	0.04	0.02	0.06	0.16	0.10
d11	0.015	0.62	0.81	5.0	1.43	0.16	0.10	0.13	0.24	0.50	0.26
d12	0.015	0.75	0.01	5.0	0.76	0.23	0.17	0.00	0.17	0.50	0.43
d13	0.016	1.04	0.17	5.0	1.20	0.18	0.19	0.03	0.22	0.50	0.47
d14	0.025	1.68	1.00	5.0	2.68	0.11	0.18	0.11	0.29	0.50	0.46
d15	0.016	1.65	0.58	5.0	2.24	0.12	0.20	0.07	0.28	0.50	0.51
d16	0.040	2.15	0.49	5.0	2.63	0.11	0.24	0.05	0.29	0.50	0.59
c1	0.007	0.63	0.03	5.0	0.65	0.24	0.15	0.01	0.16	0.50	0.38
c2	0.001	0.11	0.01	5.0	0.12	0.36	0.04	0.00	0.04	0.50	0.10
c3	0.015	1.68	0.30	5.0	1.98	0.13	0.23	0.04	0.27	0.50	0.56
c4	0.009	0.25	0.01	5.0	0.26	0.32	0.08	0.00	0.08	0.50	0.20
c5	0.011	1.15	0.18	5.0	1.33	0.17	0.20	0.03	0.23	0.50	0.50
c6	0.016	1.90	0.39	5.0	2.29	0.12	0.23	0.05	0.28	0.50	0.58
c7	0.020	1.11	0.56	5.0	1.68	0.15	0.17	0.08	0.25	0.50	0.42
c8	0.003	0.29	0.04	8.0	0.33	0.30	0.09	0.01	0.10	0.31	0.22
c9	0.012	0.93	0.39	5.0	1.32	0.17	0.16	0.07	0.23	0.50	0.40
c10	0.000	0.01	0.02	7.1	0.02	0.39	0.00	0.01	0.01	0.35	0.01
c11	0.004	0.10	0.01	5.0	0.11	0.36	0.04	0.00	0.04	0.50	0.09
c12	0.009	0.75	0.17	5.0	0.92	0.21	0.16	0.04	0.19	0.50	0.39
c13	0.008	0.67	0.00	5.0	0.67	0.24	0.16	0.00	0.16	0.50	0.40
c14	0.007	0.67	0.01	5.0	0.68	0.24	0.16	0.00	0.16	0.50	0.40

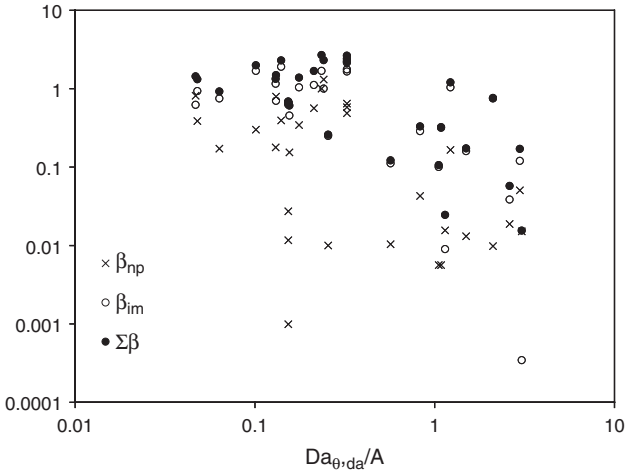

Figure 5. Capacity coefficients compared to $Da_{\theta,da}/A$.

vary with aquifer attributes. High-resolution reference simulations considered 30 different scenarios involving variations in permeability distribution, flow field, mass transfer timescale, and contaminant exposure time. Optimal dual-domain transport parameters were determined by matching breakthrough curves.

Mobile porosity is shown to increase with lower permeability contrast/variance, smaller spatial correlation length, lower connectivity of high-permeability zones, and flow transverse to strata. A nonzero non-participating porosity improves empirical fitting, and becomes larger for flow aligned with strata, smaller diffusion coefficient, and larger spatial correlation length. The non-dimensional mass transfer coefficient or Damkohler number tends to be close to 1.0 and decrease with contaminant exposure time, in agreement with prior studies. The best empirical fit is generally achieved with a combination of macrodispersion and first-order mass transfer.

Prediction of dual-domain parameters for individual realizations was not feasible using statistical average and deterministic attributes of each system configuration, due to significant variations in system behavior between realizations. Quantitative prediction of average parameter variations between classes was only marginally successful. Nonetheless, the concepts and prediction strategy elucidated here may provide useful qualitative guidance to modeling practitioners for considering the influence of physical heterogeneity, flow field characteristics, and mass transfer and contaminant exposure timescales on single-rate mass transfer model parameters.

Acknowledgments

This research was supported by the U.S. Department of Energy (DOE) through the Environmental Remediation Science Program (ERSP) and Savannah River National Laboratory, operated for DOE by Savannah River Nuclear Solutions LLC under contract DE-AC09-08SR22470. The thoughtful peer reviews of Dr. Chunmiao Zheng and two anonymous reviewers, whose constructive comments improved the paper, are much appreciated.

References

Bajracharya, K., and D.A. Barry. 1997. Nonequilibrium solute transport parameters and their physical significance: Numerical and experimental results. *Journal of Contaminant Hydrology* 24, no. 3-4: 185–204.

Bibby, R. 1981. Mass transport of solutes in dual-porosity media. *Water Resources Research* 17, no. 4: 1075–1081.

Boggs, J.M., S.C. Young, L.M. Beard, L.W. Gelhar, K.R. Rehfeldt, and E.E. Adams. 1992. Field study of dispersion in a heterogeneous aquifer 1: Overview and site description. *Water Resources Research* 28, no. 12: 3281–3291.

Brusseau, M.L. 1991. Application of a multiprocess nonequilibrium sorption model to solute transport in a stratified porous medium. *Water Resources Research* 27, no. 4: 589–595.

Brusseau, M.L., Z. Gerstl, D. Augustijn, and P.S.C. Rao. 1994. Simulating solute transport in an aggregated soil with the dual-porosity model: Measured and optimized parameter values. *Journal of Hydrology* 163, no. 1–2: 187–193.

Chakraborty, P., M.M. Meerschaert, and C.Y. Lim. 2009. Parameter estimation for fractional transport: a particle-tracking approach. *Water Resources Research* 45, W10415. DOI: 10.1029/2008WR007577.

Cherblanc, F., A. Ahmadi, and M. Quintard. 2007. Two-domain description of solute transport in heterogeneous porous media: Comparison between theoretical predictions and numerical experiments. *Advances in Water Resources* 30, no. 5: 1127–1143.

Cherblanc, F., A. Ahmadi, and M. Quintard. 2003. Two-medium description of dispersion in heterogeneous porous media: Calculation of macroscopic properties. *Water Resources Research* 39, no. 6: 1154. DOI: 10.1029/2002WR001559.

Coats, K.H., and B.D. Smith. 1964. Dead-end pore volume and dispersion in porous media. *Society of Petroleum Engineers Journal* 4: 73–84.

Deutsch, C.V. 1998. Cleaning categorical variable (lithofacies) realizations with maximum a-posteriori selection. *Computers and Geosciences* 24, no. 6: 551–562.

Deutsch, C.V., and A.G. Journel. 1998. *GSLIB: Geostatistical Software Library and User's Guide*. New York: Oxford University Press, 369 p.

Culkin, S.L., K. Singha, and F.D. Day-Lewis. 2008. Implications of rate-limited mass transfer for aquifer storage and recovery. *Ground Water* 46, no. 4: 591–605.

Falta, R.W. 2000. Numerical modeling of kinetic interphase mass transfer during air sparging using a dual-media approach. *Water Resources Research* 36, no. 12: 3391–3400.

Feehley, C.E., C. Zheng, and F.J. Molz. 2000. A dual-domain mass transfer approach for modeling solute transport in heterogeneous aquifers: Application to the Macrodispersion Experiment (MADE) site. *Water Resources Research* 36, no. 9: 2501–2515.

Fernàndez-Garcia, D., G. Llerar-Meza, and J.J. Gómez-Hernández. 2009. Upscaling transport with mass transfer models: Mean behavior and propagation of uncertainty. *Water Resources Research* 45, W10411. DOI: 10.1029/2009WR007764.

Flach, G.P., S.A. Crisman, and F.J. Molz III. 2004. Comparison of single-domain and dual-domain subsurface transport models. *Ground Water* 42, no. 6: 815–828.

Gaudet, J.P., H. Jégat, G. Vachaud, and P.J. Wierenga. 1977. Solute transfer, with exchange between mobile and stagnant water, through unsaturated sand. *Soil Science Society of America Journal* 41, no. 4: 665–670.

Gelhar, L.W., C. Welty, and K.R. Rehfeldt. 1992. A critical review of data on field-scale dispersion in aquifers. *Water Resources Research* 28, no. 7: 1955–1974.

Gerke, H.H., and M.T. van Genuchten. 1993. A dual-porosity model for simulating the preferential movement of water and solutes in structured porous media. *Water Resources Research* 29, no. 2: 305–319.

Gorelick, S.M., G.S. Liu, and C. Zheng. 2005. Quantifying mass transfer in permeable media containing conductive dendritic networks. *Geophysical Research Letters* 32, no. 18: L18402. DOI: 10.1029/2005GL023512.

Gray, G.A., and T.G. Kolda. 2006. Algorithm 856: APPSPACK 4.0: Asynchronous parallel pattern search for derivative-free optimization. *ACM Transactions on Mathematical Software* 32, no. 3: 485–507.

Griffioen, J.W., D.A. Barry, and J.-Y. Parlange. 1998. Interpretation of two-region model parameters. *Water Resources Research* 34, no. 3: 373–384.

Griffin, J.D., T.G. Kolda, and R.M. Lewis. 2008. Asynchronous parallel generating set search for linearly-constrained optimization. *SIAM Journal on Scientific Computing* 30, no. 4: 1892–1924.

Guan, J., F.J. Molz, Q. Zhou, H.H. Liu, and C. Zheng. 2008. Behavior of the mass transfer coefficient during the MADE-2 experiment: New insights. *Water Resources Research* 44: W02423. DOI: 10.1029/2007WR006120.

Guswa, A.J., and D.L. Freyberg. 2002. On using the equivalent conductivity to characterize solute spreading in environments with low-permeability lenses. *Water Resources Research* 38, no. 8: 1132. DOI: 10.1029/2001WR000528.

Haggerty, R., C.F. Harvey, C.F. von Schwerin, and L.C. Meigs. 2004. What controls the apparent timescale of solute mass transfer in aquifers and soils? A comparison of experimental results. *Water Resources Research* 40: W01510. DOI: 10.1029/2002WR001716.

Haggerty, R., and S.M. Gorelick. 1995. Multiple rate mass transfer for modeling diffusion and surface reactions in media with pore-scale heterogeneity. *Water Resources Research* 31, no. 10: 2383–2400.

Harbaugh, A.W., E.R. Banta, M.C. Hill, and M.G. McDonald. 2000. MODFLOW-2000, the U.S. Geological Survey modular ground-water model: User guide to modularization concepts and the Ground-Water Flow Process. U. S. Geological Survey Open-File Report 00-92, 121 p.

Harvey, C.F., and S.M. Gorelick. 2000. Rate-limited mass transfer or macrodispersion: Which dominates plume evolution at the Macrodispersion Experiment (MADE) site? *Water Resources Research* 36, no. 3: 637–650.

Huyakorn, P.S., B. Lester, and J.W. Mercer. 1983. An efficient finite-element technique for modeling transport in fractured porous media. 1. Single species transport. *Water Resources Research* 19, no. 3: 841–854.

Julian, H.E., M.J. Boggs, C. Zheng, and C.E. Feehley. 2001. Numerical simulation of a natural gradient tracer experiment for the Natural Attenuation Study: Flow and physical transport. *Ground Water* 39, no. 4: 534–545.

Kolda, T.G. 2005. Revisiting asynchronous parallel pattern search for nonlinear optimization. *SIAM Journal on Optimization* 16, no. 2: 563–586.

Knudby, C., and J. Carrera. 2005. On the relationship between indicators of geostatistical, flow and transport connectivity. *Advances in Water Resources* 28, no. 4: 405–421.

Li, L., D.A. Barry, P.J. Culligan-Hensley, and K. Bajracharya. 1994. Mass transfer in soils with local stratification of

hydraulic conductivity. *Water Resources Research* 30, no. 11: 2891–2900.

Liu, G., C. Zheng, and S.M. Gorelick. 2007. Evaluation of the applicability of the dual-domain mass transfer model in porous media containing connected high-conductivity channels. *Water Resources Research* 43: W12407. DOI: 10.1029/2007WR005965.

Liu, G., C. Zheng, and S.M. Gorelick. 2004. Limits of applicability of the advection-dispersion model in aquifers containing connected high-conductivity channels. *Water Resources Research* 40: W08308. DOI: 10.1029/2003WR002735.

Llopis-Albert, C., and J.E. Capilla. 2009. Gradual conditioning of non-Gaussian transmissivity fields to flow and mass transport data. 3. Application to the Macrodispersion Experiment (MADE-2) site, on Columbus Air Force Base in Mississippi (USA). *Journal of Hydrology* 371, no. 1–4: 75–84.

Maraqa, M.A. 2001. Prediction of mass-transfer coefficient for solute transport in porous media. *Journal of Contaminant Hydrology* 50, no. 1–2: 1–19.

Painter, S., V. Cvetkovic, and D.R. Turner. 2001. Effect of heterogeneity on radionuclide retardation in the alluvial aquifer near Yucca Mountain, Nevada. *Ground Water* 39: 326–338.

Parker, J.C., and A.J. Valocchi. 1986. Constraints on the validity of equilibrium and first-order kinetic transport models in structured soils. *Water Resources Research* 22, no. 3: 399–407.

Passioura, J.B. 1971. Hydrodynamic dispersion in aggregated media; 1. Theory. *Soil Science* 111, no. 6: 339–344.

Plantenga, T.D. 2009. HOPSPACK 2.0 User Manual (v 2.0.1). Sandia Report SAND2009-6265, 64 p.

Rao, P.S.C., D.E. Rolston, R.E. Jessup, and J.M. Davidson. 1980. Solute transport in aggregated porous media: Theoretical and experimental evaluation. *Soil Science Society of America Journal* 44, no. 6: 1139–1146.

Reichle, R.H., W. Kinzelbach, and H. Kinzelbach. 1998. Effective parameters in heterogeneous and homogeneous transport models with kinetic sorption. *Water Resources Research* 34, no. 4: 583–594. DOI: 10.1029/97WR03518.

Riva, M., A. Guadagnini, D. Fernandez-Garcia, X. Sanchez-Vila, and T. Ptak. 2008. Relative importance of geostatistical and transport models in describing heavily tailed breakthrough curves at the Lauswiesen site. *Journal of Contaminant Hydrology* 101, no. 1–4: 1–13.

Schumer, R., D.A. Benson, M.M. Meerschaert, and B. Baeumer. 2003. Fractal mobile/immobile solute transport. *Water Resources Research* 39, no. 10: 1296. DOI: 10.1029/2003WR002141.

Skopp, J., and A.W. Warrick. 1974. A two-phase model for the miscible displacement of reactive solutes in soils. *Soil Science Society of America Journal* 38, no. 4: 545–550.

Sudicky, E.A., R.W. Gillham, and E.O. Frind. 1985. Experimental investigation of solute transport in stratified porous media. 1. The nonreactive case. *Water Resources Research* 21, no. 7: 1035–1041.

van Genuchten, M.Th., and P.J. Wierenga. 1976. Mass transfer studies in sorbing porous media I. Analytical solutions. *Soil Science Society of America Journal* 40, no. 4: 473–480.

Wang, P.P., C. Zheng, and S.M. Gorelick. 2005. A general approach to advective–dispersive transport with multirate mass transfer. *Advances in Water Resources* 28, no. 1: 33–42.

Willmann, M., J. Carrera, and X. Sánchez-Vila. 2008. Transport upscaling in heterogeneous aquifers: What physical parameters control memory functions? *Water Resources Research* 44: W12437. DOI: 10.1029/2007WR006531.

Zhang, Y., D.A. Benson, and B. Baeumer. 2007. Predicting the tails of breakthrough curves in regional-scale alluvial systems. *Ground Water* 45, no. 4: 473–484.

Zheng, C., and S.M. Gorelick. 2003. Analysis of solute transport in flow fields influenced by preferential flowpaths at the decimeter scale. *Ground Water* 41, no. 2: 142–155.

Zheng, C., and P.P. Wang. 1999. MT3DMS, A modular three-dimensional multi-species transport model for simulation of advection, dispersion and chemical reactions of contaminants in groundwater systems; Documentation and user's guide. U.S. Army Engineer Research and Development Center Contract Report SERDP-99-1, Vicksburg, Mississippi, 202 p.

Zheng, C., and G.D. Bennett. 1995. *Applied Contaminant Transport Modeling: Theory and Practice.* New York: van Nostrand Reinhold, 440 p.

Zinn, B., L.C. Meigs, C.F. Harvey, R. Haggerty, W.J. Peplinski, and C.F. von Schwerin. 2004. Experimental visualization of solute transport and mass transfer processes in two-dimensional conductivity fields with connected regions of high conductivity. *Environmental Science and Technology* 38, no. 14: 3916–3926.

Zinn, B., and C.F. Harvey. 2003. When good statistical models of aquifer heterogeneity go bad: A comparison of flow, dispersion, and mass transfer in connected and multivariate Gaussian hydraulic conductivity fields. *Water Resources Research* 39, no. 3: 1051. DOI: 10.1029/2001WR001146.

ground water

Technical Commentary/

Effective Porosity Implies Effective Bulk Density in Sorbing Solute Transport

by G.P. Flach

The concept of an *effective porosity* is widely used in solute transport modeling to account for the presence of a fraction of the medium that effectively does not influence solute migration, apart from taking up space. This non-participating volume or ineffective porosity plays the same role as the gas phase in single-phase liquid unsaturated transport: it increases pore velocity, which is useful toward reproducing observed solute travel times. The prevalent use of the effective porosity concept is reflected by its prominent inclusion in popular texts, for example, de Marsily (1986), Fetter (1988, 1993), and Zheng and Bennett (2002).

The purpose of this commentary is to point out that proper application of the concept for sorbing solutes requires more than simply reducing porosity while leaving other material properties unchanged. More specifically, effective porosity implies the corresponding need for an *effective bulk density* in a conventional single-porosity model. The reason is that the designated non-participating volume is composed of both solid and fluid phases, both of which must be neglected for consistency. Said another way, if solute does not enter the ineffective porosity then it also cannot contact the adjoining solid. Conceptually neglecting the fluid portion of the non-participating volume leads to a lower (effective) porosity. Similarly, discarding the solid portion of the non-participating volume inherently leads to a lower or effective bulk density. In the author's experience, practitioners virtually never adjust bulk density when adopting the effective porosity approach.

Savannah River National Laboratory, 773-42A Savannah River Site, Aiken, SC 29808; gregory.flach@srnl.doe.gov

Received October 2011, accepted February 2012.

Savannah River Nuclear Solutions, LLC (SRNS), is Managing and Operating Contractor of the United States Department of Energy for the Savannah River Site under Contract No. DE-AC09-08SR22470.

doi: 10.1111/j.1745-6584.2012.00934.x

Effective bulk density is easily derived in terms of assumed effective porosity. The following exercise assumes that the participating and non-participating volumes have the same pore scale porosity and solid density, but that is not required. Let V = total volume, V_f = fluid volume, $\varphi = V_f/V$ = porosity, M_s = solid mass, $\rho_s = M_s/(V - V_f)$ = solid density, $\rho_b = M_s/V = (1-\varphi)\rho_s$ = bulk density, V_p = participating (mobile) volume, and $f_p = V_p/V$ = participating fraction. Then the effective (participating, mobile) porosity is defined by

$$\theta_{eff} = \frac{V_{fp}}{V} = \frac{V_{fp}}{V_f}\frac{V_f}{V} = f_p\varphi \tag{1}$$

where V_{fp} is the fluid volume within the participating volume. Similarly the effective bulk density is defined by

$$\rho_{b,eff} = \frac{M_{sp}}{V} = \frac{M_{sp}}{M_s}\frac{M_s}{V} = f_p\rho_b = f_p(1-\varphi)\rho_s \tag{2}$$

where M_{sp} is the solid mass within the participating volume. Combining Equations (1 and 2) produces

$$\rho_{b,eff} = \frac{\theta_{eff}}{\varphi}\rho_b = \frac{\theta_{eff}}{\varphi}(1-\varphi)\rho_s. \tag{3}$$

One can also define an *effective solid density*, which is useful for modeling software that takes (or requires) solid density as input. Using Equations (2 and 3) the result is

$$\rho_{s,eff} = \frac{\rho_{b,eff}}{(1-\theta_{eff})} = \frac{\theta_{eff}}{(1-\theta_{eff})}\frac{(1-\varphi)}{\varphi}\rho_s. \tag{4}$$

We next examine the impact of alternative density assignments on solute retardation. To generate example values, we consider the following specific settings representative of a sedimentary aquifer at the Savannah River Site: $\varphi = 0.40$, $\theta_{eff} = 0.25$ (Flach et al. 2004), and $\rho_b = 1.6$ g/cm^3. The sorption coefficient (K_d) is arbitrarily assumed to be 1.0 cm^3/g.

As one intuitively anticipates, Equation (3) preserves retardation between the total (R) and effective porosity (R_{eff}) systems

$$R = 1 + \frac{\rho_b K_d}{\varphi} = 1 + \frac{\rho_{b,\text{eff}} K_d}{\theta_{\text{eff}}} = R_{\text{eff}} = 5. \quad (5)$$

In contrast, if the unaltered original bulk density is used with an effective porosity in forward model predictions, then retardation is biased high

$$1 + \frac{\rho_b K_d}{\theta_{\text{eff}}} = 7.4 > 1 + \frac{\rho_b K_d}{\varphi} = 5 \quad (6)$$

The bias is larger still if the unaltered solid density is coupled with an effective porosity

$$1 + \frac{(1-\theta_{\text{eff}})\rho_s K_d}{\theta_{\text{eff}}} = 9 > 1 + \frac{(1-\varphi)\rho_s K_d}{\theta_{\text{eff}}} = 1 + \frac{\rho_b K_d}{\theta_{\text{eff}}} = 7.4 > 1 + \frac{\rho_b K_d}{\varphi} = 5. \quad (7)$$

If experimental retardation data are fit using a single-porosity model with variable effective porosity, but bulk density is fixed at the total porosity value, then the apparent sorption coefficient will be biased low because the analysis assumes excess solid is present

$$\frac{\theta_{\text{eff}}(R-1)}{\rho_b} = 0.625 < \frac{\theta_{\text{eff}}(R-1)}{\rho_{b,\text{eff}}} = K_d = 1. \quad (8)$$

Thus the direction of the bias differs for inverse modeling vs. forward simulations. Biases are zero when effective porosity is equal to total porosity, and increase with increasing non-zero ineffective porosity. These modeling biases can be eliminated by adopting an effective bulk density using Equation (3).

References

de Marsily, G. 1986. *Quantitative Hydrogeology: Groundwater Hydrology for Engineers.* Orlando, Florida: Academic Press, 440 p.

Fetter, C.W. 1988. *Applied Hydrogeology*, 2nd ed. New York: Macmillan Publishing Company, 592 p.

Fetter, C.W. 1993. *Contaminant Hydrogeology.* New York: Macmillan Publishing Company, 458 p.

Flach, G.P., S.A. Crisman, and F.J. Molz III. 2004. Comparison of single-domain and dual-domain subsurface transport models. *Ground Water* 42, no. 6: 815–828.

Zheng, C., and G.D. Bennett. 2002. *Applied Contaminant Transport Modeling*, 2nd ed. New York: Wiley, 621 p.